

Multiple-scale Dynamics in Neural Systems: Learning, Synchronization and Network Oscillations

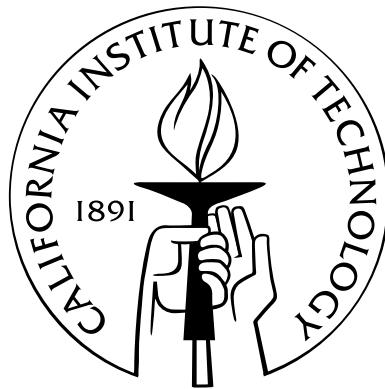
Thesis by

Valentin P. Zhigulin

In Partial Fulfillment of the Requirements

for the Degree of

Doctor of Philosophy



California Institute of Technology

Pasadena, California

2004

(Defended May 12, 2004)

© 2004

Valentin P. Zhigulin

All Rights Reserved

Acknowledgements

This work would not have been possible without the help and support of many people. I would like to thank Mikhail Rabinovich for constant encouragement and support. His scientific advice and, even more importantly, worldly wisdom were and will always be invaluable to me. I am thankful to Gilles Laurent for inspiring much of the research presented in this thesis and for giving me the freedom to pursue it. Many thanks go to Michael Cross for his advice and for raising questions that have led to the improvement of this thesis. I would also like to thank Pietro Perona for giving the impetus to my studies of chaotic dynamics in neural networks. I thank all members of Gilles Laurent's lab and especially Vivek Jayaraman, Roni Jortner, Rachel Wilson and Ofer Mazor for keeping me grounded and aware of the latest experimental data and of the pitfalls of my models, and a former lab member Alex Bäcker for letting the wildest ideas fly.

I have had a wonderful experience while working at the Institute for Nonlinear Science. I would like to thank all its members and especially Henry Abarbanel for making it possible, Ramon Huerta for teaching me so much, Dmitry Volfson for countless discussions and Rafi Levi for keeping my political views in check. Special thanks go to Thomas Nowotny who has performed experiments that are described in Chapter 3, endured my interferences into them and had been a great collaborator on that project.

Last but not least, I would like to thank my wife, Natalia, for her love and support and for making me happy.

Abstract

Many dynamical processes that take place in neural systems involve interactions between multiple temporal and/or spatial scales which lead to the emergence of new dynamical phenomena. Two of them are studied in this thesis: learning-induced robustness and enhancement of synchronization in small neural circuits; and emergence of global spatio-temporal dynamics from local interactions in neural networks.

Chapter 2 presents the study of synchronization of two model neurons coupled through a synapse with spike-timing-dependent plasticity (STDP). It shows that this form of learning leads to the enlargement of frequency locking zones and makes synchronization much more robust to noise than classical synchronization mediated by non-plastic synapses. A simple discrete-time map model is presented that enables deep understanding of this phenomenon and demonstrates its generality. Chapter 3 extends these results by demonstrating enhancement of synchronization in a hybrid circuit with living postsynaptic neuron. The robustness of STDP-mediated synchronization is further confirmed with simulations of stochastic plasticity.

Chapter 4 studies the entrainment of a heterogeneous network of electrically coupled neurons by periodic stimulation. It demonstrates that, when compared to the case of non-plastic input synapses, inputs with STDP enhance coherence of network oscillations and improve robustness of synchronization to the variability of network properties. The observed mechanism may play a role in synchronization of hippocampal neural ensembles.

Chapter 5 proposes a new type of artificial synaptic connection that combines fast reaction of an electrical synapse with plasticity of a chemical synapse. It shows that such synapse mediates regularization of chaos in a circuit of two chaotic bursting neu-

rons and leads to structural stability of the regularized state. Such plastic electrical synapse may be used in the development of robust neural prosthetics.

Chapter 6 suggests a new approach to the study of spatio-temporal network dynamics. The approach is based on the analysis of dynamical motifs – small subnetworks with periodic and chaotic dynamics. It is used to explain the transition from quiescence to periodic and chaotic dynamics in simulations of randomly connected neural networks and the domination of periodic dynamics in simulations of spatially distributed networks with local connectivity.

Contents

Acknowledgements	iii
Abstract	iv
1 Introduction	1
1.1 The brain as a complex, multiscale system	1
1.2 Thesis overview	3
1.3 Summary of work	5
2 Robustness and enhancement of neural synchronization by activity-dependent coupling	7
2.1 Introduction	7
2.2 Description of the model	8
2.3 Results	11
2.3.1 Enhancement of synchronization	11
2.3.2 Robustness of synchronization	14
2.3.3 Phase diffusion	15
2.3.4 Synchronization of bursts	17
2.3.5 Discrete time map model	18
2.4 Discussion	25
3 Plasticity-mediated enhancement of synchronization in a hybrid neural circuit	26
3.1 Introduction	26

3.2	Materials and methods	28
3.2.1	Preparation	28
3.2.2	Experimental setup	28
3.2.3	Spike generator and synapse model	29
3.2.4	Learning rule	31
3.2.5	Experimental protocol	35
3.2.6	Data analysis	36
3.2.7	Computational model	38
3.3	Results	41
3.3.1	Frequency synchronization in the hybrid circuit	41
3.3.2	Numerical results	44
3.3.3	Robustness	46
3.3.4	The mechanism	47
3.4	Discussion	49
4	Entrainment of electrically coupled neural ensembles by STDP-mediated periodic inputs	54
4.1	Introduction	54
4.2	Description of the model	55
4.3	Results	56
4.4	Discussion	59
5	Regularization of chaos in neural circuits with plastic electrical synapses	61
5.1	Introduction	61
5.2	Description of the model	63
5.3	Results	65
5.4	Discussion	70
6	Dynamical motifs: Building blocks of complex dynamics in neural networks	72

6.1	Introduction	72
6.2	Description of the model	73
6.3	Results	74
6.3.1	Dynamics in Erdős-Rényi networks	74
6.3.2	Dynamical motifs	82
6.3.3	Dynamics in spatial networks	89
6.4	Discussion	92
	Bibliography	94

List of Figures

2.1	Dependence of spiking frequency F on the input current I_{stim} for the model neuron (dots). Solid line represents its fit given by equation (2.5).	9
2.2	Plots of the update rule (2.8) in the cases of (top) STDP and (bottom) inverse STDP. Only pairs of the nearest pre- and postsynaptic spikes are taken for calculation of Δg .	11
2.3	Synchronization of the neurons with inverse STDP coupling. (top) Membrane voltages of presynaptic (dotted line) and postsynaptic (solid line) neurons. Postsynaptic neuron was initially spiking faster than the presynaptic one due to relatively strong coupling between them. Coupling strength decreased (bottom) and synchronized state was reached.	12
2.4	Same as in Fig. 2.3, but with postsynaptic neuron initially spiking slower than the presynaptic one (top) due to relatively weak coupling between them. Coupling strength increased (bottom) and synchronized state was reached.	13
2.5	Devil's Staircase for (a) constant synaptic strength and (b) synaptic strength varying according to inverse STDP coupling. T_1 and T_2 are the observed periods of the presynaptic (driving) neuron and postsynaptic (driven) neuron respectively. In (c) the final value of synaptic strength is displayed.	15
2.6	Two-dimensional projections of the phase portraits of the system for different values of T_1 : (a) 24.2 ms, (b) 24.33 ms, (c) 27 ms, and (d) 29 ms. The autonomous oscillation period of the postsynaptic neuron was 15 ms.	16

2.7	Same as Fig. 2.5, but with zero mean, Gaussian, white noise with $\sigma = 0.1$ nA added to the membrane currents.	17
2.8	The difference of oscillation phases of two neurons as a function of time in the cases of (a) constant and (b) activity-dependent coupling.	18
2.9	Average rate of phase slips as a function of RMS noise amplitude for the case of 1:1 synchronization and constant (solid line) or activity-dependent (dashed line) coupling.	19
2.10	Out-of-phase rapid locking of the postsynaptic neuron membrane voltage (solid line) to a burst of spikes from the presynaptic neuron (dotted line). The frequency of the second neuron changes significantly and the transient period before complete synchronization is short.	19
2.11	Phase response curve of the model neuron that was rescaled by synaptic conductance, $g = 3.6 \cdot 10^{-9} S$ in this case (dots). Solid line represents its approximation by Eq. (2.11).	20
2.12	Arnol'd Tongues calculated for the discrete map model with (a) constant and (b) activity-dependent coupling. $T_2^0 = 13$ ms.	21

- 3.1 Experimental setup for the hybrid circuit of a simulated presynaptic neuron, a simulated synapse and a postsynaptic biological neuron from the *Aplysia* abdominal ganglion. The presynaptic neuron is a spike generator eliciting spikes of predetermined form at predetermined times which are read from a file. The synapse is simulated by the same software. The calculated synaptic current is injected into the postsynaptic neuron by means of a D/A converter (Digidata 1200, Axon, CA) and intracellular amplifier (A-M systems). The postsynaptic membrane potential is made available to the combined spike generator/ dynamic clamp software in the reverse direction. All relevant variables, the pre- and postsynaptic potentials and the injected synaptic current, are recorded by a separate data acquisition computer using DasyLab 5.6 (DATALOG - A National Instruments Company). Note that the calculated synaptic current as well as the plastic synapse conductance depend on both the pre- and postsynaptic voltages. Through the dependencies on the postsynaptic membrane potential, an effective feedback loop is formed between the synapse and the postsynaptic neuron. This feedback allows the STDP synapse to adjust to the intrinsic properties of the postsynaptic neuron 30
- 3.2 Episode of the uncoupled (left) and coupled (right) dynamics of the simulated and the biological neuron. The coupled dynamics are shown for a situation of stable 1:1 synchronization. The upper two panels show the membrane potentials of the simulated presynaptic and the biological postsynaptic cells, respectively. The lowest panel shows the synaptic current injected into the postsynaptic neuron. Note the pre- and postsynaptic spike forms and the typical EPSCs in the synaptic current. The synaptic strength in this example is comparably weak and clearly stabilized below the allowed maximum g_{\max} 32

- 3.5 Two examples of synchronization windows. A, D show the ratios of coupled periods against the ratios of uncoupled periods for the static coupling and B, E display these data for the plastic synapse. Note the much larger synchronization windows and the very small error bars in the synchronized states in the experiments with the STDP synapse. The two experiments shown here correspond to numbers 4 and 5 in Figure 7. C, F show the average synaptic strength of the STDP synapse during the last 30 s of coupling (triangles) and the constant synaptic strength of the static synapse (circles). 37
- 3.6 Example of a synchronization experiment in the computational model. The upper panel shows the membrane potential of the presynaptic HH neuron (black line) and of the postsynaptic HH neuron (gray line). The lower panel shows the synaptic conductance. The synchronized state is entered around 4000 *ms*. Note how the synaptic conductance stabilizes at a low value in the synchronized state and that there is a non-zero phase lag of about 90° in this example. 41
- 3.7 Three characteristics of the synchronization windows observed in 5 experiments. The left panel shows the width of the synchronization windows, W , the middle panel the averaged average ratio $\langle\langle T_1/T_2 \rangle_T \rangle_W$ within the synchronization window and the right panel the averaged standard deviation of the period ratios $\langle\sigma(T_1/T_2) \rangle_T \rangle_W$. The squares are the data obtained with a STDP synapse and the circles correspond to a static synapse. Note that synchronization windows are always larger and synchronization is always more precise and more robust for the STDP synapse than for the static synapse. 43

- 3.8 Numerical results. Synchronization window for 1:1 frequency synchronization of the simulated neurons for the cases of a static synapse (A, D) and (B, G) and of a STDP synapse (C, H) and (D, I). Linear superposition of synaptic changes was used in (C, H) and the non-linear suppression model in (D, I). Note that the results do not differ significantly. In (E, J) the average steady-state value of the synaptic strength g for the STDP synapses and the constant synaptic strength of the static synapses are displayed. The maximal synaptic strength of the STDP synapses was $25 nS$ in this study. The plots in the right column correspond to simulations with noise. Note the clear enlargement of the synchronization windows for both of the learning schemes and both in presence and absence of noise. The error bars in (A - D) and (F-I) indicate the standard deviation of the ratio $\langle (T_1/T_2)_{\text{coupled}} \rangle$. They show the precision of the frequency synchronization. There is a clear dependence of the equilibrium synaptic strength of the STDP synapse in the synchronization regime on the initial frequency mismatch. 45
- 3.9 Mechanism of stable synchronization. Panel A shows the stable fixed point for the synaptic conductance for a period $T_1 = T_2 = \Delta t_1 + \Delta t_2$. The two contributions Δg_1 and Δg_2 cancel each other and the net change of synaptic strength is 0. If the postsynaptic neuron is too slow as shown in panel B, the synaptic changes do not cancel such that there is a net increase in synaptic strength and the postsynaptic neuron is driven stronger forcing it back into the synchronized state. On the other hand, if the postsynaptic neuron is too fast as depicted in panel C, the net change in synaptic strength is negative and the postsynaptic neuron is driven less strong bringing it back into synchronization as well. 48

3.10	Time lags in the synchronized state. Panel A shows the spike time difference between each presynaptic and the next postsynaptic spike in the synchronized state. The solid line corresponds to the time difference predicted by the fixed point analysis of the learning rule. There is a perfect correspondence in the 1:1 synchronization region. The on average stronger forcing through the static synapse causes on average shorter time delays (right panel). The dependence of the average time delays on the presynaptic period T_1 in the case of the static synapse comes about because the mismatch of frequencies is higher on the left side than on the right side of the synchronization step. Therefore, stronger forcing would be needed to obtain the same small delays on the left side as on the right side which can not be provided by the synapse of constant strength.	49
4.1	(A) Configuration of the model: heterogeneous network of tonically spiking pyramidal neurons stimulated by external periodic input through a set of STDP synapses. (B) The curve illustrating the learning rule used in simulations of STDP.	55
4.2	Time series of the local field potential in networks with constant (top) and STDP-mediated (bottom) inputs.	56
4.3	Dynamics of conductances of input synapses with STDP.	57
4.4	Dependence of the amplitude of network's local field potential on the number of input synapses.	58
4.5	Dependence of the amplitude of network's local field potential on the average conductance of gap junctions.	59
4.6	Dependence of the amplitude of network's local field potential on the variability of network parameters.	59

5.1	Largest Lyapunov exponent λ calculated for the stimulated Hindmarsh-Rose neuron as a function of stimulating current I . Dynamics of this model neuron is periodic for $I \lesssim 2.75$ (see insert (a) and Fig. 5.2(a)) and $I \gtrsim 3.25$ (see insert (c) and Fig. 5.2(c)), and is chaotic for $2.75 \lesssim I \lesssim 3.25$ (see insert(b) and Fig. 5.2(b)).	62
5.2	Time series of the membrane potential $x(t)$ during (a) periodic bursting, (b) chaotic spiking-bursting and (c) periodic spiking dynamics of the uncoupled ($g = 0$) Hindmarsh-Rose neuron (5.1) stimulated by a DC current with the following strength: (a) $I = 2.6$, (b) $I = 3.1$ and (c) $I = 3.4$	63
5.3	Largest Lyapunov exponent λ of a coupled system (5.1)-(5.2) as a function of coupling strength g . Letters A, B, C, D and E indicate windows with different periodic dynamics (see Fig. 5.4).	65
5.4	Examples of periodic dynamics each corresponding to a window with zero LLE in Fig. 5.3. The following values of synaptic conductance g were used: A - 0.005, B - 0.021, C - 0.042, D - 0.084, E - 0.102. . . .	66
5.5	Dynamics of the scaled membrane potentials x_1 and x_2 (top) and of the coupling strength g (bottom) in the cases of (a),(c) periodic and (b),(d) chaotic dynamics of the coupled system.	69
5.6	Example of the typical slow dynamics of the coupling strength. After the initial random-like behavior g gets on the stable limit cycle.	70
5.7	Largest Lyapunov exponent λ as a function of the initial conductance g_0 of the plastic synapse.	70
6.1	Time series of fixed point dynamics in a network. Time goes along the horizontal axis while identity of the neuron - along the vertical. Each horizontal line represents activity of one neuron. Level of neuronal activity is coded by grayscale with black corresponding to the quiet state ($x_i(t) = 0$) and white - to the maximally active state ($x_i(t) = 1$). . . .	76

6.2	Another example of a network with fixed point dynamics. In this case the period of transient chaotic dynamics was rather long. Time series are represented is the same way as in Fig. 6.1.	77
6.3	Example of a network with periodic dynamics. Time series are represented is the same way as in Fig. 6.1.	78
6.4	Another example of a network with periodic dynamics. In this case periodic dynamics was more complicated and had longer period. Time series are represented is the same way as in Fig. 6.1.	79
6.5	Example of a network with chaotic dynamics. Time series are represented is the same way as in Fig. 6.1.	80
6.6	Another example of a network with chaotic dynamics. Time series are represented is the same way as in Fig. 6.1.	81
6.7	Fraction of networks F with periodic (stars) or chaotic (squares) dynamics in simulations of 200-node cANN networks with node-to-node connection probability p	82
6.8	Smallest dynamical motifs with periodic (a) and chaotic (b-d) dynamics. Triangles indicate direction of the inhibitory connections.	83
6.9	Theoretical estimation of the dependence of fraction of frozen nodes p_f in the network on the density of connections p (solid line) and its values that were calculated from simulations (squares).	85
6.10	Fraction of networks F with either periodic or chaotic (triangles) and only chaotic (squares) dynamics in simulations of 200-node cANN networks with node-to-node connection probability p . Lines represent predictions based on the probability of occurrence of periodic (dashed line, Eq. (6.17)) and chaotic (solid line, Eq. (6.18)) motifs.	87
6.11	Bifurcation diagram depicting local maxima of $x_1(t)$ oscillations for a range of strengths w of the inhibitory connections in the first chaotic motif (Fig. 6.10(b)). Period doubling cascades start around $w = 0.7$ and $w = 2.5$	89

6.12	Projections of the five-dimensional phase space onto two-dimensional plane calculated for different strengths w of the inhibitory connections in the first chaotic motif (Fig. 6.10(b)). Period doubling bifurcations of the limit cycle are clearly seen.	90
------	--	----

List of Tables

3.1	Parameters for the learning and static synapse.	33
3.2	Experimental protocol for the synchronization assessment experiment. The neurons were recorded when uncoupled, coupled with a STDP synapse, uncoupled again and then coupled with a static synapse. Then we started over with a different presynaptic period T_1 and so on. Note that it is not important to use exactly the same presynaptic periods for STDP and static coupling as the postsynaptic neuron varies its intrinsic frequency over time anyways. Most experiments were done with the pro- tocol A of full 100 s coupling. Protocol B was used for intrinsically faster neurons to save experiment time and avoid damage to the preparation due to excessive forcing of the postsynaptic neuron.	38

Chapter 1

Introduction

1.1 The brain as a complex, multiscale system

Our brain is arguably one of the most complex dynamical systems in the Universe. It consists of more than 10^{11} neurons that are connected by approximately 10^{15} chemical and electrical synaptic connections. Each neuron in itself is an elaborate dynamical element with a number of diverse dynamical processes occurring on different timescales ranging from sub-milliseconds (opening and closing of single ionic channels) to seconds (flow of ‘slow’ ionic currents), minutes (changes in synaptic conductances), days (growth and development of new synaptic connections) and decades (death of neurons). The range of spatial scales on which these dynamical processes take place is also enormous – from micrometers (molecular and biochemical processes inside neurons) to millimeters (synaptic interactions in localized neuronal ensembles) and tens of centimeters (interactions between different areas of the brain).

One of the reasons for the spectacular progress of physics in the study of non-living matter is the presence of the so-called ‘separation of scales’ between fundamental forces of Nature. This separation has allowed physicists to split the study of the Universe into the separate analysis of the building blocks and the rules of their interaction at each ‘scale.’ However, when compared to its success in physics, the ‘separation of scales’ approach has had limited success so far when applied to complex living matter such as the brain. One of the stumbling blocks for this approach is the fact that many spatio-temporal dynamical processes in the brain operate on

several spatial and/or temporal scales, thus providing strong interactions between the scales. For example, neurons produce spikes (very short electrical pulses that carry information from neuron to neuron) whose timing is in some cases up to one millisecond precise [57, 102, 10]. On the other hand, there are examples showing that a lot of information is transmitted between neurons in the variations of the average firing rate [37, 15]. Those variations occur on the timescale of hundreds of milliseconds. The debate still rages among neuroscientists as to what is most important in the ‘neural code’ – precise spike timing or average firing rate? The emerging answer seems to indicate that both of them are essential and that their relative importance may depend on the situation and context [100, 63, 23, 55]. It is therefore impossible to separate temporal scales in this case and the dynamical processes with timescales from 1 ms to 100 ms should be analyzed simultaneously. This and other examples demonstrate that in most cases the proper way to harness the power of the ‘separation of scales’ approach to neural systems was not yet found. Moreover, it may turn out that it can not in principle be found and that scientists may have to deal with the problem of understanding the brain in its full integrity. It is not yet known when and how to ‘coarse-grain’ in order to move from one ‘scale’ to another, as well as if this procedure is applicable at all.

As just described, the brain is a very complex high-dimensional dynamical system with mixed spatial and temporal scales and, probably, has to be studied as such. However, the paradox of the situation is in the fact that it is difficult for us to proceed with studying the brain as a whole. Present theoretical and experimental tools are in most cases not inadequate for such an approach to be practical. Hence, in many cases we have to resort to the tried-and-true reductionist approach of physics and mathematics. The purpose then is to learn as much as possible about the workings of the brain at each ‘scale’ and to develop new experimental techniques and theoretical tools that would help bridge the scales. The hope is that with the help of these connecting tools it will be possible one day to combine the wealth of collected information into one unified ‘Theory of the brain.’

1.2 Thesis overview

Today, while still in its infancy, theoretical neuroscience presents many exciting problems for an aspiring theorist to tackle. For the reasons described above, most of these problems are limited to a specific ‘scale’ and are rather ‘narrow’ and non-general from a point of view of a typical physicist. Luckily, a lot of progress had been made in understanding of the building blocks at each ‘scale,’ be it ionic channels, single neurons, or brain areas. This progress allows theorists to start addressing more general questions about interactions between the scales and about structures and dynamical processes that emerge as a result of these interactions.

This thesis is focused on addressing questions about the emergence of two of the most intriguing properties of neural systems. The first one is the question about the origin of the robustness of the dynamical phenomena such as synchronization and regularization of oscillations in neural circuits. The second one is the question about the nature of the connection between the structure of local neural connectivity and the properties of global dynamics of neural networks. As it turns out, answers to both of these questions require the study of the mechanisms that mediate interactions between the processes occurring on different temporal (in the first case) and spatial (in the second case) scales.

In Chapters 2-5 the influence of slow synaptic learning mechanisms on the fast dynamical processes in neural circuits such as synchronization of spikes and bursts of spikes is studied. Unlike in the usual studies of dynamical systems in which systems’ parameters are kept fixed, some parameters of the model dynamical systems describing these neural circuits are changing on slow timescales according to biologically inspired learning rules. The unexpected result of these studies is that learning may greatly improve robustness of the dynamical processes such as synchronization of oscillations and regularization of chaos in model neural circuits. Even more unexpectedly, as Chapter 5 indicates, natural learning mechanisms are able to transform structurally unstable (in the sense of the theory of bifurcations) and sensitive to parameter perturbations dynamical systems into structurally stable ones. This oc-

curs when the parameters to the values of which the system is very sensitive are allowed to change slowly according to appropriate learning rules. Another example of this phenomenon was recently experimentally demonstrated by David Tank and his collaborators in the study of the oculomotor integrator of goldfish. Oculomotor integrator is a neural circuit that was found to be structurally unstable in the modeling studies as it required very precise tuning of the feedback. Experimental studies in the Tank's group have shown that the circuit is indeed very sensitive and can be induced to become unstable. Experiments showed, however, that through the 'slow timescale' feedback-mediated learning mechanism the integrator usually returns from the perturbed unstable regime to the stable operational regime [58].

At present, the lack of understanding of the connection between the 'scale' of single neurons and the 'scale' of neuronal networks appears to be one of the major bottlenecks in our understanding of the brain. Brain networks are usually very dense and highly connected, with thousands and sometimes millions neurons talking to each other simultaneously inside a localized network. And while a lot is known and understood about the properties and functions of single neurons and brain areas, the way in which the neurons 'combine their efforts' when connected in networks and brain areas is in many cases not well understood. There are at least several reasons for this lack of understanding. First, experimental techniques that would allow one to measure all that activity with an adequate temporal and spatial resolution are still present only in very remote dreams of neuroscientists. Second, there is a lack of theoretical methods that would allow a meaningful analysis of high-dimensional spatio-temporal dynamics in neural networks to be carried out. In Chapter 6 of the thesis an attempt is made to address the latter problem through the development of a new theoretical tool that may be used to improve our understanding of the connection between local structure and overall dynamics of large neural networks.

1.3 Summary of work

In Chapter 2 we study the synchronization of two model neurons coupled through a synapse having an activity-dependent strength. This synapse follows the rules of spike-timing-dependent plasticity (STDP). We show that this plasticity of the coupling between neurons produces enlarged frequency locking zones and results in synchronization that is more rapid and much more robust against noise than classical synchronization arising from connections with constant strength. We also present a simple discrete map model that enables deep understanding of this phenomenon and demonstrates its generality. A concise presentation of the material of this chapter had been published in [110].

In Chapter 3 we demonstrate that spike-timing-dependent plasticity enhances synchronization (entrainment) in a hybrid circuit composed of a spike generator, a dynamic clamp emulating an excitatory, plastic synapse, and a chemically isolated neuron from the *Aplysia* abdominal ganglion. Fixed phase entrainment of the *Aplysia* neuron to the spike generator is possible for a much wider range of frequency ratios, and is more precise and more robust with the plastic synapse, than with a non-plastic synapse of comparable strength. Further analysis in a computational model of Hodgkin-Huxley type neurons reveals the mechanism behind this significant enhancement in synchronization. The experimentally observed STDP plasticity curve appears to be designed to adjust synaptic strength to a value suitable for stable entrainment of the postsynaptic neuron. We argue that one functional role of STDP might therefore be to facilitate synchronization or entrainment of non-identical neurons. Biological experiments described in this chapter were performed by Thomas Nowotny. Most of its material had been published in [69].

In Chapter 4 we study the entrainment of a heterogeneous network of electrically coupled neurons by synaptically mediated periodic stimulation. We demonstrate by computer simulations that input synapses with spike-timing-dependent plasticity greatly enhance the coherence of spiking activity in the network as compared to the case of input with constant strength. We also show that synchronization in the

network stimulated through STDP synapses is much more robust to the variability of network properties. We speculate that the observed mechanism may play a role in synchronizing the activity of a hippocampal network. Most of the material of this chapter had been published in [108].

In Chapter 5 we suggest a new type of artificial synaptic connection that combines the best properties of electrical and chemical synapses: the fast reaction of a gap junction and the plasticity of a chemical synapse. Based on the mathematical analysis and computer simulations we show that such plastic electrical synapse regularizes chaos in the minimal neural circuit consisting of two chaotic bursting neurons and leads to structural stability of the regularized state. A concise presentation of the material of this chapter will be published shortly [109].

In Chapter 6 we suggest a new approach to the study of spatio-temporal network dynamics which is based on the analysis of dynamical motifs – small subnetworks with periodic and chaotic dynamics. We simulate randomly connected neural networks and, with increasing density of connections, observe the transition from quiescence to periodic and chaotic dynamics. This transition is explained by the appearance of dynamical motifs in the structure of these networks. We also observe domination of periodic dynamics in simulations of spatially distributed networks with local connectivity and explain it by the absence of chaotic and the presence of periodic motifs in their structure. A concise presentation of the material of this chapter will be published shortly [107].

Chapter 2

Robustness and enhancement of neural synchronization by activity-dependent coupling

2.1 Introduction

Synchronous activity among neurons or neuronal ensembles is a robust phenomenon observed in many regions of the brain, in sensory systems and in other neural networks. With constant synaptic connections, the regions of parameter space in which neural synchronization arises are quite narrow and the origin of the observed robustness of synchronization is not clear. It is known that many neurons in the cortex, in the cerebellum and in other neural systems are coupled through excitatory synaptic connections whose strength can be altered through activity-dependent plasticity. Indeed, this plasticity is widely thought to underlie learning processes, and in itself constitutes a broadly interesting phenomenon. Here we discuss its role in the synchronization of neurons in a network.

There have been recent experimental advances in the understanding of such plasticity, and, in particular, of the critical dependence on timing in presynaptic and postsynaptic signaling. Two manifestations of this kind of synaptic plasticity are spike-timing-dependent plasticity (STDP) [61, 11] seen in excitatory connections between neurons, and its inverse, observed, for example, in the connections between excitatory and inhibitory neurons in the electrosensory lobe of fish [9]. The con-

nections between excitatory neurons through inhibitory interneurons are typical in sensory systems [52, 77] and cerebral cortex [7]. These also express synaptic plasticity [71] and play an important role in the control and synchronization of neural ensembles in hippocampus.

We report here on the synchronization of two model neurons coupled through a synapse with STDP or inverse STDP. We demonstrate that such coupling leads to neural synchronization which is more rapid, more flexible and much more robust against noise than synchronization mediated by constant strength connections. (For reviews, see [30, 24, 19]). We also build a simple discrete map that illustrates the enhancement of synchronization by activity-dependent coupling. The map allows us to speculate about the general applicability of learning-enhanced synchronization.

2.2 Description of the model

We consider here the simplest neural network: two neurons with unidirectional, activity-dependent excitatory synaptic coupling. Each neuron is described by Hodgkin-Huxley equations [40] with sodium (I_{Na}), potassium (I_K) and leak (I_{leak}) currents:

$$C \frac{dV_i(t)}{dt} = -I_{Na}(t) - I_K(t) - I_{leak}(t) - I_{syn}(t) + I_{stim}, \quad (2.1)$$

where $i = 1, 2$, the leak current is given by $I_{leak}(t) = g_L(V_i(t) - E_L)$, $I_{Na}(t)$ and $I_K(t)$ are taken from [94]:

$$I_{Na}(t) = g_{Na} m_i(t)^3 h_i(t) (V_i(t) - E_{Na}), \quad (2.2a)$$

$$I_K(t) = g_K n_i(t)^4 (V_i(t) - E_K), \quad (2.2b)$$

with each of the activation and inactivation variables $y_i(t) = \{n_i(t), m_i(t), h_i(t)\}$ satisfying first-order kinetics

$$\frac{dy_i(t)}{dt} = \alpha_y(V_i(t))(1 - y_i(t)) - \beta_y(V_i(t))y_i(t), \quad (2.3)$$

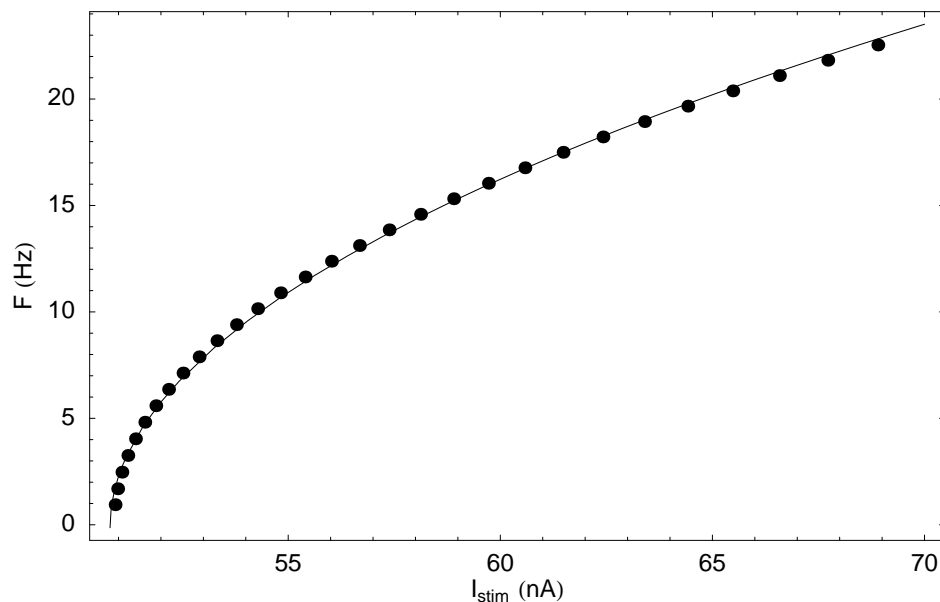


Figure 2.1: Dependence of spiking frequency F on the input current I_{stim} for the model neuron (dots). Solid line represents its fit given by equation (2.5).

where

$$\alpha_n = 0.032(-50 - V)/(\exp((-50 - V)/5) - 1), \quad (2.4a)$$

$$\beta_n = 0.5 \exp((-55 - V)/40), \quad (2.4b)$$

$$\alpha_m = 0.32(-52 - V)/(\exp((-52 - V)/4) - 1), \quad (2.4c)$$

$$\beta_m = 0.28(25 + V)/(\exp((25 + V)/5) - 1), \quad (2.4d)$$

$$\alpha_h = 0.128 \exp((-48 - V)/18), \quad (2.4e)$$

$$\beta_h = 4/(\exp((-25 - V)/5) + 1). \quad (2.4f)$$

The following values of the parameters were used in the model: membrane capacitance $C = 1.43 \cdot 10^{-4} \mu F$, leak conductance $g_L = 0.0267 \mu S$, leak potential $E_L = -63.55 mV$, conductance of sodium channels $g_{Na} = 7.15 \mu S$, reversal potential of sodium channels $E_{Na} = 50 mV$, conductance of potassium channels $g_K = 1.43 \mu S$, reversal potential of potassium channels $E_K = -95 mV$.

In this model each neuron receives a constant input current I_{stim} that forces it to spike with a constant, I_{stim} -dependent frequency (see Fig. 2.1). This dependence can

be approximated by

$$f = 5.4\sqrt{I_{stim} - 50.8} - 0.146, \quad (2.5)$$

which was inverted and used to control spiking frequencies by injecting input currents of appropriate strength.

The second neuron is synaptically driven by the first via an excitatory current that is dependent on the postsynaptic $V_2(t)$ and presynaptic $V_1(t)$ membrane voltages (reversal potential is taken to be zero):

$$I_{syn}(t) = g(t)S(t)V_2(t), \quad (2.6)$$

where $S(t)$ is the fraction of open synaptic channels. We describe its dynamics by a typical first-order kinetic scheme with rates of synaptic binding and unbinding $\alpha = 10 \text{ ms}^{-1}$ and $\beta = 0.2 \text{ ms}^{-1}$:

$$\frac{dS(t)}{dt} = \alpha(1 - S(t))H(V_1(t)) - \beta S(t), \quad (2.7)$$

where $H(V_1(t)) = (1 + \tanh(10V_1(t)))/4$.

The time-dependent synaptic conductance $g(t)$ is conditioned by the dynamics of the pre- and postsynaptic neurons. We consider two types of activity-dependent couplings: (1) an excitatory synapse with STDP, and (2) an excitatory synapse with inverse STDP. Through STDP $g(t)$ changes by $\Delta g(t)$ which is a function of the time difference $\Delta t = t_{post} - t_{pre}$ between the times of post- and presynaptic spikes. We use the additive update rule

$$\Delta g(t) = G(\Delta t) = A \text{sign}(\Delta t) \exp(-\gamma|\Delta t|) \quad (2.8)$$

for STDP, and $\Delta g(t) = -G(\Delta t)$ for inverse STDP (see Fig. 2.2). The following values of parameters were used: $A = 4 \text{ nS}$ and $\gamma = 0.15 \text{ ms}^{-1}$.

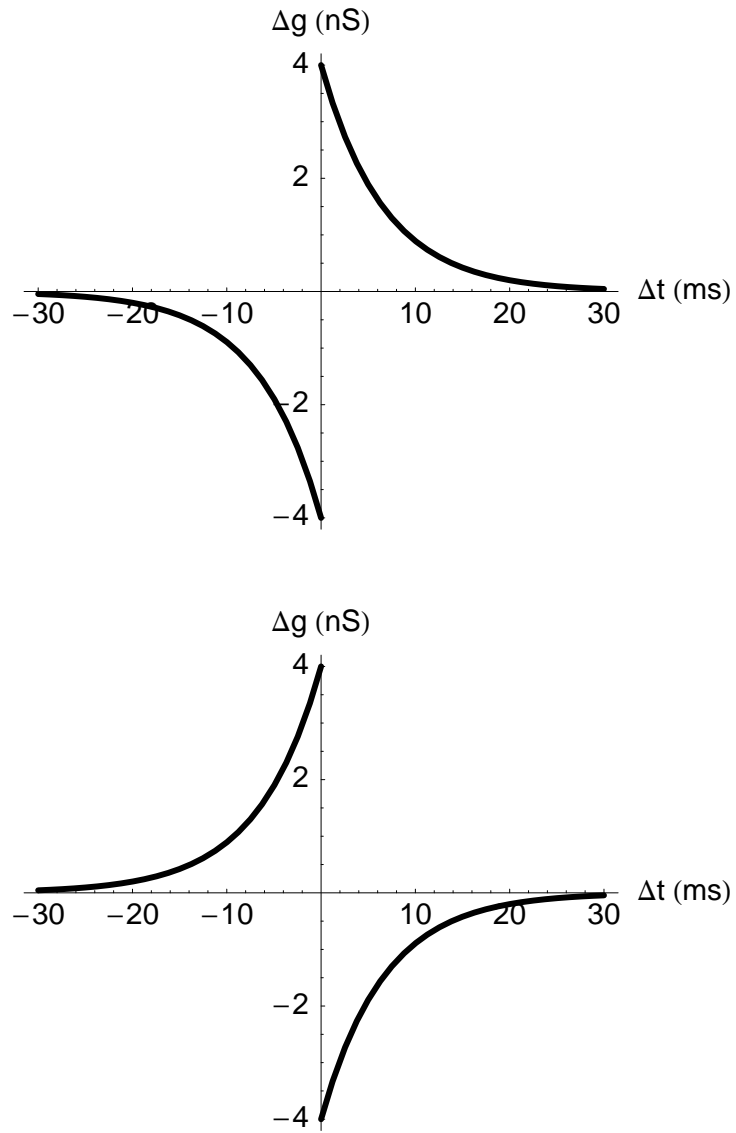


Figure 2.2: Plots of the update rule (2.8) in the cases of (top) STDP and (bottom) inverse STDP. Only pairs of the nearest pre- and postsynaptic spikes are taken for calculation of Δg .

2.3 Results

2.3.1 Enhancement of synchronization

We studied the synchronization properties of the system coupled through an inverse STDP synapse by setting the autonomous period of the postsynaptic neuron to 15

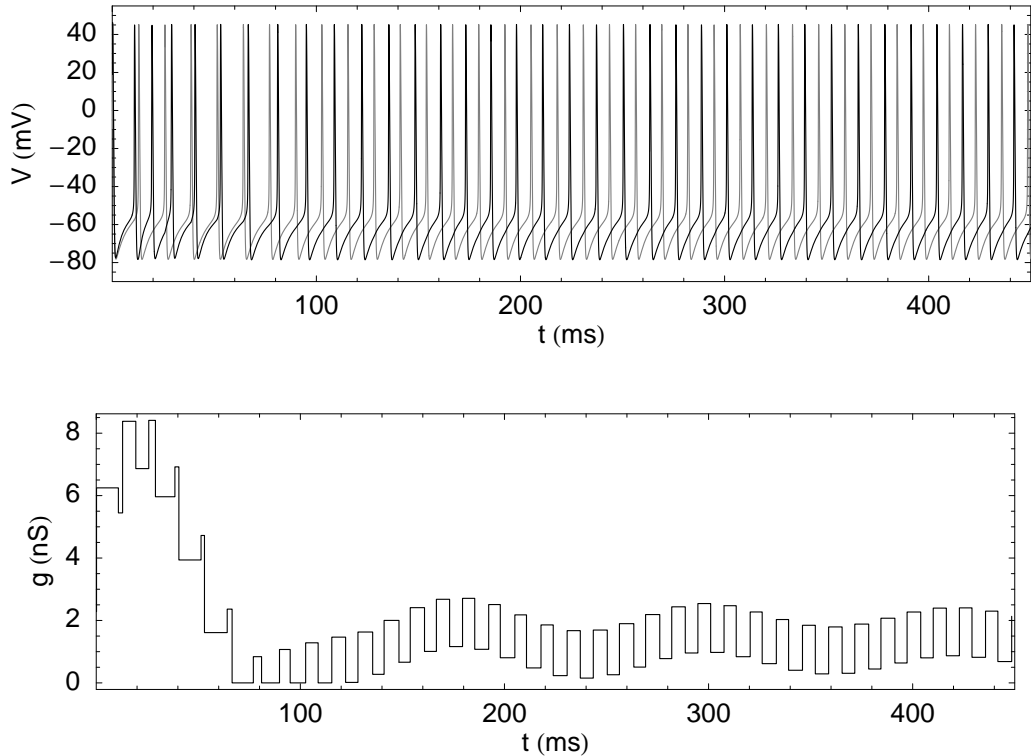


Figure 2.3: Synchronization of the neurons with inverse STDP coupling. (top) Membrane voltages of presynaptic (dotted line) and postsynaptic (solid line) neurons. Postsynaptic neuron was initially spiking faster than the presynaptic one due to relatively strong coupling between them. Coupling strength decreased (bottom) and synchronized state was reached.

ms and then evaluating the actual period of its oscillation T_2 as a function of the imposed autonomous oscillation period T_1 of the presynaptic neuron. Figures 2.3 and 2.4 illustrate typical examples of such simulations. In these examples the initial coupling strength $g(0)$ was set to $0.005 \mu S$. In the example that is presented in Fig. 2.3 the period of the driving neuron T_1 was set to 13 ms. Because of the mismatch in spiking periods the neurons were not initially synchronized. Even though their autonomous spiking periods were very similar, the postsynaptic neuron was in fact driven too strongly for 1:1 frequency locking to occur. Surprisingly, as the bottom panel of Fig. 2.3 illustrates, dynamic interplay between potentiation and depression of synaptic strength led to its overall decrease and stabilization around $0.001 \mu S$. As the top panel of the plot indicates, such strength was appropriate for 1:1 synchronization.

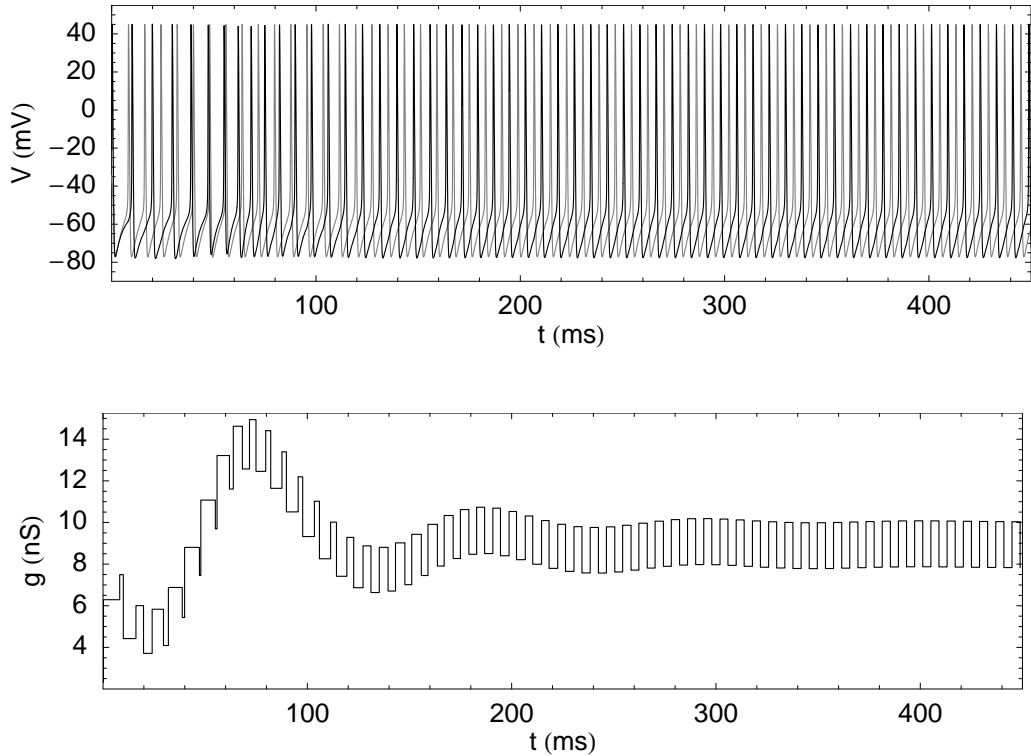


Figure 2.4: Same as in Fig. 2.3, but with postsynaptic neuron initially spiking slower than the presynaptic one (top) due to relatively weak coupling between them. Coupling strength increased (bottom) and synchronized state was reached.

In another example, presented in Fig. 2.4, the period of the driving neuron T_1 was set to 8.5 ms. In this case the postsynaptic neuron was not driven strongly enough for synchronization to occur. As in the previous example, STDP dynamics led to a change in synaptic strength (increase), necessary for synchronization to occur.

The above examples indicate that STDP-mediated learning may induce adaptation of synaptic strength to the level that is appropriate for synchronization of neurons with different intrinsic spiking frequencies. To study this phenomenon in more detail series of simulations were performed for the range of presynaptic periods T_1 and the steady-state values of synaptic strength and postsynaptic periods T_2 were recorded. Fig. 2.5 shows the ratio of pre- and postsynaptic periods T_1/T_2 as a function of T_1 in two cases: (a) synaptic coupling with constant strength $0.008 \mu S$ and (b) synaptic coupling with inverse STDP. In the later case the steady-state coupling strength depends on the ratio of neuronal frequencies (c). Its average over all T_1 values is

$0.002 \mu S$, which is much lower than the strength in the case of constant coupling.

In Fig. 2.5(a) we see the usual ‘Devil’s Staircase’ associated with frequency locking domains of a driven nonlinear oscillator. Only frequency locking with ratios 1:1, 2:1, 3:1, and 4:1 leads to synchronization plateaus with significant width. In Fig. 2.5(b) we see that the synchronization domains are substantially broadened due to activity-dependent coupling, especially for $T_1/T_2 = 1$. Some synchronization plateaus exhibit multistability, which we confirmed by observing the associated hysteresis. These results show that even a weak, but adaptive connection with strength that is determined dynamically is able to greatly enhance and enrich synchronization.

Close to the boundary of every synchronization zone the transition from quasi-periodic oscillations to complete frequency locking was observed. This phenomenon is related to the strong nonlinearity of the neuronal oscillations and is illustrated in Fig. 2.6, where projections of the phase portrait of the system for the cases of (a) absence, (b,c) non-exact and (d) exact 2:1 frequency locking are plotted.

Our simulations show that synchronization with an STDP synapse is not as stable as with the inverse STDP. If the periodic spike sequence is long enough, the strength of the STDP synapse shows instability and starts to grow without limit, which is consistent with the discussion in [81].

2.3.2 Robustness of synchronization

The robustness of the enhanced synchronization in the presence of noise was studied by adding zero mean Gaussian white noise to the membrane currents of each neuron. The behavior of the system with RMS noise amplitudes $\sigma = 0.01, 0.05, 0.1$, and 0.5 nA was examined.

For $\sigma = 0.01$ nA no phase-locking plateaus were destroyed. At $\sigma = 0.05$ nA the 4:1 plateau became distorted. Larger σ sequentially eliminated synchronization plateaus until only the 1:1 plateau remained. The 1:1 plateau was seen for all σ . Fig. 2.7 illustrates the effect of the noise on synchronization when $\sigma = 0.1$ nA with (a) constant and (b) inverse STDP coupling. While in (a) most of the plateaus

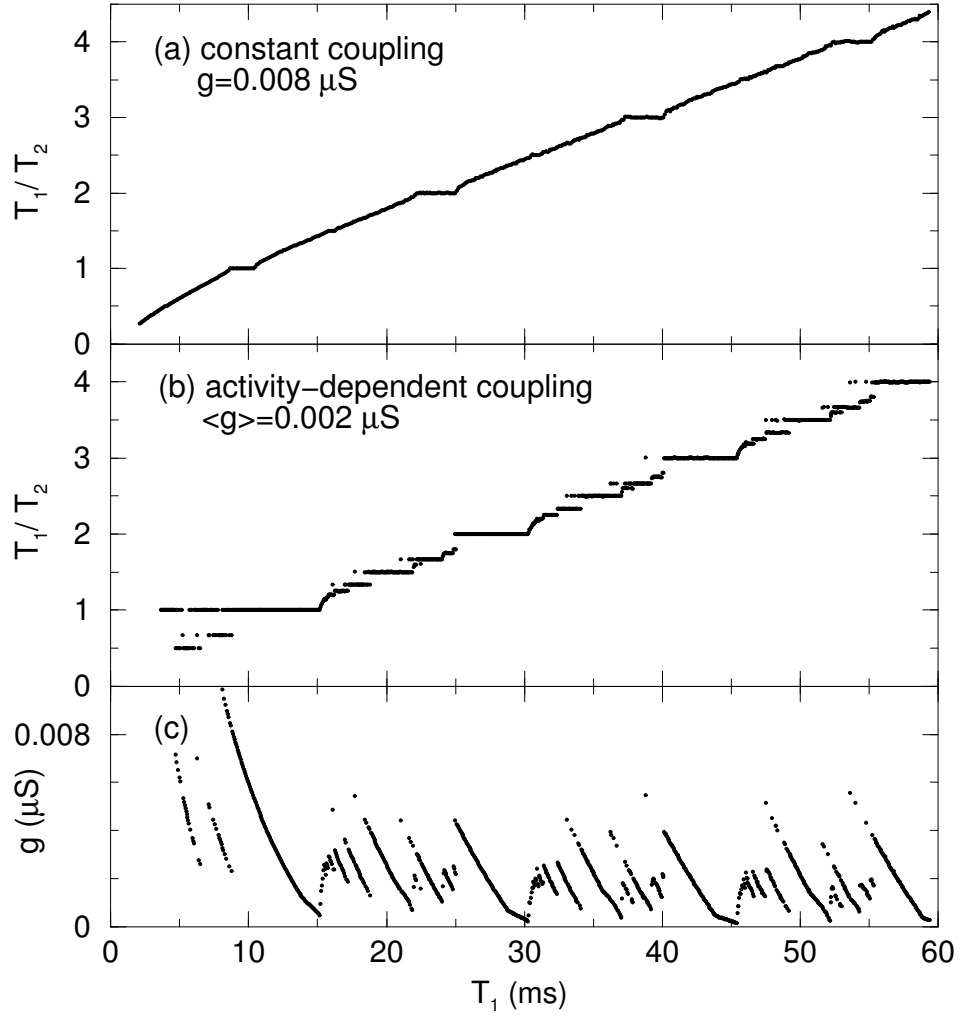


Figure 2.5: Devil's Staircase for (a) constant synaptic strength and (b) synaptic strength varying according to inverse STDP coupling. T_1 and T_2 are the observed periods of the presynaptic (driving) neuron and postsynaptic (driven) neuron respectively. In (c) the final value of synaptic strength is displayed.

have disappeared, in (b) the 1:1, the 2:1 and even the 3:1 frequency locking regimes remained. In sharp distinction to classical synchronization, frequency locking through activity-dependent coupling is significantly more robust in the presence of noise.

2.3.3 Phase diffusion

To understand the mechanisms behind such a remarkable robustness noise-induced diffusion of oscillation phase was studied. For $\sigma = 0.5 \text{ nA}$ Fig. 2.8(a) shows that in

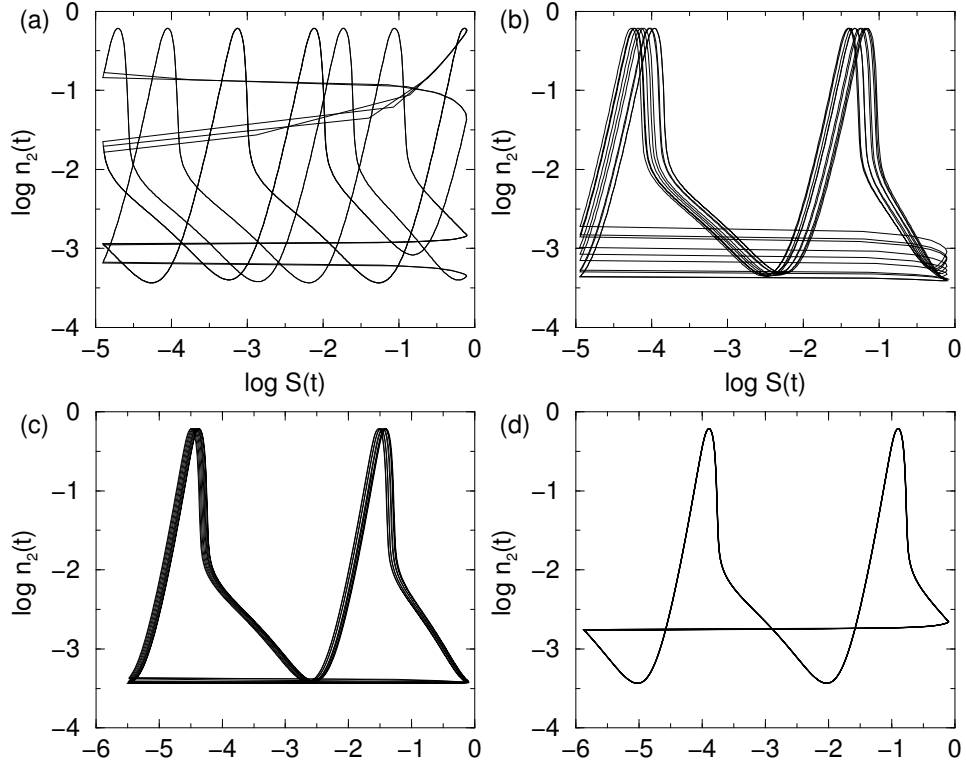


Figure 2.6: Two-dimensional projections of the phase portraits of the system for different values of T_1 : (a) 24.2 ms, (b) 24.33 ms, (c) 27 ms, and (d) 29 ms. The autonomous oscillation period of the postsynaptic neuron was 15 ms.

the case of 1:1 synchronization and coupling with constant strength $0.008 \mu S$ noise-induced phase diffusion results in 2π phase slips that destroy synchronized state. Quite contrary, Fig. 2.8(b) shows that in the case of activity-dependent coupling phase slips are absent and the phase difference does not increase. In this particular case the strength of coupling varied around the mean of $0.0064 \mu S$ with standard deviation of $0.0026 \mu S$.

In Fig. 2.9 the average rate of phase slips for different amplitudes of the noise is plotted. In line with the above observation we see that in the case of activity-dependent coupling (dashed line) phase slips are suppressed in a wide range of noise amplitudes. This suppression of phase slips is the primary mechanism responsible for robustness of synchronization mediated by activity-dependent coupling. After the introduction of a discrete map model this mechanism will be discussed in more detail.

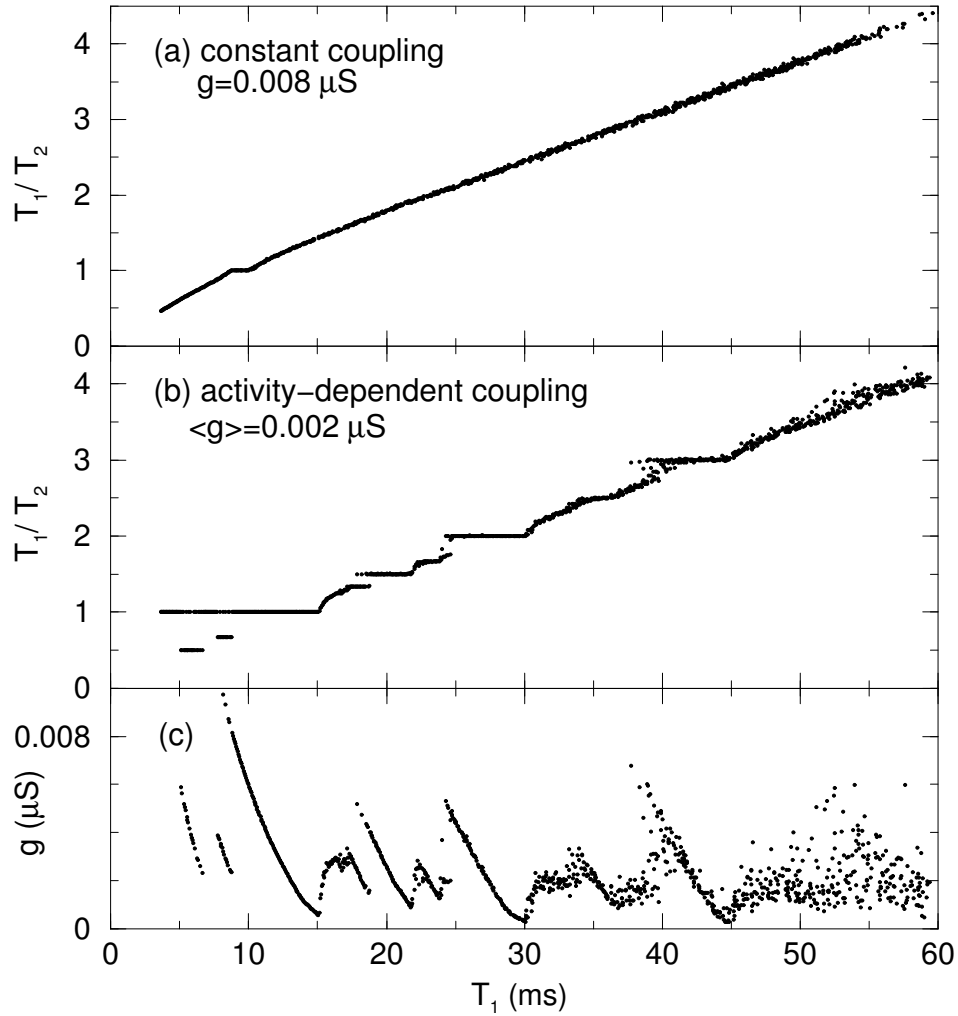


Figure 2.7: Same as Fig. 2.5, but with zero mean, Gaussian, white noise with $\sigma = 0.1$ nA added to the membrane currents.

2.3.4 Synchronization of bursts

Fig. 2.10 shows an example of synchronization through an activity-dependent synapse in the realistic case when the first neuron produces bursts of spikes and the autonomous postsynaptic neuron spikes irregularly. It illustrates that synchronization through an STDP synapse is very fast; even a few spikes are enough for the frequency locking to establish itself. Neurons in the same setup but with constant coupling synchronize much slower and *only* if the strength of the connection is appropriate for the given ratio of their frequencies. Hence, activity-dependent synapses allow adaptation

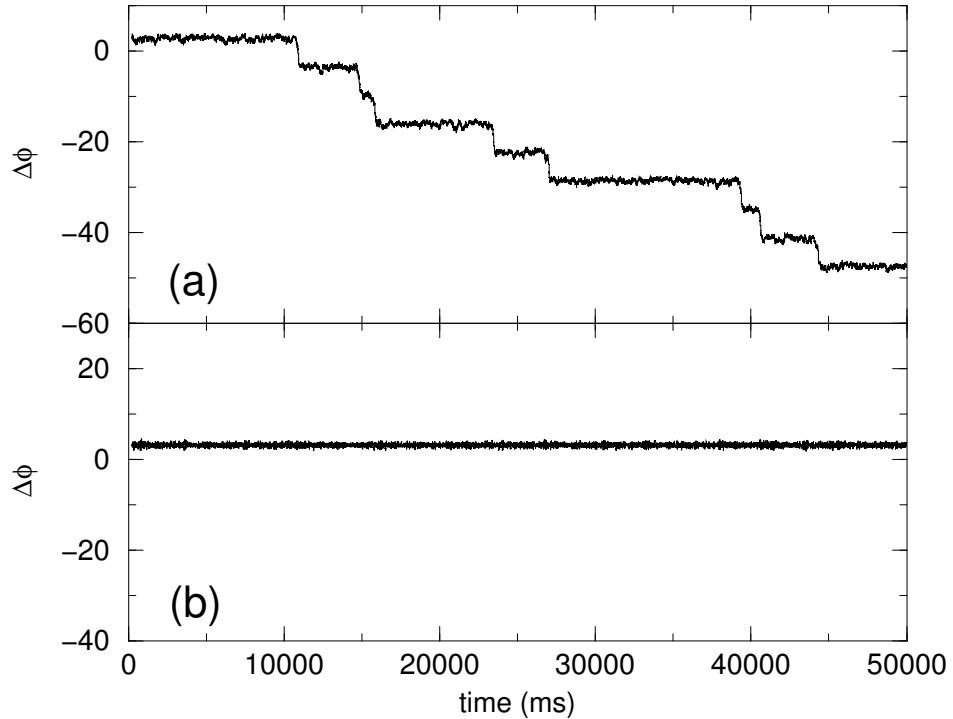


Figure 2.8: The difference of oscillation phases of two neurons as a function of time in the cases of (a) constant and (b) activity-dependent coupling.

‘on the run,’ synching a postsynaptic neuron to the firing properties of its presynaptic partner.

2.3.5 Discrete time map model

To understand the above results in a general way a discrete time map model of periodic spike generators with STDP-like coupling that accounts for the dependence of the coupling strength on the activity of generators was constructed in the following way. Take T_1^0 and T_2^0 as the autonomous periods of the first and second generators. As a result of unidirectional coupling, the period of the second generator will change by some amount ΔT each time it receives a spike from the first generator. Assuming initial phases to be 0, the time of the $n + 1$ -st spike of the first generator and $m + 1$ -st

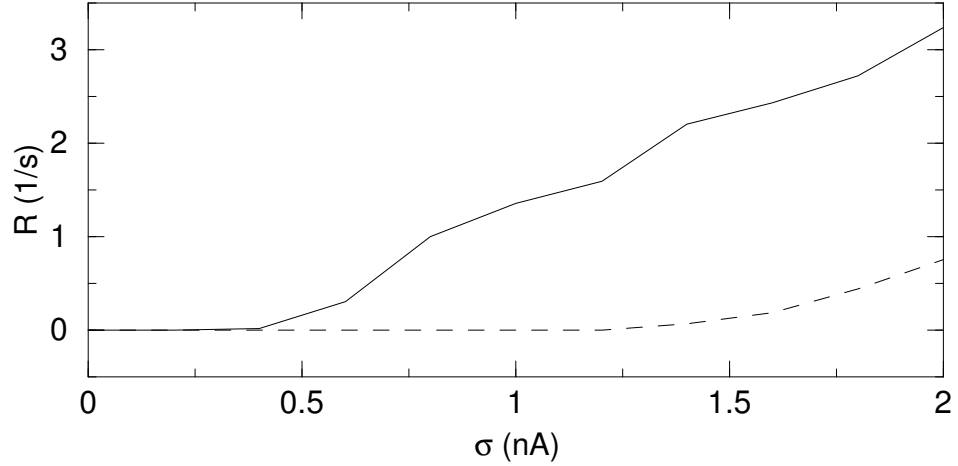


Figure 2.9: Average rate of phase slips as a function of RMS noise amplitude for the case of 1:1 synchronization and constant (solid line) or activity-dependent (dashed line) coupling.

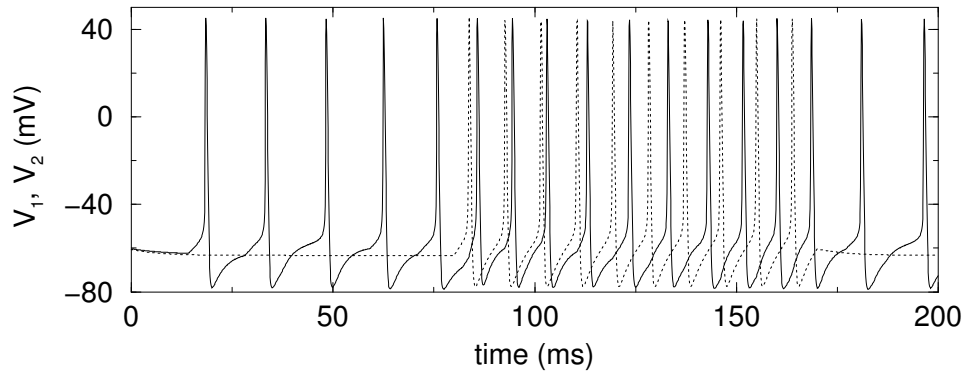


Figure 2.10: Out-of-phase rapid locking of the postsynaptic neuron membrane voltage (solid line) to a burst of spikes from the presynaptic neuron (dotted line). The frequency of the second neuron changes significantly and the transient period before complete synchronization is short.

spike of the second generator are taken to satisfy

$$t_{n+1}^{(1)} = t_n^{(1)} + T_1^0, \quad (2.9a)$$

$$t_{m+1}^{(2)} = t_m^{(2)} + T_2^0 - \Delta T_{m,n}, \quad (2.9b)$$

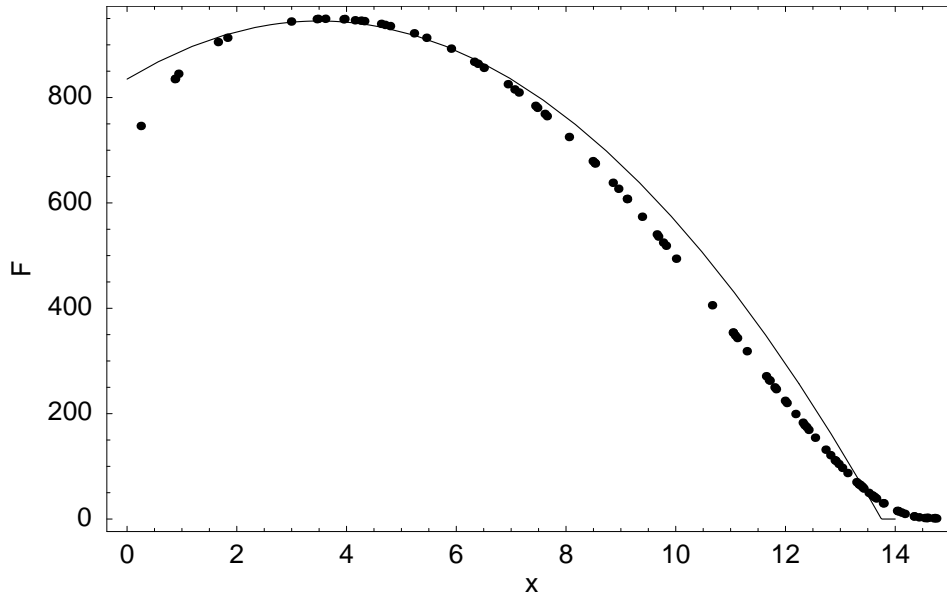


Figure 2.11: Phase response curve of the model neuron that was rescaled by synaptic conductance, $g = 3.6 \cdot 10^{-9} S$ in this case (dots). Solid line represents its approximation by Eq. (2.11).

where n and m are such that $t_m^{(2)} \leq t_n^{(1)} \leq t_{m+1}^{(2)}$. In general, $\Delta T_{m,n}$ would be a function of T_1^0 , T_2^0 , $t_n^{(1)}$, $t_m^{(2)}$, and the coupling strength $g_{m,n}$. We argue that the two main variables here are $t_n^{(1)} - t_m^{(2)}$, and $g_{m,n}$. In the case of weak coupling $\Delta T_{m,n}$ can be approximated by

$$\Delta T_{m,n} = g_{m,n} F(t_n^{(1)} - t_m^{(2)}), \quad (2.10)$$

where the function $F(x)$ is the rescaled phase response curve [104] of the model Hodgkin-Huxley neuron. To obtain results quantitatively comparable with our neuronal model, it was fitted by a non-negative quadratic function that describes phase response of our model neurons:

$$F(x) = 835 + 63x - 9x^2 \quad (2.11)$$

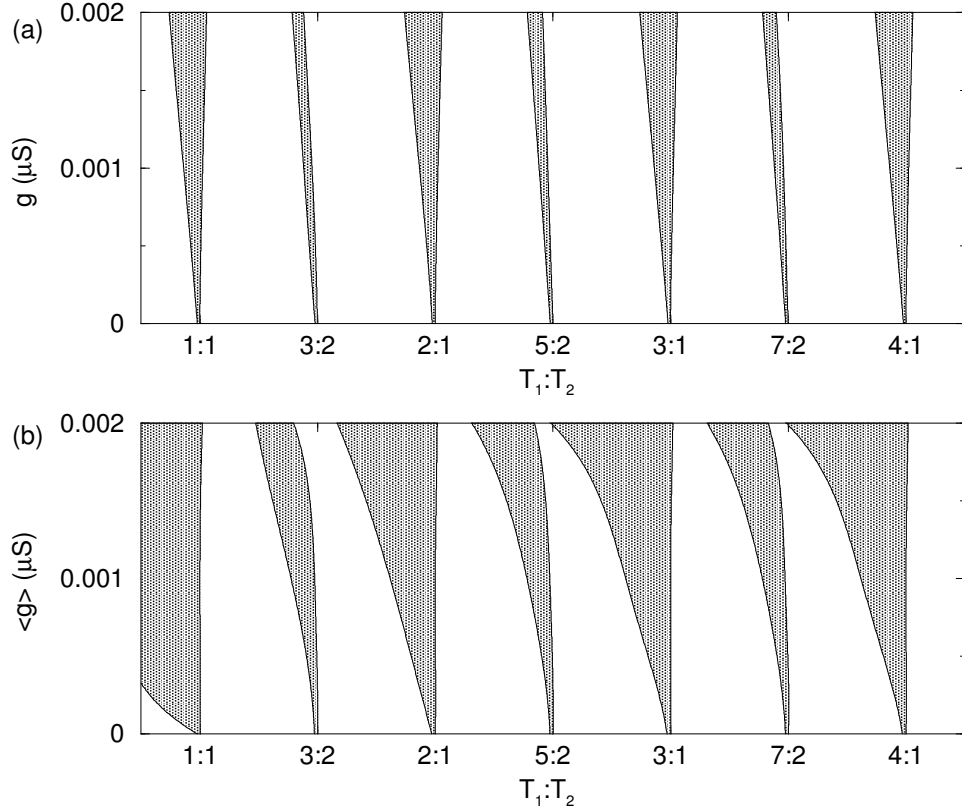


Figure 2.12: Arnold's Tongues calculated for the discrete map model with (a) constant and (b) activity-dependent coupling. $T_2^0 = 13$ ms.

for $0 \leq x \leq T_2^0$ and 0 otherwise (see Fig. 2.11). $g_{m,n}$ in equation (2.10) obeys the inverse STDP update rules (see Eq. (2.8)):

$$g_{m+1,n} = g_{m,n} - G(t_{m+1}^{(2)} - t_n^{(1)}), \quad (2.12a)$$

$$g_{m,n} = g_{m,n-1} - G(t_m^{(2)} - t_n^{(1)}), \quad (2.12b)$$

where, as before, n and m are such that $t_m^{(2)} \leq t_n^{(1)} \leq t_{m+1}^{(2)}$. Fig. 2.12 shows the Arnold's Tongues calculated for the map (2.9-2.12) in the cases of (a) constant and (b) inverse STDP coupling. As with the model neurons, we see that activity-dependent coupling greatly enlarges the zones of synchronization.

This discrete map can be further analyzed to find its fixed points corresponding to $n : m$ synchronization and to examine their stability. We present here the case

of 1:1 synchronization. Then $m = n$, and the system of equations (2.9-2.12) can be written in the following simple form:

$$\tau_{n+1} = \tau_n + T_1^0 - T_2^0 + g_n F(\tau_n), \quad (2.13a)$$

$$g_{n+1} = g_n - G(T_1^0 - \tau_{n+1}) - G(-\tau_{n+1}), \quad (2.13b)$$

where $\tau_n = t_n^{(1)} - t_n^{(2)}$. The fixed points g_f and τ_f of (2.13) are given by

$$g_f = (T_2^0 - T_1^0)/F(\tau_f), \quad (2.14a)$$

$$0 = G(T_1^0 - \tau_f) + G(-\tau_f). \quad (2.14b)$$

In order to calculate stability of these fixed points let us follow the dynamics of small variations $(\delta\tau, \delta g)$ around the equilibrium (τ_f, g_f) . From (2.13) we obtain

$$\delta\tau_{n+1} = \delta\tau_n + F(\tau_f)\delta g_n + g_f \left. \frac{dF(\tau)}{d\tau} \right|_{\tau_f} \delta\tau_n, \quad (2.15a)$$

$$\delta g_{n+1} = \delta g_n + \left(\left. \frac{dG(\tau)}{d\tau} \right|_{T_1^0 - \tau_f} + \left. \frac{dG(\tau)}{d\tau} \right|_{-\tau_f} \right) \delta\tau_{n+1}. \quad (2.15b)$$

Substituting (2.15a) into (2.15b) and rewriting (2.15) in matrix form we get

$$\begin{pmatrix} \delta\tau_{n+1} \\ \delta g_{n+1} \end{pmatrix} = \begin{pmatrix} 1 + g_f A & F(\tau_f) \\ (1 + g_f A)B & 1 + F(\tau_f)B \end{pmatrix} \begin{pmatrix} \delta\tau_n \\ \delta g_n \end{pmatrix}, \quad (2.16)$$

where

$$A = \left. \frac{dF(\tau)}{d\tau} \right|_{\tau_f} \quad \text{and} \quad B = \left(\left. \frac{dG(\tau)}{d\tau} \right|_{T_1^0 - \tau_f} + \left. \frac{dG(\tau)}{d\tau} \right|_{-\tau_f} \right). \quad (2.17)$$

As it is well known from the theory of stability, the equilibrium (τ_f, g_f) of (2.13) is stable if and only if

$$-1 < \lambda_{1,2} < 1, \quad (2.18)$$

where $\lambda_{1,2}$ are the eigenvalues of the Jacobian in (2.16). They are given by

$$\lambda_{1,2} = \frac{1}{2} \left(2 + g_f A + F(\tau_f) B \pm \sqrt{(2 + g_f A + F(\tau_f) B)^2 - 4(1 + g_f A)} \right). \quad (2.19)$$

Clearly, $\lambda_1 > \lambda_2$ and, hence, Eq. (2.18) implies that

$$g_f A + F(\tau_f) B + \sqrt{(2 + g_f A + F(\tau_f) B)^2 - 4(1 + g_f A)} < 0, \text{ and} \quad (2.20a)$$

$$g_f A + F(\tau_f) B - \sqrt{(2 + g_f A + F(\tau_f) B)^2 - 4(1 + g_f A)} > -4. \quad (2.20b)$$

Solving (2.20b) we obtain the following conditions:

$$g_f A + F(\tau_f) B + 4 > 0 \text{ and } 3g_f A + F(\tau_f) B + 6 > 0, \quad (2.21)$$

which are always satisfied since both $g_f A$ and $F(\tau_f) B$ are of the order 10^{-3} . Meanwhile, the condition (2.20a) is equivalent to

$$F(\tau_f) B > 0, \quad (2.22a)$$

$$g_f A + F(\tau_f) B < 0. \quad (2.22b)$$

Recalling (2.17) we see that stability of the synchronized state depends crucially on the forms of the STDP curve $G(t)$ and of the scaled phase response curve $F(\tau)$. Substituting the value of B we see that (2.22a) is equivalent to

$$F(\tau_f) \left(\left. \frac{dG(\tau)}{d\tau} \right|_{T_1^0 - \tau_f} + \left. \frac{dG(\tau)}{d\tau} \right|_{-\tau_f} \right) > 0, \quad (2.23)$$

which for the STDP curve (2.8) gives

$$-\gamma F(\tau_f) A (e^{-\gamma(T_1^0 - \tau_f)} + e^{-\gamma\tau_f}) > 0. \quad (2.24)$$

This condition will be satisfied in the following cases:

(a) $F(\tau_f) > 0$ (type I neurons) and $A < 0$ (inverse STDP),

(b) $F(\tau_f) < 0$ (type II neurons) and $A > 0$ (normal STDP).

Hence, stable synchronization of the considered in this chapter type I neurons (for which $F(\tau)$ is non-negative) is only possible with inverse STDP. This explains mentioned above observations from the simulations showing that stable synchronization was not possible with the STDP curve of the form given by Eq. (2.8). However, condition (b) indicates that synapses with such an STDP curve may mediate stable synchronization of type II neurons (for which $F(\tau)$ takes on both positive and negative values). Moreover, as it was shown with abstract models [45] and confirmed through our own research with biologically realistic models STDP leads to the learning of *in-phase* synchronization in networks of type II neurons.

As is discussed in the next chapter, the data from which the STDP curve has to be derived is very noisy [8, 11, 106, 27]. There is no unique way of doing so and other shapes of the curve were proposed along with (2.8). Biophysical models of STDP predict that the curve should be continuous [1, 103, 46], *e.g.*, of the following form:

$$\Delta g(t) = G(\Delta t) = A\Delta t \exp(-\gamma|\Delta t|). \quad (2.25)$$

As it will be shown in the following chapter, introduction of such a curve allows one to solve the problem of instability that was just described.

Finally, in somewhat general terms, I would like to emphasize the difference between the regimes of synchronization that are mediated by couplings with constant and activity-dependent strength. While absent in the case of constant coupling, presence of the second fixed point (2.14b) in the case of activity-dependent coupling introduces a new limitation on the relationship between the phases of two oscillators. It is this limitation that causes the suppression of phase slips under the influence of noise. Since this fixed point is stable, in the course of noise-affected synchronization the strength of activity-dependent coupling adjusts dynamically to keep this phase relationship close to satisfaction and, hence, suppresses phase slips. This, it turn, leads to the improved robustness of the synchronized state.

2.4 Discussion

In this chapter the effects of activity-dependent coupling on synchronization properties of coupled type I neurons was analyzed. It was shown that such coupling results in a substantial extension of the temporal synchronization zones, leads to more rapid synchronization and makes it much more robust against noise. The enlargement of synchronization zones means that with STDP-like learning rules the number of synchronized neurons in a large heterogeneous population must increase. In fact, this is an aspect of the popular idea due to Hebb [36]. It is supported by the results in [67, 28] which indicate that the coherence of fast EEG activity in the gamma band increases in a process of associative learning.

Based on the results from the discrete map model, it can be argued that the particular details of the signal-generating devices (e.g., neurons) and their connections (e.g., synapses) are not essential and the obtained results have general applicability. In fact, similar phenomena of robust and enhanced synchronization were observed in computer simulations of other types of periodic generators (such as Van-der-Pol and θ -oscillators) with STDP-like activity-dependent coupling.

Chapter 3

Plasticity-mediated enhancement of synchronization in a hybrid neural circuit

3.1 Introduction

The synchronization of oscillatory neural activity is a general mechanism underlying transient functional coupling of neurons, the formation of neural ensembles and large-scale neural integration [53, 25, 99]. Two recent examples illustrate this: Simultaneous recordings in the primary motor cortex of monkeys during task performance demonstrate accurate spike synchronization [79]. Fell *et al.* [28] showed that human memory formation is accompanied by rhinal-hippocampal gamma synchronization followed by a later desynchronization. The observed synchronization becomes more effective and robust as a result of learning (see, for example, [101]).

These observations lead to the key questions:

- What are the mechanisms that synchronize neurons with different intrinsic dynamics and frequencies?
- Why is neural synchronization so robust against noise?
- Which synaptic features and which features of the postsynaptic neuron are really important for stable synchronization (or entrainment) with fixed phase shift?

To answer these questions it is necessary to consider both the cooperative dynamics of large neural ensembles with diverse interconnections and the primary mechanisms of synchronization in minimal neural circuits. In this paper we investigate the second issue preparatory to the large-scale computations required for the first.

The mathematical description of neural synchronization or entrainment has a long history but starting in the late eighties to the present the role of synaptic dynamics and in particular synaptic plasticity in neural synchronization has increasingly attracted the attention of neuroscientists [22, 26, 96, 16, 60, 54, 91, 45]. Another recent development is the characterization of spike-timing-dependent plasticity (STDP) [11, 12, 1, 61]. In this type of plasticity, a synapse is depressed *or* potentiated according to the *timing* of pre- and postsynaptic spikes. This led us to the hypothesis that STDP might allow a synapse to adjust to an optimal strength for synchronization.

Our previous modeling with the type of STDP found in the mormyrid electrosensory lobe [9] has shown [110] that STDP allows synchronization over a much wider range of frequency mismatches and makes it much more robust to noise. These results encouraged us to explore the role of the more common and substantially different type of STDP found, e.g., in rat hippocampus [11, 61]. In an independent investigation Karbowski and Ermentrout (2002) showed within the framework of phase oscillators that this type of STDP allows stable and robust synchronization both in minimal circuits and in large heterogeneous networks. In the present work, we analyze the stability and robustness of synchronization in a hybrid neural network (spike generator - dynamic clamp (STDP synapse) - living neuron). In parallel numerical experiments we simulated two Hodgkin-Huxley type model neurons connected by an excitatory STDP synapse. Using both the hybrid circuit and a fully computational model we were able to explore the role in synchronization of various properties of the STDP synapse, and of the postsynaptic neuron, separately. Full control of the synapse allowed us to probe the role of the specific learning mechanism, whereas the computational model allowed us to test the influence of the properties of the postsynaptic neuron. The hybrid experiment and the model system demonstrate robust fixed phase entrainment through a STDP synapse.

3.2 Materials and methods

The experiments were carried out on *Aplysia californica* [44] weighing approximately 50-75 g supplied by the Aplysia Resource Facility, University of Miami, Florida. The animals were kept in a small artificial seawater tank at a temperature of 12°C.

3.2.1 Preparation

The animals were anesthetized with a high concentration Mg^{2+} solution injected into the body cavity of the animal at several points. The animal was then opened on the ventral side and the abdominal ganglion was taken out and pinned to a Sylgard coated Petri dish. The ganglion was de-sheathed in the dish on the dorsal side with fine forceps after 5 min application of a few crystals of protease (Type XIV, Sigma), washing and 30 min rest in a hypertonic Mg^{2+} solution.

The experiments were conducted in a high Mg^{2+} , low Ca^{2+} saline (330 mM NaCl, 10 mM KCl, 90 mM $MgCl_2$, 20 mM $MgSO_4$, 2 mM $CaCl_2$ and 10 mM Hepes) which blocks synaptic interaction such that the neurons are effectively isolated.

3.2.2 Experimental setup

Two sharp glass electrodes filled with 3M KCl with ca. 10 MΩ resistance were inserted into one tonic spiking neuron on the left side (dorsal side up) of the abdominal ganglion, typically the identified cells L7 or L8. These electrodes were connected to intracellular amplifiers (A-M Systems). One of the electrodes was used to pass the current calculated by a dynamic clamp program and converted by a Digidata 1200 D/A converter (Axon, CA) into the neuron. The other electrode was used to record the membrane potential via an A/D converter (PCI-MIO-16E-4, National Instruments) and the DasyLab (DATALOG - A National Instruments Company) data acquisition software.

The combined spike generator and dynamic clamp software with plastic synapses was developed from a simpler version developed by R. D. Pinto [72] after the original

ideas of Sharp [83, 84]. It was interfaced with Digidata 1200 board and was run on a Pentium III, 450 MHz system using Microsoft Windows NT 4.0. The presynaptic neuron was simulated by the dynamic clamp software as a simple spike generator with a given generic spike form. The calculated membrane potential of the presynaptic neuron was converted with the Digidata 1200 board as well and recorded on the data acquisition computer simultaneously with the membrane potential of the postsynaptic biological neuron and the injected synaptic current. The setup is summarized in Figure 3.1.

3.2.3 Spike generator and synapse model

The combined spike generator and dynamic clamp software generates the presynaptic membrane potential and the synaptic current. The presynaptic membrane potential V_1 is calculated from a list of predetermined spike times t_i .

$$V_1(t) = \sum_i V_s((t - t_i)/\tau_s). \quad (3.1)$$

The sum is taken over all spike times t_i before the present time t . The spike width used in the experiments was $\tau_s = 0.6 \text{ ms}$. The normalized spike potential $V_s(t)$ for a spike with maximum at $t_i = 0$ is given by

$$V_s(t) = V_{\text{spike}} \frac{x_a(t) + x_b(t)}{x_{\text{norm}}} + V_{\text{rest}} \quad (3.2)$$

$$x_a(t) = \frac{1}{2}(\tanh(2(t_0 - t)) + 1) \exp((t - t_0)/4) \quad (3.3)$$

$$x_b(t) = 2(\tanh(2(t - t_0)) + 1) \exp((t_0 - t)/4). \quad (3.4)$$

The variables $x_a(t)$ and $x_b(t)$ model the rising and falling flank of the spike. The parameter $t_0 = -0.576 \text{ ms}$ was chosen such that the maximum of the potential $V_s(t)$ occurs exactly at $t = 0$ and $x_{\text{norm}} = 3.25394$ guarantees that the maximum of $V_s(t)$ is V_{spike} . In the experiments this spike amplitude was chosen to be $V_{\text{spike}} = 60 \text{ mV}$ and the resting potential was $V_{\text{rest}} = -40 \text{ mV}$. These are typical values observed

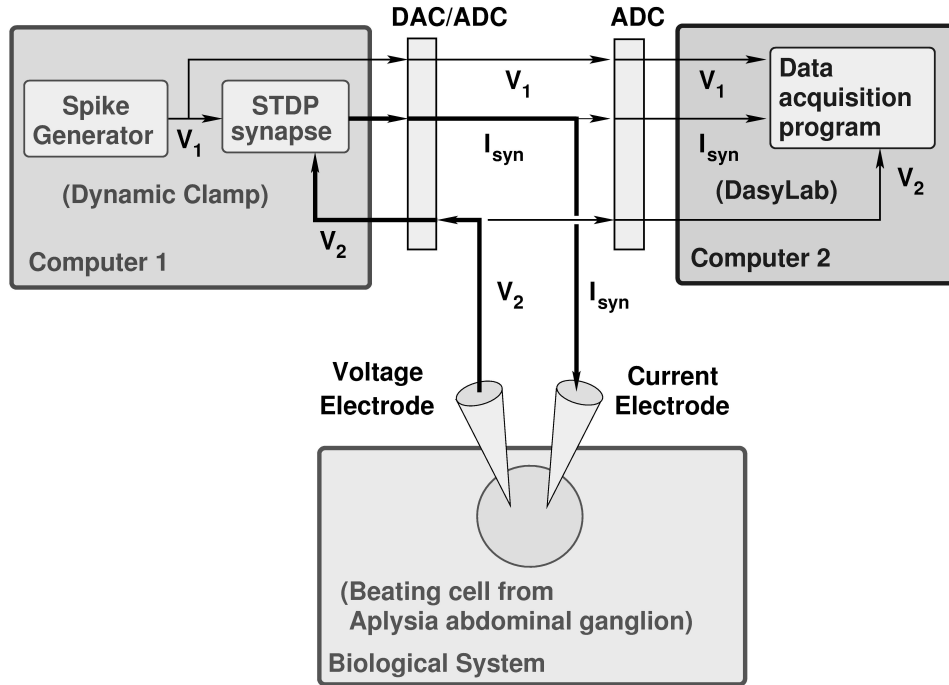


Figure 3.1: Experimental setup for the hybrid circuit of a simulated presynaptic neuron, a simulated synapse and a postsynaptic biological neuron from the *Aplysia* abdominal ganglion. The presynaptic neuron is a spike generator eliciting spikes of predetermined form at predetermined times which are read from a file. The synapse is simulated by the same software. The calculated synaptic current is injected into the postsynaptic neuron by means of a D/A converter (Digidata 1200, Axon, CA) and intracellular amplifier (A-M systems). The postsynaptic membrane potential is made available to the combined spike generator/ dynamic clamp software in the reverse direction. All relevant variables, the pre- and postsynaptic potentials and the injected synaptic current, are recorded by a separate data acquisition computer using DasyLab 5.6 (DATALOG - A National Instruments Company). Note that the calculated synaptic current as well as the plastic synapse conductance depend on both the pre- and postsynaptic voltages. Through the dependencies on the postsynaptic membrane potential, an effective feedback loop is formed between the synapse and the postsynaptic neuron. This feedback allows the STDP synapse to adjust to the intrinsic properties of the postsynaptic neuron

in molluscan preparations (compare to the data from the *Aplysia* neuron shown in figure 3.2).

The synaptic current is a function of the presynaptic and postsynaptic potentials of the spike generator, $V_1(t)$, and the biological neuron, $V_2(t)$, respectively. It is calculated according to the following model. The synaptic current depends linearly

on the difference between the postsynaptic potential V_2 and its reversal potential V_{rev} , on an activation variable $S(t)$, and its maximal conductance $g(t)$,

$$I_{\text{syn}}(t) = g(t)S(t) (V_2(t) - V_{\text{rev}}). \quad (3.5)$$

The activation variable $S(t)$ is a non-linear function of the presynaptic membrane potential V_1 and has an intrinsic activation timescale τ_{syn} ,

$$\frac{dS(t)}{dt} = \frac{S_{\infty}(V_1(t)) - S(t)}{\tau_{\text{syn}}(1 - S_{\infty}(V_1(t)))}, \quad (3.6)$$

where $S_{\infty}(V)$ is a sigmoid function, in particular

$$S_{\infty}(V) = \begin{cases} \tanh((V - V_{\text{th}})/V_{\text{slope}}) & \text{for } V > V_{\text{th}} \\ 0 & \text{otherwise} \end{cases}. \quad (3.7)$$

The reversal potential was chosen to be $V_{\text{rev}} = 20 \text{ mV}$, the threshold potential $V_{\text{th}} = -20 \text{ mV}$, the inverse slope of the sigmoid function $V_{\text{slope}} = 10 \text{ mV}$ and the synaptic timescale $\tau_{\text{syn}} = 25 \text{ ms}$ or sometimes $\tau_{\text{syn}} = 40 \text{ ms}$. The maximal conductance $g(t)$ is determined by the learning rule discussed below. The synaptic current is updated at about 5-10 KHz depending on how fast the computer is able to evaluate the equations. Figure 3.2 shows a typical example for the resulting spike forms and synaptic currents.

3.2.4 Learning rule

To determine the maximal synaptic conductance g of the simulated STDP synapse, an additive STDP learning rule with shift was used. To avoid run-away behavior (and resulting damage to the neuron) the additive rule was applied to an intermediate variable g_{raw} which then was filtered through a sigmoid function. In particular the

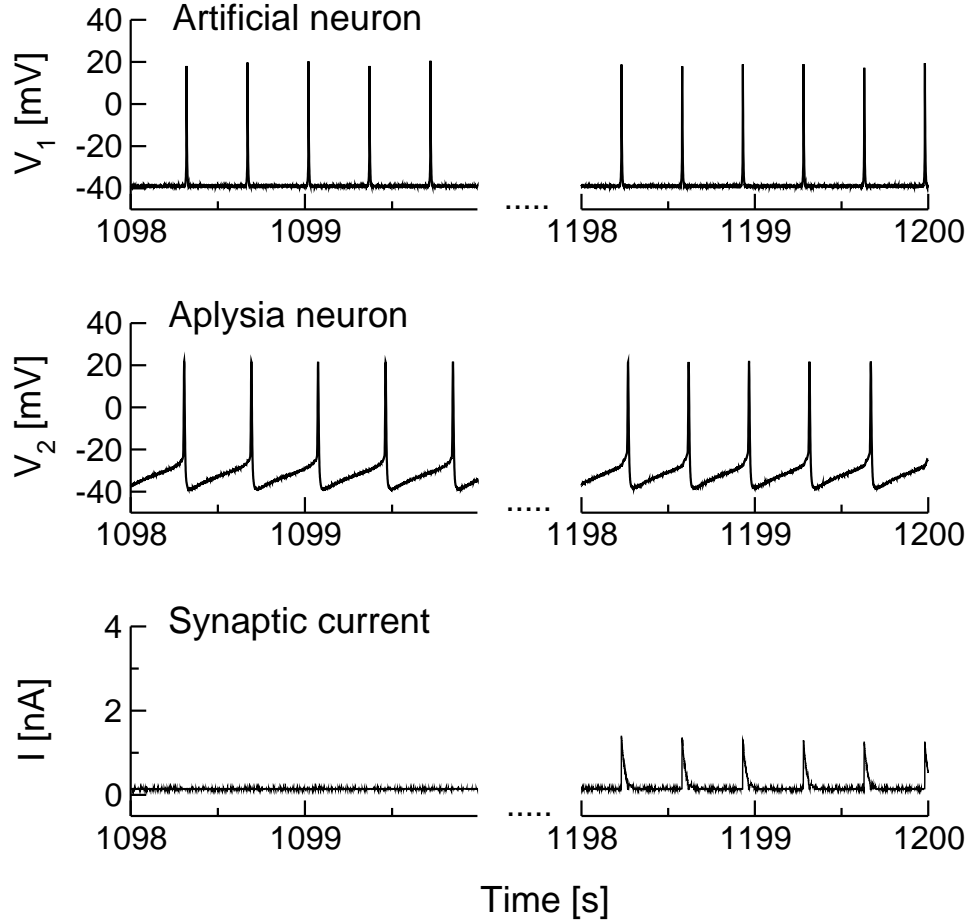


Figure 3.2: Episode of the uncoupled (left) and coupled (right) dynamics of the simulated and the biological neuron. The coupled dynamics are shown for a situation of stable 1:1 synchronization. The upper two panels show the membrane potentials of the simulated presynaptic and the biological postsynaptic cells, respectively. The lowest panel shows the synaptic current injected into the postsynaptic neuron. Note the pre- and postsynaptic spike forms and the typical EPSCs in the synaptic current. The synaptic strength in this example is comparably weak and clearly stabilized below the allowed maximum g_{\max} .

change Δg_{raw} in (raw) synaptic strength is given by

$$\Delta g_{\text{raw}} = \begin{cases} A_+ \frac{\Delta t - \tau_0}{\tau_+} e^{-(\Delta t - \tau_0)/\tau_+} & \text{for } \Delta t > \tau_0 \\ A_- \frac{\Delta t - \tau_0}{\tau_-} e^{(\Delta t - \tau_0)/\tau_-} & \text{for } \Delta t < \tau_0 \end{cases}, \quad (3.8)$$

where $\Delta t = t_{\text{post}} - t_{\text{pre}}$ is the difference in post- and presynaptic spike times. The parameters τ_+ and τ_- determine the width of the learning windows for potentiation

#	τ_{syn}	g_0	A_+	A_-	τ_+	τ_-	τ_0	g_{max}	g_{static}
1	20 ms	10 nS	8 nS	4 nS	80 ms	120 ms	30 ms	100 nS	50 nS
2	25 ms	15 nS	8 nS	4 nS	60 ms	90 ms	30 ms	150 nS	75 nS
3	25 ms	15 nS	8 nS	4 nS	80 ms	120 ms	30 ms	150 nS	75 nS
4 & 5	40 ms	15 nS	10 nS	6 nS	100 ms	200 ms	30 ms	50 nS	25 nS

Table 3.1: Parameters for the learning and static synapse.

and depression respectively and the amplitudes A_+ and A_- determine the magnitude of synaptic change per spike pair. The shift τ_0 reflects the finite time of information transport through the synapse. The left panel of Figure 3.3 shows the learning curve for the raw synaptic strength prescribed by equation (3.8) for a typical set of parameters.

The raw synaptic strength is then filtered according to

$$g = \frac{g_{\text{max}}}{2} \left(\tanh \left(\frac{g_{\text{raw}} - g_{\text{mid}}}{g_{\text{slope}}} \right) + 1 \right). \quad (3.9)$$

The maximally allowed value g_{max} for $g(t)$ varies in the individual experiments whereas $g_{\text{mid}} = \frac{1}{2}g_{\text{max}}$ and $g_{\text{slope}} = g_{\text{mid}}$ were used in all the experiments. By this filtering mechanism it is guaranteed that the maximal conductance $g(t)$ will always have values between 0 nS and g_{max} . It turns out that the raw synaptic strength $g_{\text{raw}}(t)$ is already bounded by the dynamics, if the neurons are synchronized, such that this mechanism often is not necessary. For frequency ratios in which entrainment did not occur, however, the bound imposed on $g(t)$ is important to avoid unrealistically high synaptic conductances and possible damage to the postsynaptic neuron. The shape of the filtering function (3.9) is shown in the right panel of Figure 3.3. Note that in the vicinity of g_{mid} the filtering function is close to the identity function, such that it has no serious impact on g and changes in g in this range, i.e., $g \approx g_{\text{raw}}$ and $\Delta g \approx \Delta g_{\text{raw}}$ in the vicinity of $g \approx g_{\text{mid}}$. This type of bounding mechanism was chosen over a threshold filter to avoid artifacts arising from positive STDP changes that reach such a threshold and are suppressed followed by negative changes that are not suppressed thereby destroying the balance between potentiation and depression.

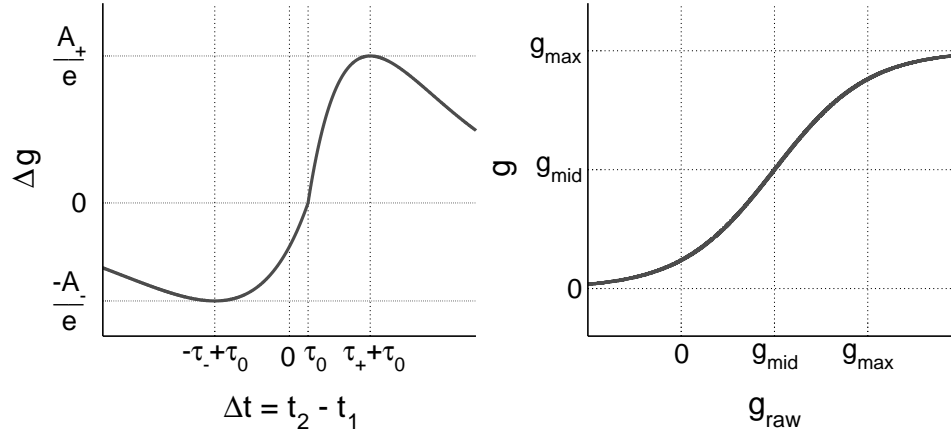


Figure 3.3: STDP learning curve (left panel) and filtering curve (right panel). The synaptic conductance $g(t)$ is enhanced if a postsynaptic spike occurs sufficiently long after a presynaptic spike, i.e., Δt is greater than the shift parameter τ_0 . Otherwise the synaptic strength is depressed. Note that the maximal changes in synaptic conductance occur at $\tau_- + \tau_0$ for depression and $\tau_+ + \tau_0$ for potentiation. The maximally possible changes are A_-/e and A_+/e . The specific parameters used in the experiments are given in the methods section. Usually $\tau_- = 1.5\tau_+$ and $A_+ = 1.5A_-$ were used as shown in the figure. The filtering is used to prevent damage to the postsynaptic neuron if synchronization is not achieved and the synaptic strength could grow without bounds. The filter curve shown in the right panel was generated with the typically used values g_{max} , $g_{\text{mid}} = 1/2 g_{\text{max}}$ and $g_{\text{slope}} = g_{\text{mid}}$. For details of the parameters used in the experiments see Table 3.1.

Synaptic changes occur whenever a pre- or postsynaptic spike is elicited. The dynamic clamp program continuously detects spikes and memorizes the most recent spike time of each pre- and postsynaptic neuron. For each new spike in either of the neurons, the synaptic strength is adjusted according to equations (3.8) and (3.9), immediately taking effect in the next time step of the calculation.

Our implementation of the STDP rule assumes that the experimentally observed rules for isolated spike pairs can be linearly superimposed. Recent results on spike-timing-dependent plasticity induced by triplets or quadruplets of spikes [29, 13] indicate that a simple superposition of the spike pair based rule might not always be appropriate. In numerical simulations we therefore also tested a non-linear superposition scheme based on the suppression model in [29]. For more complex spike patterns with very short inter-spike intervals and therefore a high degree of non-linear inter-

actions between multiple spikes, a dynamical model of STDP like the one suggested in [1] might be necessary.

3.2.5 Experimental protocol

For each presynaptic frequency the artificial neuron and the biological neuron were coupled and their membrane potentials as well as the synaptic currents were recorded for later analysis. In particular, we first took a 100 s recording of the uncoupled biological neuron and then coupled it to the presynaptic spike generator with an initial coupling strength g_0 (this parameter varies over different trials; see results below). The coupling with the plastic synapse was maintained for 100 s in most of the experiments. As the intrinsic frequencies of the tonic spiking neurons can vary with the individual preparation we sometimes also used a shorter coupling period of 50 s for intrinsically faster neurons. After another 100 s period of uncoupled recording, we repeated the coupling at a similar frequency but with static synapse strength g_{stat} . Again, we recorded the coupled neurons for 100 s (50 s). This procedure was repeated for a set of various presynaptic frequencies. Figure 3.4 shows an example of a recording from one of the STDP coupling sessions. Table 3.2 shows the two experimental protocols used for slow neurons (protocol A) and faster neurons (protocol B). To obtain a sufficient number of trials with different frequency ratios, a stable two-electrode recording had to be maintained for 2-3 hours. Not uncommonly, however, one of the micro-electrodes slipped or the neuron lost its spontaneous activity. In these cases reinserting the electrode or hyperpolarizing the neuron for a considerable time allowed us to continue the experiment, but it changed the properties of the neuron too much to allow a direct comparison between data collected before and after the adjustments. For analysis, we therefore only included data from ‘successful’ experiments, i.e., experiments in which a full sweep of the relevant frequencies was possible without interruption or loss of stationarity.

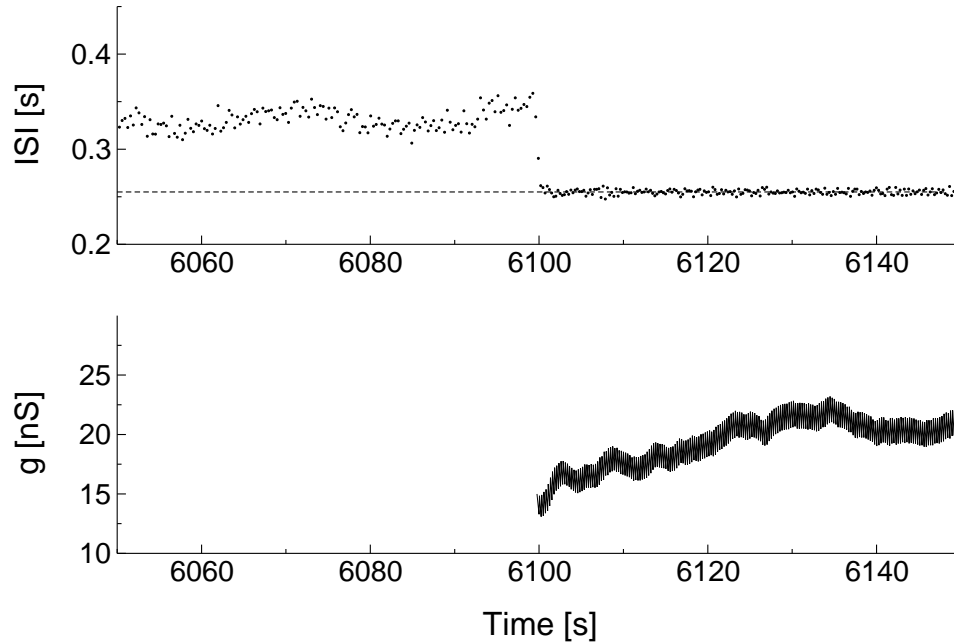


Figure 3.4: Example of a synchronization experiment. The upper panel shows the ISIs of the postsynaptic biological neuron and the lower panel the synapse strength g . Before coupling with the presynaptic spike generator the biological neuron spikes tonically at its intrinsic ISI of approx. 330 ms . Coupling was switched on with $g_0 = 15\text{ nS}$ at time $t = 6100\text{ s}$. As one can see the postsynaptic neuron quickly synchronizes to the presynaptic spike generator with ISI 255 ms (dashed line in the upper panel). The synaptic strength continuously adapts to the state of the postsynaptic neuron effectively counteracting adaptation and other modulations of the system. This leads to a very precise and robust synchronization at a non-zero phase lag. The precision of the synchronization manifests itself in the very small fluctuations of the postsynaptic ISIs in the synchronized state. Robustness and phase lag can not be seen directly in this figure.

3.2.6 Data analysis

To detect synchronization we first used a simple spike detection algorithm within the DasyLab data acquisition protocol to convert the membrane potential data into inter-spike interval data. Then we took the ratio of the average inter-spike intervals of the artificial and biological neuron during the 30 s before coupling and this ratio for the last 30 s of the coupled time and plotted these against each other. The choice of averaging over 30 s was guided by the trade-off between obtaining good statistics while, at the same time, not averaging over transient dynamics at the beginning of

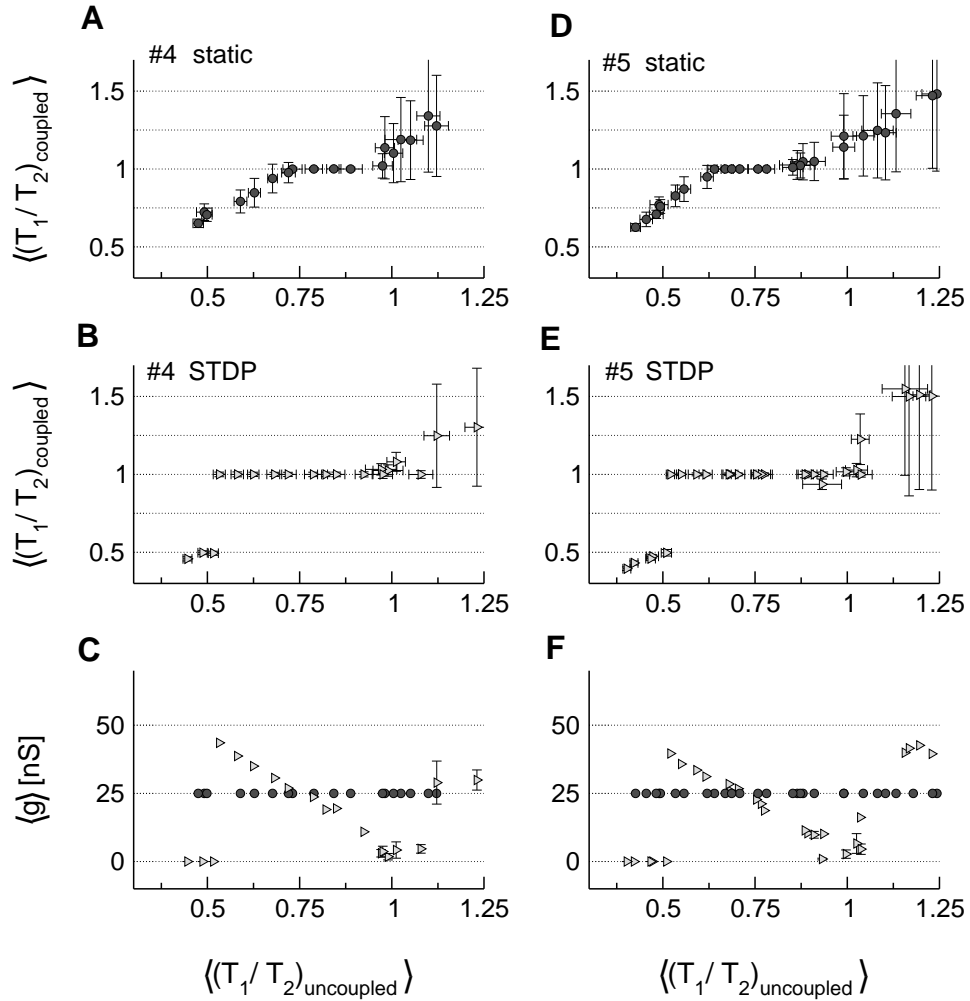


Figure 3.5: Two examples of synchronization windows. A, D show the ratios of coupled periods against the ratios of uncoupled periods for the static coupling and B, E display these data for the plastic synapse. Note the much larger synchronization windows and the very small error bars in the synchronized states in the experiments with the STDP synapse. The two experiments shown here correspond to numbers 4 and 5 in Figure 7. C, F show the average synaptic strength of the STDP synapse during the last 30 s of coupling (triangles) and the constant synaptic strength of the static synapse (circles).

the coupled phase. The coupled ratio as a function of the uncoupled ratio has a form typically obtained for coupled oscillators, cf. Figure 3.5. The plateaus in this function correspond to synchronized behavior at the last 30 s of the coupling phase. The vertical error bars in Figure 3.5 show the precision of the synchronization whereas the horizontal error bars show how constant the tonic spiking of the postsynaptic

A			B		
time [s]	coupling	T_1 [ms]	time [s]	coupling	T_1 [ms]
100-200	STDP	500	100-150	STDP	500
300-400	static	495	250-300	static	495
500-600	STDP	490	400-450	STDP	490
700-800	static	485	550-600	static	485

Table 3.2: Experimental protocol for the synchronization assessment experiment. The neurons were recorded when uncoupled, coupled with a STDP synapse, uncoupled again and then coupled with a static synapse. Then we started over with a different presynaptic period T_1 and so on. Note that it is not important to use exactly the same presynaptic periods for STDP and static coupling as the postsynaptic neuron varies its intrinsic frequency over time anyways. Most experiments were done with the protocol A of full 100 s coupling. Protocol B was used for intrinsically faster neurons to save experiment time and avoid damage to the preparation due to excessive forcing of the postsynaptic neuron.

neuron was before coupling. For large variations in ISIs of the uncoupled postsynaptic neuron, stable synchronization to the perfectly periodic artificial neuron cannot be expected.

3.2.7 Computational model

To analyze in greater detail how STDP influences the interaction between the pre- and postsynaptic neurons we simulated two Hodgkin-Huxley type model neurons coupled by an excitatory synapse with STDP. Each neuron was modeled using the standard formalism with sodium (I_{Na}), potassium (I_{K}) and leak (I_{leak}) currents:

$$C \frac{dV_i(t)}{dt} = -I_{\text{Na}}(t) - I_{\text{K}}(t) - I_{\text{leak}}(t) - I_{\text{syn}}(t) + I_{\text{stim}}, \quad (3.10)$$

where $i = 1, 2$ denotes the number of the pre- and postsynaptic neuron respectively, the leak current is given by $I_{\text{leak}}(t) = g_{\text{leak}}(V_i(t) - E_{\text{leak}})$, and $I_{\text{Na}}(t)$ and $I_{\text{K}}(t)$ were [94]

$$\begin{aligned} I_{\text{Na}}(t) &= g_{\text{Na}} m_i(t)^3 h_i(t) (V_i(t) - E_{\text{Na}}), \\ I_{\text{K}}(t) &= g_{\text{K}} n_i(t)^4 (V_i(t) - E_{\text{K}}). \end{aligned} \quad (3.11)$$

I_{stim} is a constant input current forcing each neuron to spike with a constant, I_{stim} -dependent frequency, and the second neuron was driven by the first via the excitatory synaptic current I_{syn} given by equation (3.5). Each of the activation and inactivation variables $y_i(t) = \{n_i(t), m_i(t), h_i(t)\}$ satisfied first-order kinetics

$$\frac{dy_i(t)}{dt} = \alpha_y(V_i(t))(1 - y_i(t)) - \beta_y(V_i(t))y_i(t). \quad (3.12)$$

The equations for the non-linear functions $\alpha_y(V)$ and $\beta_y(V)$ were

$$\begin{aligned} \alpha_n &= 0.032(-50 - V)/(\exp((-5 - V)/5) - 1), \\ \beta_n &= 0.5 \exp((-55 - V)/40), \\ \alpha_m &= 0.32(-52 - V)/(\exp((-52 - V)/4) - 1), \\ \beta_m &= 0.28(25 + V)/(\exp((25 + V)/5) - 1), \\ \alpha_h &= 0.128 \exp((-48 - V)/18), \\ \beta_h &= 4/(\exp((-25 - V)/5) + 1) \end{aligned} \quad (3.13)$$

and the parameter values were $C = 0.03 \mu F$, $g_L = 1 \mu S$, $E_L = -64 mV$, $g_{Na} = 360 \mu S$, $E_{Na} = 50 mV$, $g_K = 70 \mu S$, $E_K = -95 mV$, $\tau_{\text{Syn}} = 40 ms$.

The time dependent synaptic coupling strength $g(t)$ was determined by the spike timing of pre- and postsynaptic neurons. For each pair of nearest pre- and postsynaptic spikes, $g(t)$ changes by $\Delta g(t)$ which is a function of the time difference $\Delta t = t_{\text{post}} - t_{\text{pre}}$ between the spikes. In the first simulations we used the additive update rule already discussed (Figure 3.3 and equations (3.8) and (3.9)) with a linear superposition of synaptic weight changes. The following values of learning curve parameters were used in the simulations: $A_+ = 9 nS$, $A_- = 6 nS$, $\tau_+ = 100 ms$, $\tau_- = 200 ms$, $\tau_0 = 30 ms$. The initial synaptic conductance was taken to be $g_0 = 20 nS$. The parameters were chosen in a way that makes the model neurons to some extent similar to the *Aplysia* neurons used in the hybrid circuit experiments. Figure 3.6 shows a typical example of the dynamics of the membrane potentials (top) and the synaptic conductance (bottom). Note the onset of the synchronized state around $t = 4000 ms$,

manifested by the stabilization of the phase difference and of the synaptic strength. In a second set of simulations we repeated the investigation of synchronization with a non-linear superposition rule, adapted from the results of recent experiments with spike triplets and quadruplets [29, 13]. In this scheme the changes in synaptic strength depend on the history of previous spike times as well as the relative timing of spike pairs. In particular the simple rule of equation (3.8) is replaced by

$$\Delta g_{\text{raw}} = e_1 e_2 \begin{cases} A_+ \frac{\Delta t - \tau_0}{\tau_+} e^{-(\Delta t - \tau_0)/\tau_+} & \text{for } \Delta t > \tau_0 \\ A_- \frac{\Delta t - \tau_0}{\tau_-} e^{(\Delta t - \tau_0)/\tau_-} & \text{for } \Delta t < \tau_0 \end{cases}, \quad (3.14)$$

where the total efficacies e_1 and e_2 are products of efficacies due to all previous pairs of spikes:

$$e_k = \prod_{i=1}^{n-1} E_k(t_k^n - t_k^i), \quad (3.15)$$

where n is the number of the most recent spike of the neuron k and

$$E_k(x) = 1 - \exp(-x/\tau_k) \quad (3.16)$$

is the ‘efficacy function.’ The index $k = 1$ denotes the pre- and the index $k = 2$ the postsynaptic neuron. We used $\tau_1 = 200 \text{ ms}$, $\tau_2 = 500 \text{ ms}$ and the amplitudes $A_+ = 15 \text{ nS}$ and $A_- = 10 \text{ nS}$. All other parameters are chosen as for the linear superposition rule above. The idea behind this type of non-linear superposition of changes in g_{raw} is that the earlier spike pairs dominate and suppress contributions of later pairs. This suppression decays exponentially in time. The underlying assumption in generalizing this rule from spike triplets and quadruplets to continuous spike trains was that the suppression is combined by simple multiplication.

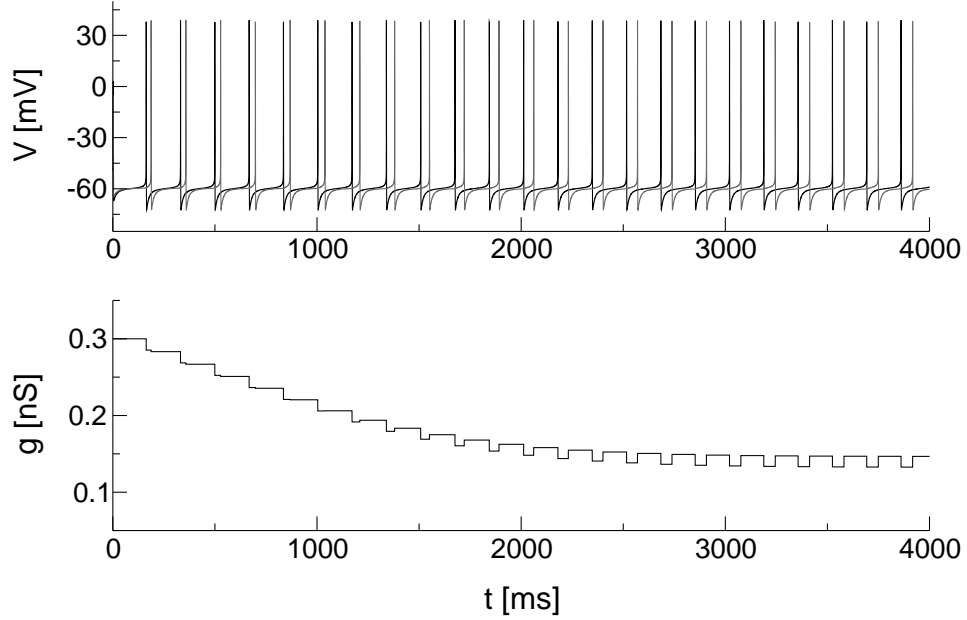


Figure 3.6: Example of a synchronization experiment in the computational model. The upper panel shows the membrane potential of the presynaptic HH neuron (black line) and of the postsynaptic HH neuron (gray line). The lower panel shows the synaptic conductance. The synchronized state is entered around 4000 *ms*. Note how the synaptic conductance stabilizes at a low value in the synchronized state and that there is a non-zero phase lag of about 90° in this example.

3.3 Results

3.3.1 Frequency synchronization in the hybrid circuit

To detect synchronization we plot the average ratio of the periods of the pre- and postsynaptic neuron during the last 30 *s* of coupling, $\langle (T_1/T_2)_{\text{coupled}} \rangle$, against the average ratio $\langle (T_1/T_2)_{\text{uncoupled}} \rangle$ during the last 30 *s* before coupling as explained in the data analysis subsection. $(T_2)_{\text{uncoupled}}$ is the starting period of the postsynaptic neuron. The period of the driving (presynaptic) neuron $(T_1)_{\text{uncoupled}} = (T_1)_{\text{coupled}}$ is unchanged when the neurons are coupled as the coupling is unidirectional. The period of the postsynaptic neuron is $(T_2)_{\text{coupled}}$ when it is driven by the presynaptic neuron. Figure 3.5 shows two examples.

To compare the quality and range of synchronization in all 5 successful experiments we calculate three characteristics:

- Synchronization window:

Synchronization of pre- and postsynaptic neurons occurs when $(T_1/T_2)_{\text{coupled}} = 1$. A postsynaptic neuron with a frequency mismatch $(T_1/T_2)_{\text{uncoupled}} \neq 1$ was more likely to be entrained by a plastic synapse than a static synapse, as shown by the greater number of points with $(T_1/T_2)_{\text{coupled}} = 1$ in Figure 3.5B and E. To assess the relative success of the static and the plastic synapses, we measured the size of the region in which $(T_1/T_2)_{\text{coupled}} = 1$. We define the *synchronization window* W as the largest contiguous set of $(T_1/T_2)_{\text{uncoupled}}$, for which $\sigma((T_1/T_2)_{\text{coupled}})_W = \langle (T_1/T_2)_{\text{coupled}} - \langle (T_1/T_2)_{\text{coupled}} \rangle_W \rangle_W$ is less than 0.01. The width of this set is denoted by $|W|$. Note that the data points $(T_1/T_2)_{\text{coupled}}$ are already averages over 30 s observation time each. We do not propagate the standard deviation of the time average to the average over data points because it is rather a measure of synchronization *quality* than of synchronization in principle. The quality of synchronization is discussed below. The results for the synchronization window size are shown in Figure 3.7 in the left panel. The synchronization windows for the plastic synapse are always larger than those for the static synapse.

- Precision of synchronization:

The average ratio $\langle \langle (T_1/T_2)_{\text{coupled}} \rangle_T \rangle_W$ over all points within the synchronization window should be exactly one for perfect synchronization. Figure 3.7, middle panel, shows this average ratio. Note that the values for the plastic synapse are much closer to 1 than the ones for the static case.

- Quality of synchronization:

The average standard deviation $\langle \sigma(T_1/T_2)_T \rangle_W$ shows how precisely the neurons were synchronized over the observed time of 30 s. The right panel in Figure 3.7 displays this quantity. The quality of synchronization is significantly higher for the STDP synapse.

The parameter values used during the experiments are summarized in Table 3.1. The strength of the static synapse was chosen to be of the order of the average station-

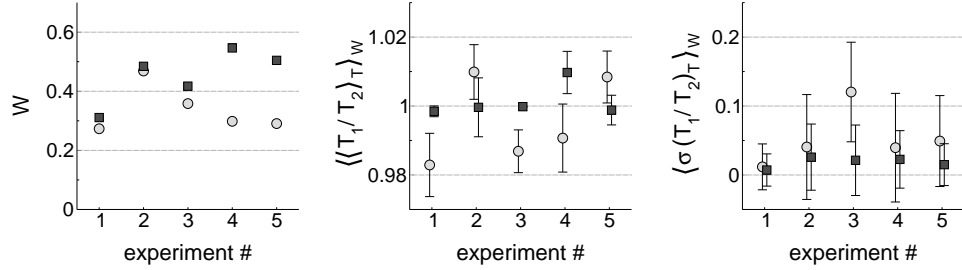


Figure 3.7: Three characteristics of the synchronization windows observed in 5 experiments. The left panel shows the width of the synchronization windows, W , the middle panel the averaged average ratio $\langle\langle T_1/T_2 \rangle_T\rangle_W$ within the synchronization window and the right panel the averaged standard deviation of the period ratios $\langle\sigma(T_1/T_2)\rangle_W$. The squares are the data obtained with a STDP synapse and the circles correspond to a static synapse. Note that synchronization windows are always larger and synchronization is always more precise and more robust for the STDP synapse than for the static synapse.

ary strength of the STDP synapse to allow a fair comparison. One might be tempted to argue that the synchronization window for the STDP synapse is larger because the static synapse is weaker than the maximally possible value of the STDP synapse. This is not true, as the numerical simulations show (see below). A stronger static synapse shifts the synchronization window toward smaller values of $(T_1/T_2)_{\text{uncoupled}}$, but does not enlarge it (see Figure 3.8). It would be desirable to demonstrate this effect in the hybrid circuit as well. Unfortunately it is not possible to keep *Aplysia* cells in a stable condition sufficiently long while driving them extremely hard. Therefore we cannot evaluate static synapses of a strength comparable to the maximal strength of the STDP synapse in the hybrid circuit experiments.

Note that the synaptic strengths for synchronized states, i.e., for points in the synchronization window, are typically weaker than the experimentally allowed maximum g_{max} . The synaptic strength is bounded by the dynamics alone. As the filtering function is close to unity for values of g close to g_{mid} , this statement also applies to the raw synaptic strength g_{raw} . For frequency ratios which the plastic synapse cannot synchronize, however, the raw synaptic strength typically either grows infinitely or goes to 0 resulting in g being close to g_{max} or 0 respectively, cf Figure 3.8E and J.

The relationship between the average strength of the STDP synapse within the

synchronization window and the presynaptic period T_1 , cf Figure 3.8E, J, can be easily explained. As the frequency mismatch between uncoupled pre- and postsynaptic frequency is larger on the left side of the synchronization window, the synapse needs to be stronger in order to entrain the postsynaptic neuron. On the right hand side of the synchronization window the frequencies are already very similar in the uncoupled state such that only a very weak synaptic connection is needed for synchronization. Overly strong forcing diminishes the synchrony, as the results for the strong static synapse show (see below).

3.3.2 Numerical results

We studied the synchronization properties of simulated neurons by setting the autonomous (uncoupled) period of the postsynaptic neuron to $T_2=300$ ms, then evaluating the average ratio of the periods in the coupled state $\langle(T_1/T_2)_{\text{coupled}}\rangle$ as a function of the period ratio before coupling $\langle(T_1/T_2)_{\text{uncoupled}}\rangle$. Figure 3.8 shows $\langle(T_1/T_2)_{\text{coupled}}\rangle$ as a function of $\langle(T_1/T_2)_{\text{uncoupled}}\rangle$ for the cases of synaptic coupling with constant strength $12.5 nS$ (A, F) and $25 nS$ (B, G), synaptic coupling with STDP using the linear superposition rule (C, H) and for the coupling with STDP using the non-linear superposition scheme (D, I). In the STDP cases the steady-state synaptic conductance $\langle g \rangle$ depends on the ratio of neuronal frequencies (C, F, triangles). Its average over all T_1/T_2 values is $\approx 13 nS$ for both STDP superposition schemes.

Figure 3.8A and B show the function associated with the 1:1 synchronization domain of a neuron driven by a static synapse. Contrary to naive expectation, the synchronization window is not substantially wider for a stronger synaptic connection; it merely moves further to the left. This is due to over-excitation by the overly strong synapse, on the right side of the synchronization window. Figure 3.8C and D show that the window of synchronization is *substantially widened* due to the plasticity of the STDP synapse. There does not seem to be a great difference between the two different superposition methods we used in the STDP rule: both mechanisms show the same widening of the synchronization window. Note that the steady-state conductance of

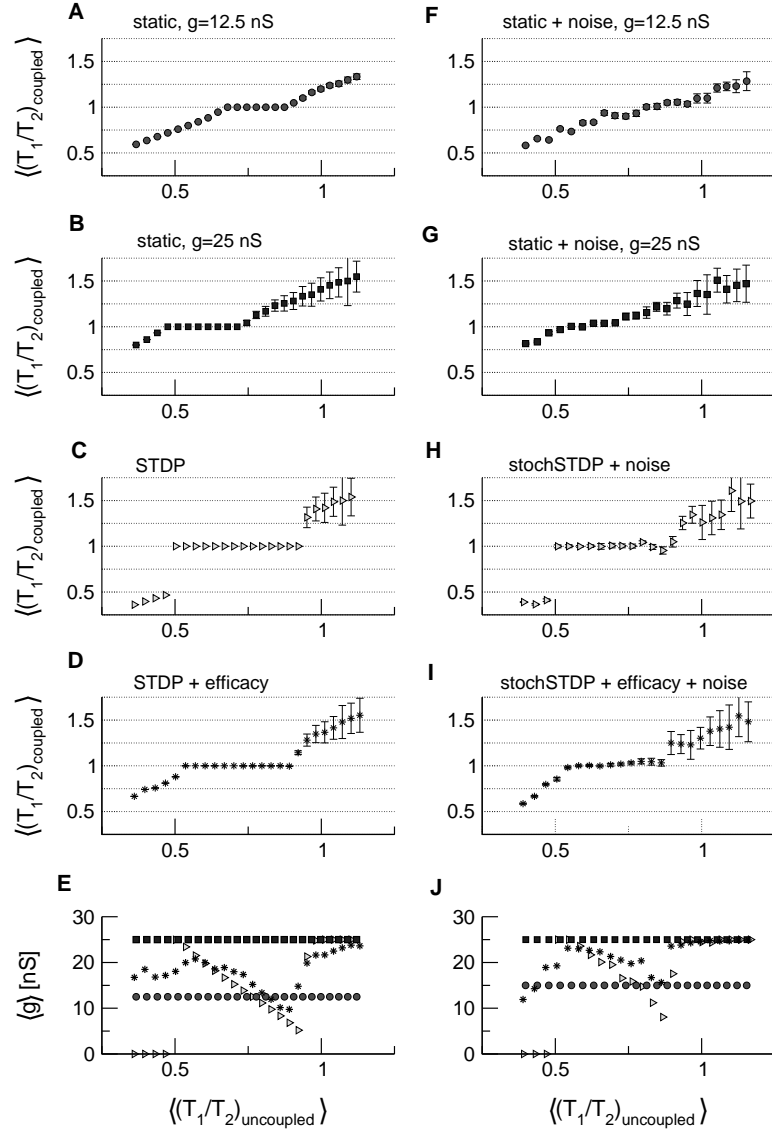


Figure 3.8: Numerical results. Synchronization window for 1:1 frequency synchronization of the simulated neurons for the cases of a static synapse (A, D) and (B, G) and of a STDP synapse (C, H) and (D, I). Linear superposition of synaptic changes was used in (C, H) and the non-linear suppression model in (D, I). Note that the results do not differ significantly. In (E, J) the average steady-state value of the synaptic strength g for the STDP synapses and the constant synaptic strength of the static synapses are displayed. The maximal synaptic strength of the STDP synapses was 25 nS in this study. The plots in the right column correspond to simulations with noise. Note the clear enlargement of the synchronization windows for both of the learning schemes and both in presence and absence of noise. The error bars in (A - D) and (F-I) indicate the standard deviation of the ratio $\langle (T_1/T_2)_{\text{coupled}} \rangle$. They show the precision of the frequency synchronization. There is a clear dependence of the equilibrium synaptic strength of the STDP synapse in the synchronization regime on the initial frequency mismatch.

the STDP synapse shown in Figure 3.8E depends on the mismatch of the presynaptic and postsynaptic frequencies and in most cases is less than its initial value of $20 nS$. These results indicate that a plastic synapse enhances neural synchronization by self-adjusting its conductance to the level that is appropriate for a given initial mismatch of the frequencies.

3.3.3 Robustness

We also studied the robustness of this enhanced synchronization in the presence of additive membrane noise and multiplicative synaptic noise. We simulated noise in the membrane potential of the postsynaptic neuron by adding Gaussian white noise to its membrane currents. Multiplicative synaptic noise was implemented by using the following stochastic update rule for the strength $g(t)$ of the STDP synapse. During each update $g(t)$ was changed by $\Delta g_{\text{stoch}} = (1 + R) \cdot \Delta g_{\text{raw}}$, where R is a uniformly distributed random number between -0.5 and 0.5 . In such a way we ensured that synaptic changes due to each event were stochastic, satisfying the learning curve depicted in Figure 3.3 only on average. This stochastic rule was again implemented both with linear superposition of changes Δg and the non-linear suppression model.

In the case of the static synapse we added noise with root mean square amplitude $\sigma = 3 nA$ (for comparison, peaks of the EPSCs were $0.75 nA$ in Figure 3.8F and $1.5 nA$ in Figure 3.8G) to the postsynaptic membrane and plotted the resulting staircases in Figure 3.8F and G. With the STDP synapse we used both membrane noise of the same strength and multiplicative synaptic noise as explained above. Note that the perturbations by additive noise on the membrane potential *and* the unreliable learning together should have more effect than the pure membrane noise applied to the static synapses. The results are shown in Figure 3.8H and I. The synchronization steps in the case of the static synapses are almost completely destroyed by noise, whereas the STDP-mediated synchronization is robust to both membrane noise and synaptic noise.

3.3.4 The mechanism

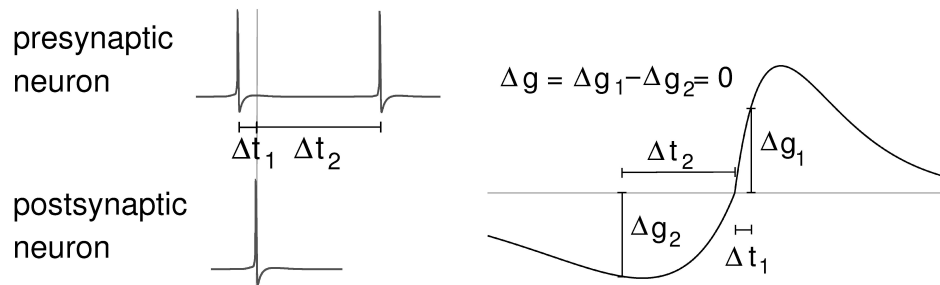
It is important to understand the mechanisms behind the enhancement of neural synchronization by a STDP synapse. The major factor is that the plastic synapse dynamically adjusts its conductance to a level that is well suited for synchronizing neurons with a given mismatch of intrinsic frequencies. This adjustment is an intrinsic property of the synaptic plasticity which can be understood by a simple stability argument.

A necessary condition for a stationary synchronized state is that the synaptic conductance is stationary as well. In the situation of two synchronized periodic spike trains with synchronization ratio 1 : 1 there are two types of contributions to changes in synaptic strength. One stems from the spike pairs comprised of a presynaptic spike followed by the next postsynaptic spike. The other is the change determined by the spike pair of the postsynaptic spike and the next presynaptic one (see Figure 3.9). The synaptic conductance is stationary if these contributions cancel each other such that the total change in synaptic strength after one period is 0.

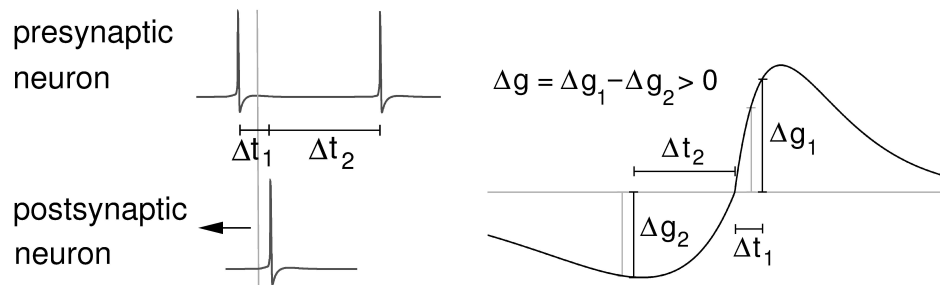
The corresponding time lags Δt_1 and Δt_2 , where $\Delta t_1 + \Delta t_2 = T_1 = T_2$, can easily be deduced directly from the learning curve, see Figure 3.9. To understand why this fixed point for the synaptic strength determines a stable synchronized state for the full system, consider the thought experiment illustrated in Figure 3.9B. Assume that the neurons are synchronized but the postsynaptic neuron's next spike is delayed, as it tries to break out of the synchronized state. This results in a net increase in synaptic strength driving the neuron back into synchronization. The other direction works in the same way. If the postsynaptic neuron advances its next spike, the net change in synaptic strength is negative; the neuron is less excited and goes back into the synchronized state (see Figure 3.9C). This analysis assumes a positive phase response curve for the postsynaptic neuron in the relevant phase regions. This condition is true for both the Aplysia neurons [44] used in experiments and the HH type model neurons used in the numerical work.

The time lag of the postsynaptic neuron with respect to the presynaptic neuron

A. No net change in conductance



B. Net increase in conductance



C. Net decrease in conductance

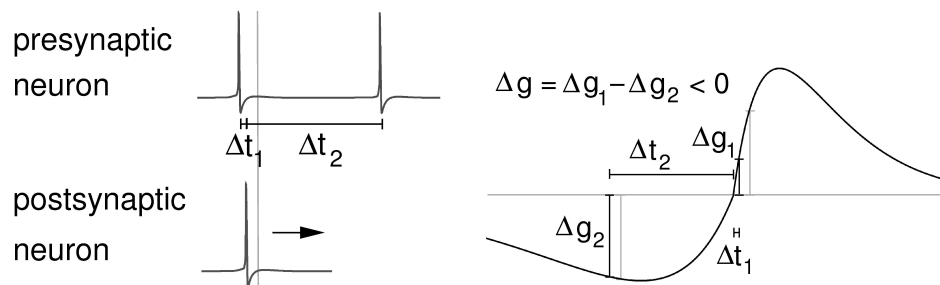


Figure 3.9: Mechanism of stable synchronization. Panel A shows the stable fixed point for the synaptic conductance for a period $T_1 = T_2 = \Delta t_1 + \Delta t_2$. The two contributions Δg_1 and Δg_2 cancel each other and the net change of synaptic strength is 0. If the postsynaptic neuron is too slow as shown in panel B, the synaptic changes do not cancel such that there is a net increase in synaptic strength and the postsynaptic neuron is driven stronger forcing it back into the synchronized state. On the other hand, if the postsynaptic neuron is too fast as depicted in panel C, the net change in synaptic strength is negative and the postsynaptic neuron is driven less strong bringing it back into synchronization as well.

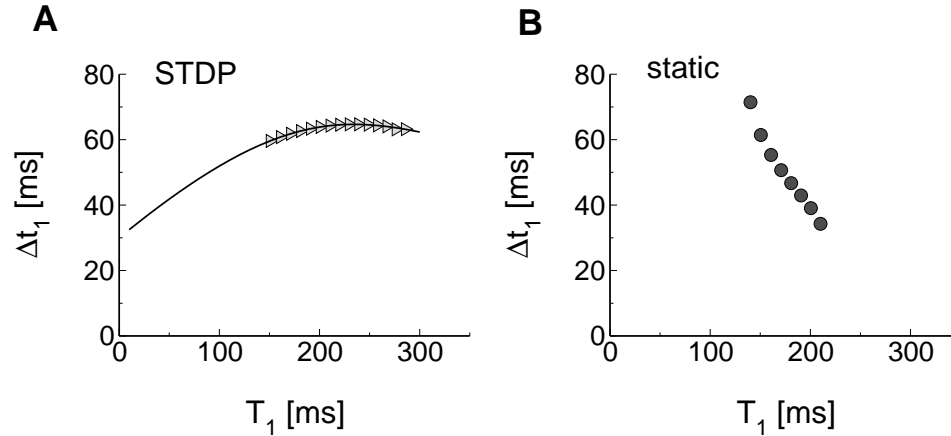


Figure 3.10: Time lags in the synchronized state. Panel A shows the spike time difference between each presynaptic and the next postsynaptic spike in the synchronized state. The solid line corresponds to the time difference predicted by the fixed point analysis of the learning rule. There is a perfect correspondence in the 1:1 synchronization region. The on average stronger forcing through the static synapse causes on average shorter time delays (right panel). The dependence of the average time delays on the presynaptic period T_1 in the case of the static synapse comes about because the mismatch of frequencies is higher on the left side than on the right side of the synchronization step. Therefore, stronger forcing would be needed to obtain the same small delays on the left side as on the right side which can not be provided by the synapse of constant strength.

resulting from the above analysis is shown as the solid line in panel A of Figure 3.10 in comparison to the observed lags in numerical simulations (triangles). The match between theory and simulation confirms the validity of our analysis; note that the simple HH type model used in the computational work was, apart from overall timescales, not specifically adjusted to match characteristics of the *Aplysia* neurons. This clearly shows that the particular spike form of the postsynaptic neuron does not play a major role for this type of synchronization. The effect of slow currents and adaptation in the postsynaptic neuron might merit further investigation, however.

3.4 Discussion

Spike-timing-dependent plasticity is a mechanism that enables synchronization of neurons with significantly different intrinsic frequencies. This is a quite unexpected

result from our experiments with hybrid circuits and from the computational analysis. These results have yet to be confirmed with real biological synapses that exhibit STDP such as synapses found between hippocampal cells in rats. We will address this question in further work.

Furthermore, STDP - mediated synchronization is a remarkably robust phenomenon. We showed that it is stable against strong noise in the membrane potentials and synaptic processes as well as against a wide variability of the membrane properties of the coupled neurons. This robustness is a result of the dynamic modifications of the synaptic conductance that allow the system to continuously adapt to an optimal state for synchronization. As shown above, the modifications in synaptic conductance arise as a result of the interplay between potentiation and depression. The form of the plasticity curve is such that the resulting synaptic changes keep the postsynaptic neuron stably entrained by the presynaptic neuron at all times. The details of the fast intrinsic dynamics of the postsynaptic neuron do not seem to play a major role in this mechanism. The main characteristics necessary for the successful synchronization are a positive phase response curve and stationary dynamics. Neurons with slow timescales due to slow currents or adaptation will need further analysis.

Another consequence of the interplay between potentiation and depression is a dynamic *stabilization* of the synaptic conductance. It has been shown by several groups that additive STDP learning rules, by themselves, lead to either an unbounded growth or an unbound decay of synaptic strength [89, 90, 97, 80, 47]. To achieve stability of the learning dynamics, multiplicative rules [81, 91], learning curves with a negative total integral [47] or, most commonly, artificial bounds on the strength of the synapse [89, 90, 97] have been used. In contrast to these approaches, we were able to show that the additive STDP learning rule of the type described here results in a *self-limitation* of synaptic strength that does not require artificial bounds or a negative integral of the learning curve. This is already a quite interesting result on its own.

The main functional role of STDP in neural systems is still not completely clear. In this work we investigated its importance for correlating rhythmic activity of neu-

rons. Because the details of the temporal dynamics of STDP synapses are not known we have used a phenomenological, instantaneous and deterministic model which is inspired by the experiments of [11, 61]. The changes of synaptic strength that depend on the pre- and postsynaptic spiking have been measured in such experiments by averaging over the action of many events that are well separated in time. As a result of such processing one might think that STDP is a slow process and characterized by a long transient time. On the contrary we think that because the results of individual events can be recognized even after long times (on the order of minutes) it seems evident that information about the timing of spikes needs to be kept in the synaptic dynamics immediately after the event (i.e., after tens of milliseconds). The averaged statistical results just tell us that not all single events are successful such that the average might change on a slower timescale only. Because in our experiment we are interested in the temporally local adaptivity of the synapse, and not in long-term plasticity, this is not important and the use of instantaneous STDP updates is justified.

The learning curve used in this work is slightly different from those used in most computational studies of STDP [89, 90, 97]. The curve typically used consists of two exponentials (on the left and on the right from $\Delta t = 0$) and is discontinuous at $\Delta t = 0$. We however used a curve which is continuous everywhere. While available experimental data [8, 11, 106, 27] are not conclusive as to which type is correct, we would like to argue that a continuous curve appears to be more reasonable from a biophysical point of view. In fact, recent biophysical models of STDP [1, 103, 46] predict a continuous learning curve and such curves have been used extensively in a number of phenomenological models [78, 47]. It turns out that this type of learning curve is also more suitable for the mechanism of stable neural synchronization investigated here.

In addition to being continuous the learning curve used in this study also was shifted to the right by a constant time shift τ_0 . The necessity for this time shift arose from the finite transmission time of the STDP synapse. Because of this finite transmission time the action of a presynaptic spike onto the postsynaptic activity is

delayed. As a result the postsynaptic neuron can not be driven with a zero phase lag. The learning rule therefore needs to allow a stable synchronized state with an appropriate non-zero phase lag. This was achieved through the shift τ_0 . We are not aware of hard experimental evidence for such a shift but as we are injecting currents and measuring potentials at the soma we would like to argue that the time shift in the learning curve merely reflects the back-propagation time of the postsynaptic action potential into the dendrite such that an unshifted learning curve applies at the synapse itself. Note that the shift is comparatively small, see Figure 3.3, and therefore hard to detect in noisy experimental data.

The comparison between a simple linear superposition of synaptic changes and the non-linear depression model adapted from [29, 13] showed no major differences for synchronization. For continuous periodic spike trains like those used in this study, the non-linear superposition model results mainly in a frequency-dependent depression of the plasticity. The balance between potentiation and depression, which is the important factor for the synchronization mechanism, is not very affected by this depression of plasticity. Therefore it is not unexpected that the impact of the non-linear superposition scheme on the synchronization results is not significant.

The synchronization observed in this work in both the experiments with a hybrid circuit and in computer simulations always occurs with non-zero time lag between pre- and postsynaptic spikes as mentioned above (see also Figure 10). This time lag is solely determined by the STDP learning curve as that time lag that produces no net change in synaptic conductance. It therefore is the same for both the experiments and the numerical work and does not depend on the details of the fast dynamics of the postsynaptic neuron. Its magnitude as compared to the period of oscillations is usually quite substantial; thus the synchronization discussed here is not to be confused with a zero-time lag frequency locking. It has, in different contexts, also been referred to as *entrainment* of the postsynaptic neuron by the presynaptic one.

Our results are in agreement with the earlier theoretical results on heterogeneous networks of phase oscillators mentioned in the introduction [45]. It is however worthwhile to note some differences in the details. Whereas synchronization in the sym-

metrically connected phase oscillator networks shows zero phase locking, we always observe a non-zero phase lag stemming from the finite timescale of the synapse dynamics and the unidirectional coupling. The other main difference is the automatic adjustment of synaptic coupling strength to a suitable value for any frequency mismatch. The coupling strength needed to some extent be adjusted by hand to the frequency mismatch in the earlier work [45].

While concentrating on a minimal neural circuit of two neurons in the present work, the results we have obtained have profound implications for larger networks of neurons as well. We expect that in the context of larger neuron groups we will be able to observe even more striking effects. We expect that only a few STDP synapses from a ‘command neuron’ might be enough to entrain large ensembles of quite heterogeneous and only weakly coupled neurons. Similar effects have already been observed in the aforementioned work on phase oscillator networks [45]. Our own preliminary numerical results also confirm this speculation. It may have implications for the binding problem and even might play a role in epilepsy. In the context of propagating waves in neural networks with STDP synapses such as so-called synfire chains [3] in the hippocampus we can predict that the non-zero time lag will determine the properties of the wave, especially its propagation speed.

Chapter 4

Entrainment of electrically coupled neural ensembles by STDP-mediated periodic inputs

4.1 Introduction

Synchronous neural activity plays an important role in the functioning of the brain. It is a robust phenomenon, frequently observed across populations of neurons with diverse membrane properties and intrinsic frequencies. In the light of such diversity it remains unclear how can precise synchronization be achieved in heterogeneous networks. Several mechanisms were suggested and many of them require unreasonably high degree of network homogeneity or very strong connectivity to achieve coherent neural activity. Recently, it was demonstrated in computer simulations and in experiments with hybrid neural circuits that in a network of two synaptically coupled neurons spike-timing-dependent plasticity of the synapse leads to the dynamic self-adaptation of synaptic conductance to the value that is optimal for the entrainment of the postsynaptic neuron [110, 69]. In this chapter we study the entrainment of a heterogeneous network of electrically coupled neurons by periodic external stimulation. Only a fraction of neurons in the network receive stimulation. We show by computer simulations that such network oscillates with much higher degree of coherence when it is subject to the stimulation that is mediated by STDP synapses as compared to the case of stimulation through non-plastic synapses. We also study how the observed

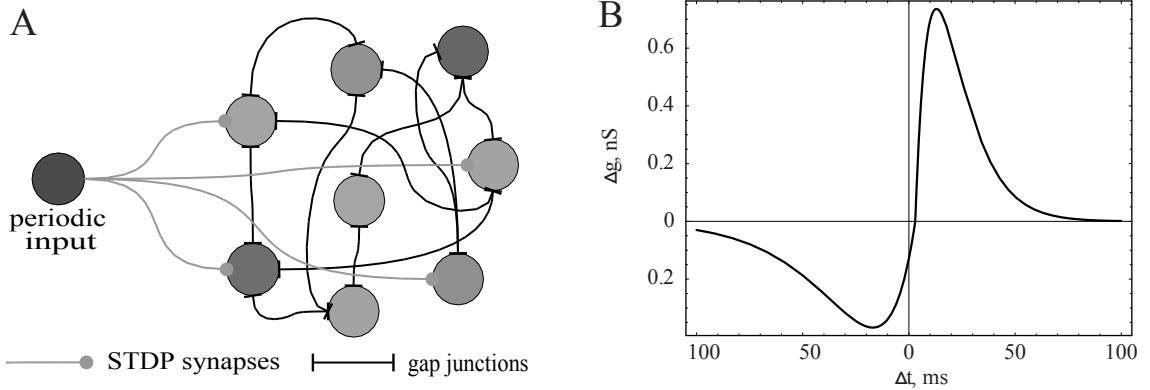


Figure 4.1: (A) Configuration of the model: heterogeneous network of tonically spiking pyramidal neurons stimulated by external periodic input through a set of STDP synapses. (B) The curve illustrating the learning rule used in simulations of STDP.

phenomenon is influenced by the number of stimulated neurons, strength of electrical coupling and the degree of heterogeneity.

4.2 Description of the model

Our computational model consists of 50 one-compartmental pyramidal neurons [94] randomly connected by 1750 gap junctions (Fig. 4.1(A)). The neurons are described by Eqs. (2.1)-(2.4) and currents through gap junctions follow Ohm's law:

$$I_{syn}^{gj}(t) = g_{gj}(t)(V_i(t) - V_j(t)). \quad (4.1)$$

Conductances of gap junctions are taken to be relatively small and chosen randomly from the interval $g_{gj} \pm 50\%$ with $g_{gj} = 0.1 nS$. Each neuron is spiking tonically with a period randomly chosen from the interval $T_2 \pm 30\%$ with $T_2 = 35 ms$. The network receives periodic input ($T_1 = 25 ms$) through a number of excitatory STDP synapses. Initial conductances of the input synapses are chosen at random from the interval $g_{in} \pm 50\%$ with $g_{in} = 2.5 nS$.

The time-dependent conductance of STDP synapses $g(t)$ is influenced by the spike timings of pre- and postsynaptic neurons. For each pair of nearest pre- and postsy-

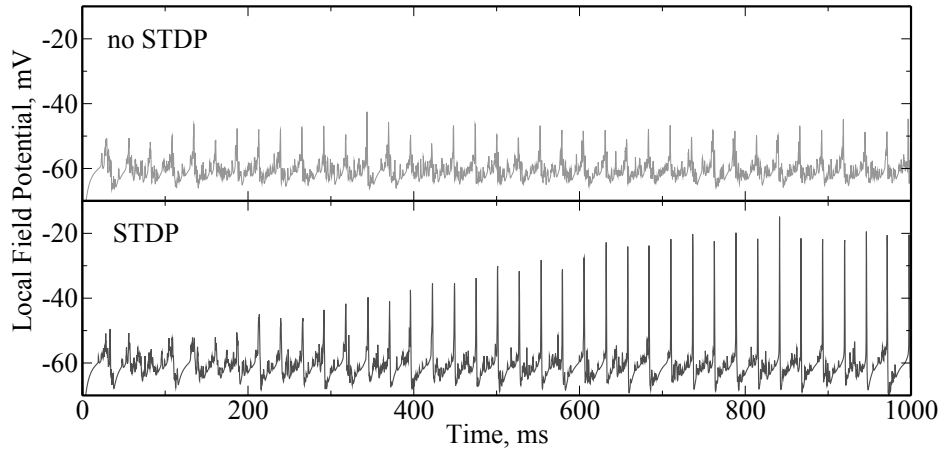


Figure 4.2: Time series of the local field potential in networks with constant (top) and STDP-mediated (bottom) inputs.

naptic spikes, $g(t)$ is changed by $\Delta g(t)$ which is a function of the time difference $\Delta t = t_{post} - t_{pre}$ between the spikes. We use additive update rule with a linear superposition of conductance changes and a small shift of the curve, τ_0 (Fig. 4.1(B)):

$$\Delta g = G(\Delta t) = \begin{cases} A_+ \frac{\Delta t - \tau_0}{\tau_+} e^{-(\Delta t - \tau_0)/\tau_+} & \text{for } \Delta t > \tau_0 \\ A_- \frac{\Delta t - \tau_0}{\tau_-} e^{(\Delta t - \tau_0)/\tau_-} & \text{for } \Delta t < \tau_0 \end{cases} \quad (4.2)$$

with the following values of parameters: $A_+ = 2 \text{ nS}$, $A_- = 1 \text{ nS}$, $\tau_+ = 10 \text{ ms}$, $\tau_- = 20 \text{ ms}$, $\tau_0 = 3 \text{ ms}$.

4.3 Results

We simulated dynamics in the described above network and evaluated the coherence of its oscillations by calculating an average membrane voltage which served as a proxy of the local field potential (LFP). As Fig. 4.2 illustrates, the amplitude of network oscillations remains constant throughout the response in the case of constant input conductances and exhibits growth and saturation at much higher values in the case of input synapses with STDP. The explanation for such behavior of LFP amplitudes

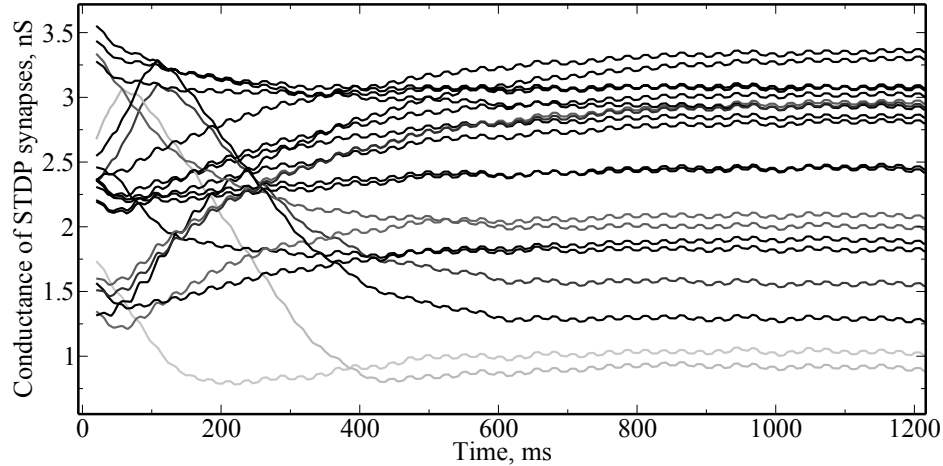


Figure 4.3: Dynamics of conductances of input synapses with STDP.

is evident from Fig. 4.3 where the dynamics of synaptic conductances in the case of STDP-mediated inputs is plotted. As one can see, these conductances change dynamically at the beginning of the response and in a relatively short time reach location-specific steady-state values. So, as it was shown in [110, 69] for the case of two neurons, at each site of the network input synapses provide forcing of the strength which is appropriate for synchronization of presynaptic and postsynaptic spike trains.

Let us investigate the role of different parameters of the model. In order to quantify the ability of STDP synapses to mediate an efficient entrainment of the postsynaptic network we compare the coherence of network oscillations (as measured by the amplitude of LFP) for the cases of constant and STDP-mediated inputs. First, let us see how the coherence of oscillations is influenced by the number of inputs. To account for the role of parameter heterogeneity we simulate 5 random networks for each data point. As one can see in Fig. 4.4, the coherence in STDP-stimulated networks growth much faster with the number of input synapses. Interestingly, the network without STDP shows a relatively low degree of coherence even when each neuron in the network is stimulated. This is because in this case conductances of input synapses do not depend on the differences of presynaptic and postsynaptic frequencies and hence provide inadequate forcing strengths.

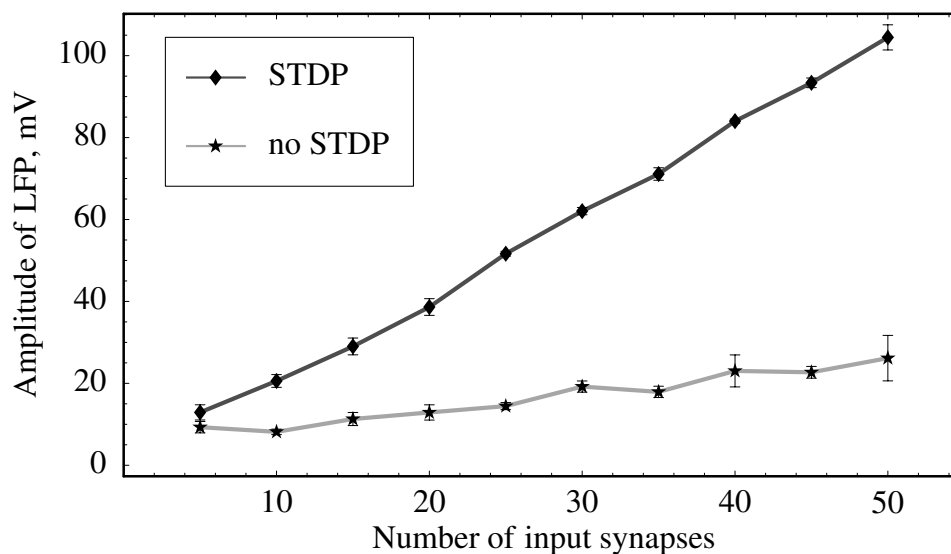


Figure 4.4: Dependence of the amplitude of network's local field potential on the number of input synapses.

Let us now look at the role of g_{gj} - average conductance of gap junctions. In Fig. 4.5 we plot the LFP amplitudes for different values of g_{gj} obtained in simulations of a network with 50 input synapses. Note that in the case of STDP-mediated stimulation the amplitude of LFP is almost independent of g_{gj} . The difference between the amplitudes is especially profound in weakly coupled networks in which gap junctions play almost no role in synchronization.

Finally, we investigate the role of network heterogeneity by simulating networks with 50 input synapses and varying the range of variability for the conductances of gap junctions, conductances of input synapses and spiking periods of the neurons. As Fig. 4.6 illustrates, coherent oscillations in STDP-stimulated networks are much more robust to the variability of network properties. They are robust because conductances of STDP synapses reach optimal for synchronization values regardless of the mismatch in neuronal properties.

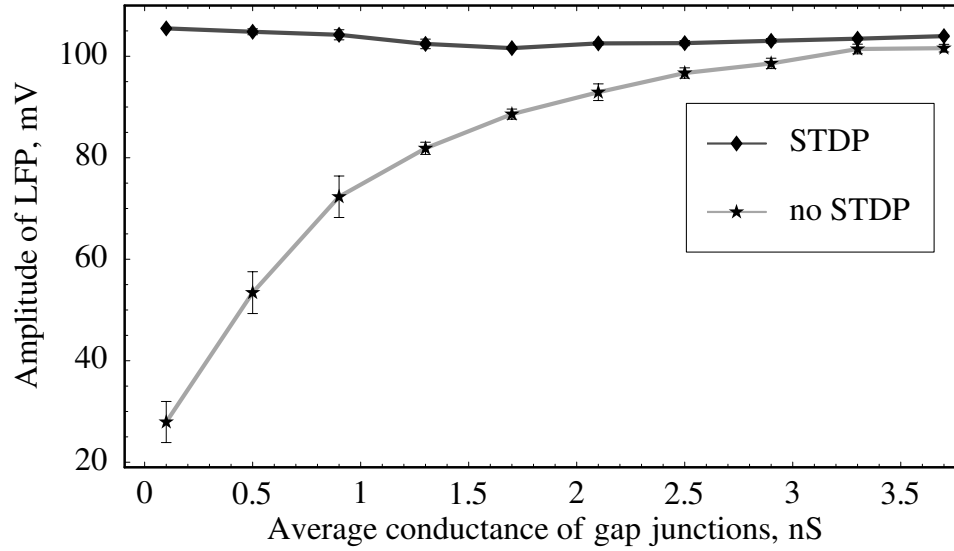


Figure 4.5: Dependence of the amplitude of network's local field potential on the average conductance of gap junctions.

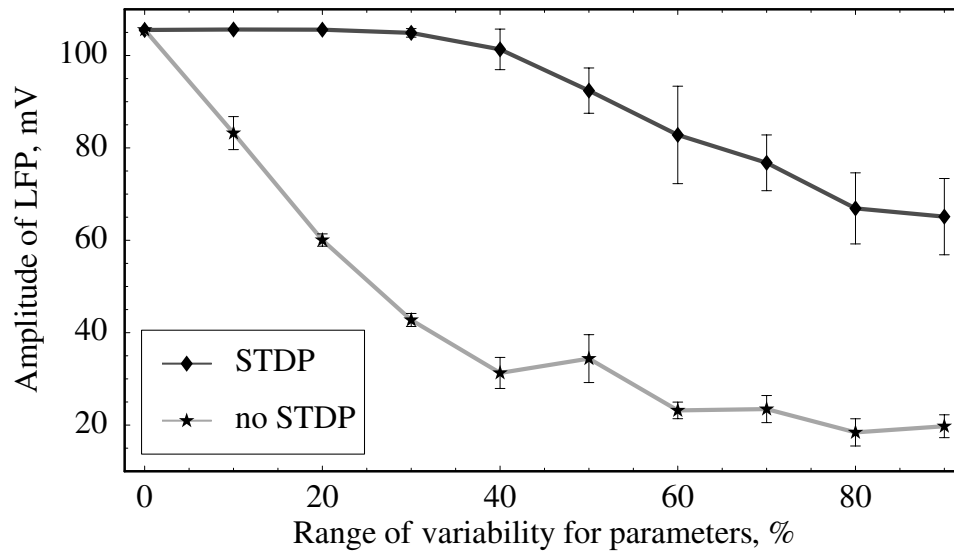


Figure 4.6: Dependence of the amplitude of network's local field potential on the variability of network parameters.

4.4 Discussion

As we have shown, due to the heterogeneity of the network, stimulations of different strengths are needed at different sites of the network in order to bring it into the synchronized state. We have demonstrated that STDP leads to such specificity of

stimulation by dynamically adjusting the strength of each synapse to the value that is optimal for entrainment. On the other hand, stimulation through static synapses is, in general, not site specific and can not provide adaptive levels of stimulation. As a result, coherence of network oscillations is much higher when it is stimulated by STDP synapses as compared to the case of stimulation by static synapses. The difference in coherence is maximal for weakly coupled networks. Also, as we have shown, coherent oscillations in STDP-stimulated network are much more robust to the variability of network properties.

Recent experiments with connexin36 knock out mice [17, 42] and modeling studies [95] suggest that electrical coupling between hippocampal pyramidal cells is responsible for the formation of synchronized gamma-band activity in hippocampus, with gap junctions between interneurons exerting modulatory effect only. Taking into account the fact that processes that synapse onto pyramidal cells exhibit STDP, we suggest that the described above mechanism may play a role in effective entrainment of the hippocampal network by the input from upstream areas of the brain.

Chapter 5

Regularization of chaos in neural circuits with plastic electrical synapses

5.1 Introduction

Traditional in neurophysiology intracellular recordings of membrane potentials have produced long, statistically stationary time series that unambiguously demonstrated presence of chaotic dynamics at the level of an individual cell. In particular, inferior olivary neurons [59], some pacemaker neurons [34] and neurons from central pattern generators [2] were found to be chaotic. Reconstructions of their phase portraits and analysis of bifurcations has indicated that neural chaos can be described by deterministic models with weak noise [2]. Functional role of the neural chaos is not absolutely clear. Reasonable hypothesis is the following: chaotic neural dynamics can be easily transformed into regular oscillations with wide range of frequencies due to the existence of saddle cycles with different periods in the strange attractor of the dynamics. Thus chaotic neural systems are potentially very flexible [74]. The regularization or control of neural chaos in cells with irregular dynamics can occur as a result of their coupling through chemical or electrical synapses [75, 24, 76, 50, 82, 18]. However, such regularization is neither robust nor adaptive. In this paper we suggest the use of electrical plastic synapses in order to improve the robustness of regularization and make its range much wider. Such synapses would be important for the creation of

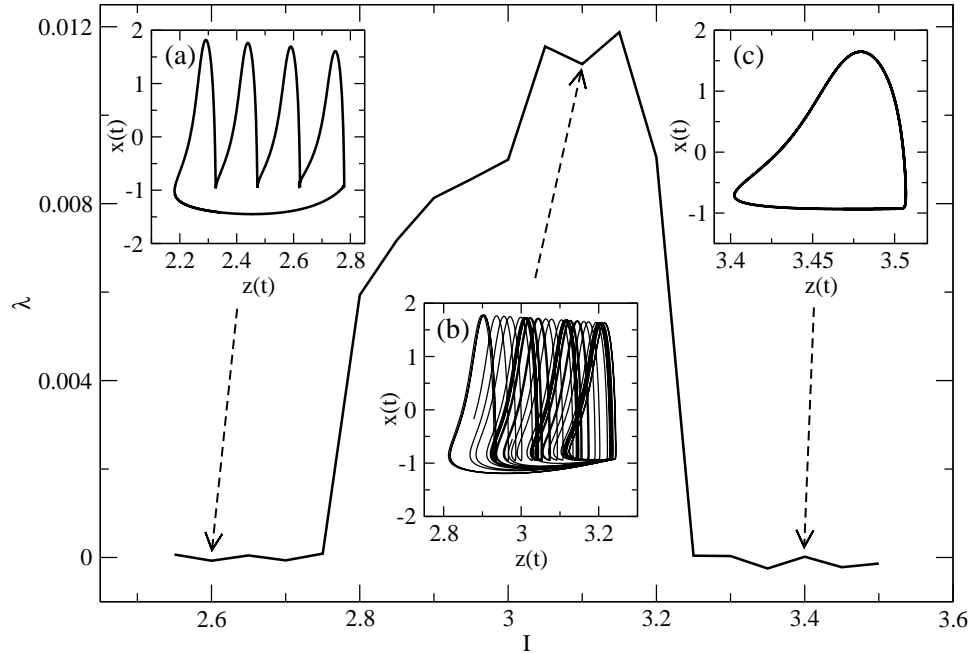


Figure 5.1: Largest Lyapunov exponent λ calculated for the stimulated Hindmarsh-Rose neuron as a function of stimulating current I . Dynamics of this model neuron is periodic for $I \lesssim 2.75$ (see insert (a) and Fig. 5.2(a)) and $I \gtrsim 3.25$ (see insert (c) and Fig. 5.2(c)), and is chaotic for $2.75 \lesssim I \lesssim 3.25$ (see insert(b) and Fig. 5.2(b)).

electronic neural networks and for the development of neural prosthetics.

The chapter is organized in the following way. We start by presenting the dynamical equations that describe chaotic spiking-bursting neurons, we then formulate the dynamical model of an electrical plastic synapse and after that we present the results of mathematical analysis and computer simulations of chaos regularization in the system. Finally, we compare our approach with the well known methods of chaos control.

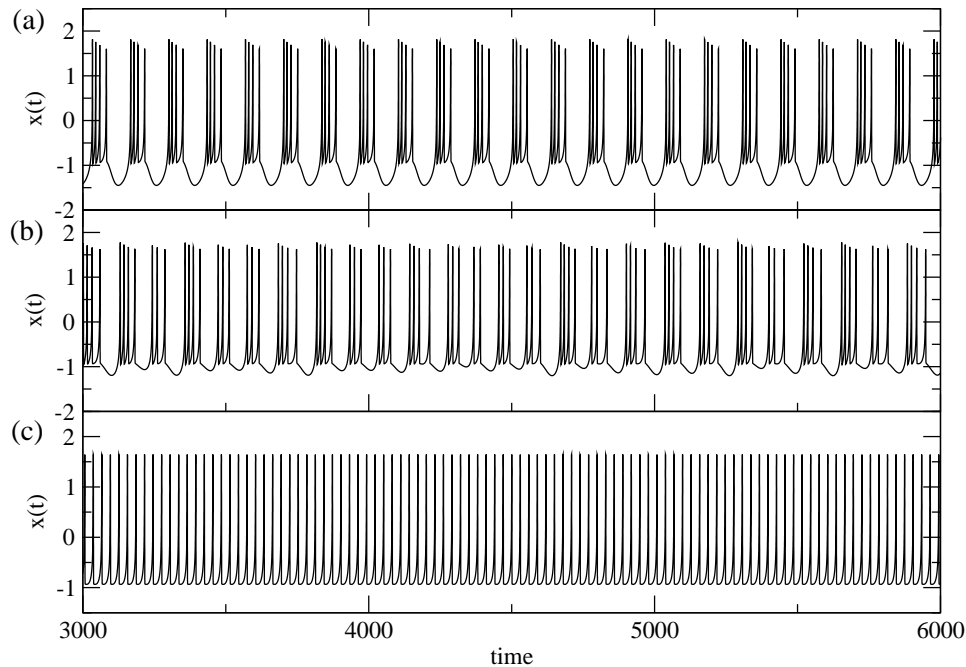


Figure 5.2: Time series of the membrane potential $x(t)$ during (a) periodic bursting, (b) chaotic spiking-bursting and (c) periodic spiking dynamics of the uncoupled ($g = 0$) Hindmarsh-Rose neuron (5.1) stimulated by a DC current with the following strength: (a) $I = 2.6$, (b) $I = 3.1$ and (c) $I = 3.4$.

5.2 Description of the model

Let us consider two diffusively coupled chaotic Hindmarsh-Rose (HR) neurons [39]:

$$\begin{aligned}
 \frac{dx_i(t)}{dt} &= y_i(t) - ax_i(t)^3 + bx_i(t)^2 - z_i(t) + I + I_i^D(t), \\
 \frac{dy_i(t)}{dt} &= c - dx_i(t)^2 - y_i(t), \\
 \frac{dz_i(t)}{dt} &= r[S(x_i(t) - \chi) - z_i(t)],
 \end{aligned} \tag{5.1}$$

where $i = 1, 2$ and $x_i(t), y_i(t), z_i(t)$ represent scaled membrane potential, recovery variable and slow adaptation current of each neuron respectively. We use the standard set of parameters: $a = 1.0$, $b = 3.0$, $c = 1.0$, $d = 5.0$, $S = 4.0$, $r = 0.006$, $\chi = -1.56$. Depending on the strength of constant stimulating current I each neuron in isolation is capable of exhibiting both periodic and chaotic dynamics (see Fig. 5.1). The neuron produces: periodic bursts of spikes for $I \lesssim 2.75$, as in the example on Fig. 5.2(a) where

$I = 2.6$; chaotic bursts of spikes for $2.75 \lesssim I \lesssim 3.25$ as in the example on Fig. 5.2(b) where $I = 3.1$; and periodic spikes for $I \gtrsim 3.25$, as in the example on Fig. 5.2(c) where $I = 3.4$. For the rest of this study stimulating current I was set to 3.07 that put each neuron into chaotic spiking-bursting regime similar to the one depicted in Fig. 5.2(b).

In this model electric synaptic coupling mediates the flow of a diffusive current between the neurons:

$$I_i^D(t) = 2g(t)[x_{i(\bmod 2)+1}(t) - x_i(t)], \quad (5.2)$$

with $g(t)$ being the time-dependent conductance of the synapse. Let us consider the case when $g(t)$ is a slow dynamical variable which depends on the activities $P_1(t), P_2(t)$ of both neurons according to the dynamical model of spike-timing-dependent plasticity [1]:

$$\frac{dg(t)}{dt} = \gamma(P_1(t)P_2(t)^N - P_1(t)^N P_2(t)). \quad (5.3)$$

Here $\gamma = 7 \cdot 10^{-5}$ is a small parameter that provides separation of the timescales between dynamics of the neurons and dynamics of the coupling, exponent N equals 8, auxiliary variables $P_1(t)$ and $P_2(t)$ describe activities of the neurons according to the following dynamical equations:

$$\frac{dP_i(t)}{dt} = F(x_i(t)) - \beta P_i(t), \quad (5.4)$$

where $\beta = 0.2$ and $F(x) = (1 + \exp[-40(x - 0.5)])^{-1}$ is a sigmoid function that is used to threshold neuronal spikes. One can see that $P_1(t)$ and $P_2(t)$ approximately represent low-pass filtered membrane potentials $x_1(t)$ and $x_2(t)$. We note here that the exact values of parameters γ, N, β and the shape of the function $F(x)$ are not crucial to obtain the results presented in our study. Different, but properly chosen values of these parameters would lead to very similar results and identical conclusions, meaning that this type of coupling induces ‘structurally robust’ phenomenon of chaos suppression.

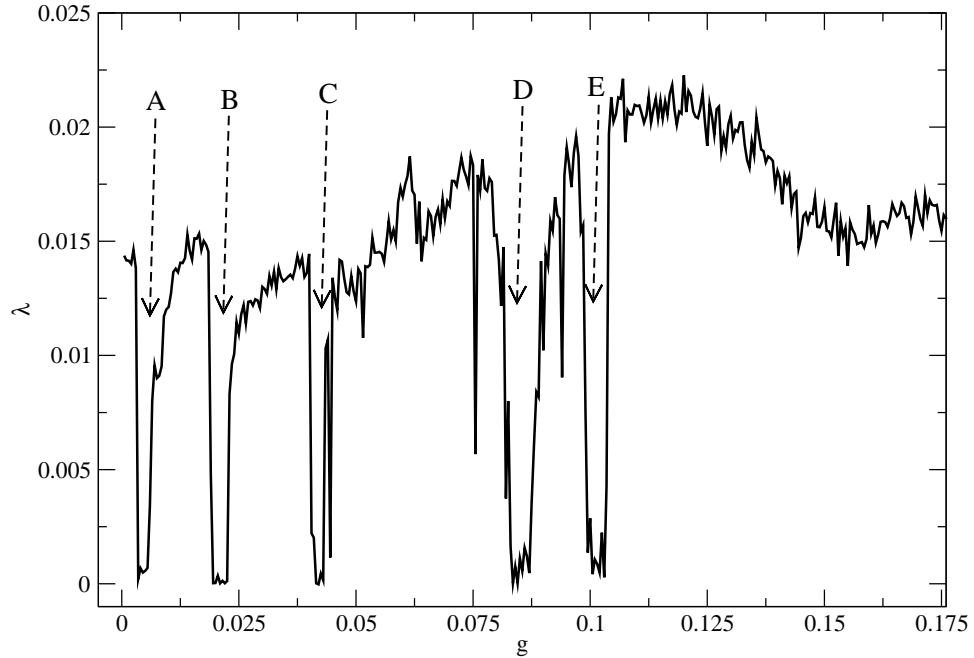


Figure 5.3: Largest Lyapunov exponent λ of a coupled system (5.1)-(5.2) as a function of coupling strength g . Letters A, B, C, D and E indicate windows with different periodic dynamics (see Fig. 5.4).

5.3 Results

Let us first consider the dynamics of the system (5.1) under the assumption of constant coupling strength g . It turns out that this system is chaotic for most values of g from the interval $(0;0.18]$. In Fig. 5.3 we show the result of numerical calculations of its largest Lyapunov exponent (LLE) λ for different values of g from the interval. As one can see, there are several narrow windows (A-E) in which LLE is close to zero within the limits of numerical accuracy. As it was recently discovered [105], these windows correspond to the cases when the neurons interact in such a way that unstable periodic orbits that are present in chaotic dynamics become stable due to so-called *mutual resonant interactions*. In Fig. 5.4 we illustrate corresponding periodic regimes, which are analogous to the generalized splay states [35, 105]. In these periodic states $x_1(t)$ and $x_2(t)$ follow each other with some delay along very similar, but not identical trajectories in the phase space of the system.

Since the dynamical timescales of the system (5.1) and of the coupling strength

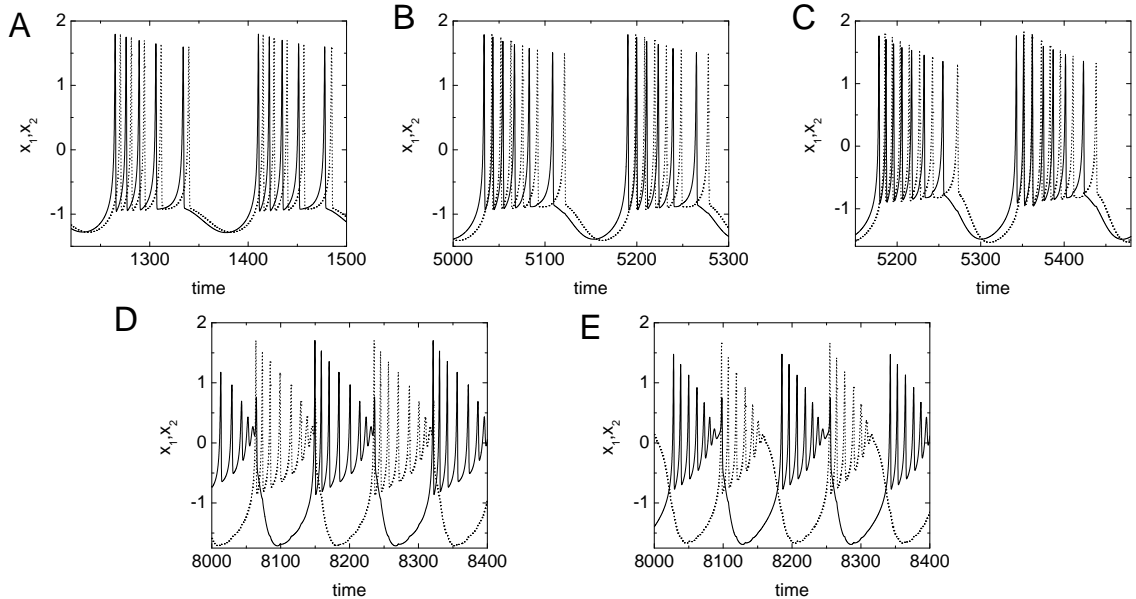


Figure 5.4: Examples of periodic dynamics each corresponding to a window with zero LLE in Fig. 5.3. The following values of synaptic conductance g were used: A – 0.005, B – 0.021, C – 0.042, D – 0.084, E – 0.102.

(5.3) are vastly different, let us now consider the evolution of g under the assumption that it does not influence the dynamics of (5.1) on short time intervals. There are two possible dynamical regimes of the coupled system: periodic and chaotic. As Fig. 5.5(a) illustrates, in the case of periodic dynamics inside the window A the dynamics of g is slaved and is also periodic. To the contrary, g exhibits *random walk* – like dynamics when the system is in chaotic state (see Fig. 5.5(b)).

Let us understand the origin of such behaviors of the synaptic conductance g . First, let us calculate the change of synaptic conductance $\Delta g(t_1, t_2)$ due to synaptic plasticity that is induced by the interaction of a spike from neuron 1 at time t_1 and a spike from neuron 2 at time t_2 . According to (5.3), this change is given by

$$\Delta g(t_1, t_2) = \gamma \int_0^\infty dt \left[P_1(t) P_2(t)^N - P_1(t)^N P_2(t) \right], \quad (5.5)$$

where the values of variables $P_1(t)$ and $P_2(t)$ can be determined by integrating

Eq. (5.4):

$$P_i(t) = \int_0^t dt' e^{-\beta(t-t')} F(x_i(t')). \quad (5.6)$$

Assuming that the duration of spikes is very short as compared to other timescales in the system we can approximate $F(x_i(t))$ by δ -functions:

$$F(x_i(t)) \approx \delta(t - t_i). \quad (5.7)$$

Combining (5.6) and (5.7) and integrating over time we obtain

$$P_i(t) \approx H(t - t_i) e^{-\beta(t-t_i)}, \quad (5.8)$$

where $H(x)$ is the Heaviside function. We are now in the position to calculate $\Delta g(t_1, t_2)$. By substituting (5.8) into (5.5) we obtain

$$\begin{aligned} \Delta g(t_1, t_2) &= \gamma \int_0^\infty dt \left[H(t - t_1) e^{-\beta(t-t_1)} H(t - t_2) e^{-\beta N(t-t_2)} \right. \\ &\quad \left. - H(t - t_1) e^{-\beta N(t-t_1)} H(t - t_2) e^{-\beta(t-t_2)} \right]. \end{aligned} \quad (5.9)$$

Let $t_m = \min(t_1, t_2)$. Then $H(t - t_1)H(t - t_2)$ equals to 0 for $t \leq t_m$ and equals to 1 otherwise. Eq. (5.9) then becomes

$$\begin{aligned} \Delta g(t_1, t_2) &= \gamma \left[e^{\beta(t_1+Nt_2)} - e^{\beta(Nt_1+t_2)} \right] \int_{t_m}^\infty e^{-\beta(1+N)t} dt \\ &= \gamma \left[e^{\beta(t_1+Nt_2)} - e^{\beta(Nt_1+t_2)} \right] \frac{e^{-\beta(1+N)t_m}}{\beta(1+N)}. \end{aligned} \quad (5.10)$$

Now, if $t_1 > t_2$ then $t_m = t_2$ and

$$\Delta g(t_1 > t_2) = \frac{\gamma}{\beta(1+N)} \left[e^{-\beta N(t_1-t_2)} - e^{-\beta(t_1-t_2)} \right]. \quad (5.11)$$

If $t_2 > t_1$ then $t_m = t_1$ and

$$\Delta g(t_2 > t_1) = \frac{\gamma}{\beta(1+N)} \left[e^{-\beta(t_2-t_1)} - e^{-\beta N(t_2-t_1)} \right]. \quad (5.12)$$

Let $\tau = t_1 - t_2$, then (5.11) and (5.12) can be written as

$$\Delta g(\tau) = \text{sign}(\tau) \frac{\gamma}{\beta(1+N)} \left[e^{-\beta|\tau|} - e^{-\beta N|\tau|} \right]. \quad (5.13)$$

According to Eq. (5.13), g changes by $\Delta g(\tau)$ due to each pair of spikes that are separated by a time interval τ . Therefore, in the case of chaotic spiking of both neurons the sequence of interspike intervals τ_i is also chaotic and g changes in a chaotic way that is approximately described by (5.13). In the case of periodic spiking of both neurons the sequence of interspike intervals is such that it results in no net change in g after one burst (see, *e.g.*, Fig. 5.5(c)).

In Fig. 5.6 we show typical evolution of the slow variable g over an extended period of time. Initially coupling strength demonstrates random-like variations and then it gets on the limit cycle close to $g = 0.022$ which corresponds to the boundary of a periodic window B in Fig. 5.3. As soon as this periodic state is reached g stays on the limit cycle indefinitely. In such a way the system with plastic coupling (5.1-5.3) reaches periodic state by means of its own dynamics. Hence the system exhibits self-control and suppression of chaotic dynamics. One can also interpret this process as a self-adaptation of the system to the edge of chaotic region in its state space.

By performing extensive simulations we tested the described above mechanism of chaos regularization for different initial values of coupling strength g_0 . After running several rounds of simulations for each g_0 we have found that this mechanism is robust and the system consistently and independently of the initial conditions and initial coupling strength g_0 reaches one of the stable periodic states. Interestingly, states A, B and D are stable while states C and E are unstable, meaning that we have never observed a limit cycle behavior of g in windows C and E. The identity of the periodic stable state that is reached by the system depends on g_0 and can vary from trial to trial. Periodic state A is usually reached for $g_0 \lesssim 0.02$, either A or B can be reached for $0.02 \lesssim g_0 \lesssim 0.08$ and either B or D can be reached for $0.08 \lesssim g_0 \lesssim 0.18$. We confirmed the observation of robust adaptation to periodic states by calculating the largest Lyapunov exponent of the system (5.1-5.3) λ as a function of g_0 (see Fig. 5.7).

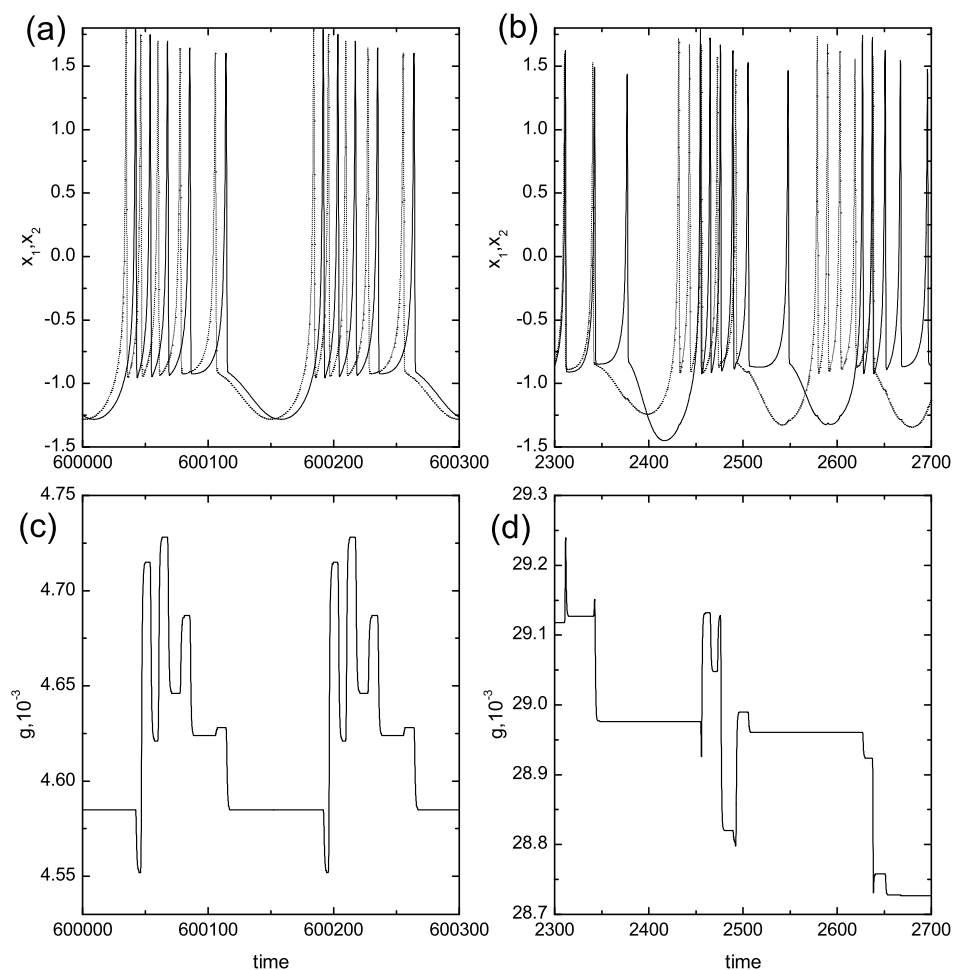


Figure 5.5: Dynamics of the scaled membrane potentials x_1 and x_2 (top) and of the coupling strength g (bottom) in the cases of (a),(c) periodic and (b),(d) chaotic dynamics of the coupled system.

The calculation was done at uniformly distributed points on g_0 axis with a fixed step size of 0.002. Within the numerical accuracy we found λ to be zero regardless of the initial conditions and the value of g_0 from the interval $(0;0.18]$. Hence, regularization of chaos by plastic electrical coupling is robust in the considered region of parameter space.

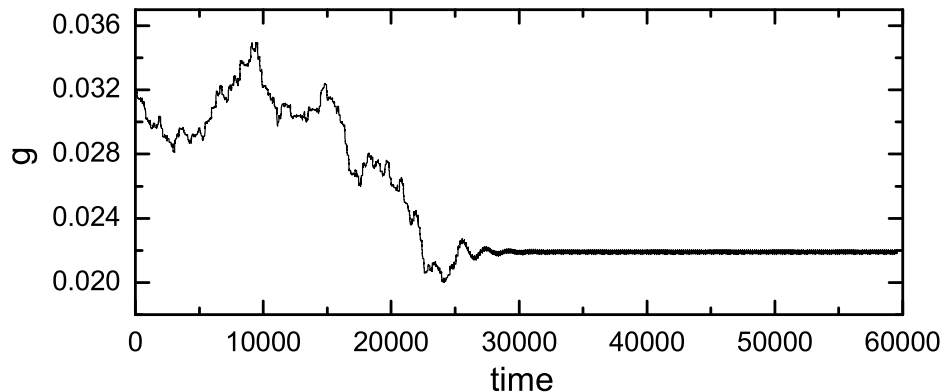


Figure 5.6: Example of the typical slow dynamics of the coupling strength. After the initial random-like behavior g gets on the stable limit cycle.

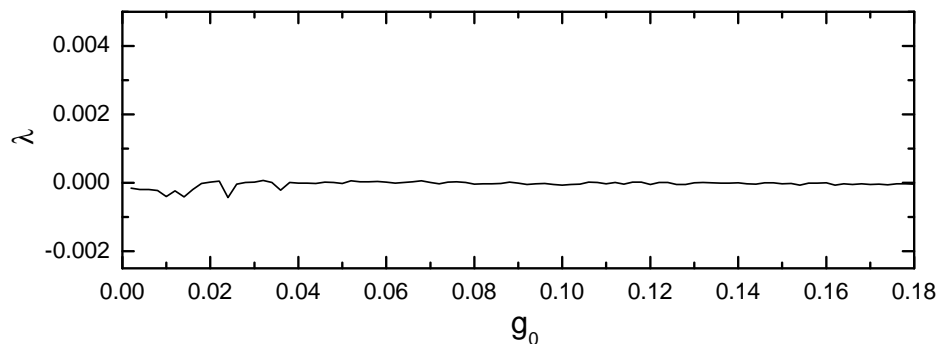


Figure 5.7: Largest Lyapunov exponent λ as a function of the initial conductance g_0 of the plastic synapse.

5.4 Discussion

As we have illustrated above, the described coupled system adapts to periodic states on the boundary of chaotic region or so-called *edge of chaos* (EOC). Systems that are able to adapt its state to the edge of chaos have recently attracted a lot of interest because this state is believed to be optimal for the system to exhibit deterministic, but at the same time flexible dynamics. For example, it was found that EOC state is beneficial for information transmission in neural networks [33]. Also, at the point of order-chaos transition ‘statistical complexity’ of chaotic systems reaches its maximum [20].

In the recent work by Melby *et al.* [64] a phenomenon similar to the one that is described here was observed. They have studied the dynamics of the logistic map with its parameter being controlled by a feedback mechanism involving low-path filtered dynamics of the map. One can argue that a similar mechanism is at work here since the variables P_1 and P_2 are close to being low-path filtered membrane potentials of the neurons and coupling strength g is a slow function of P_1 and P_2 .

In conclusion, we would like to emphasize the differences between the traditional methods of chaos control and the methods discussed above. Most of the traditional approaches are based on either one of the following two ideas. The first one is the algorithm of Ott, Grebogi and Yorke [70], i.e., suppression of chaos by occasional application of small, well calculated perturbations to parameters of the system and thus stabilization of one of the embedded unstable periodic orbits. The second one is the method of continuous-time control [73] that uses recovery of the unstable periodic behavior by delay coordinated method. Our method also achieves control by continuously perturbing an intrinsic parameter of the system, e.g., the strength of synaptic coupling, but in a different way. In our case strength of the coupling between chaotic subsystems depends nonlinearly on the distance between their output signals. Periodic activity is then generated by chaotic subsystems themselves due to the control of coupling strength through nonlinear filtering of their signals. We suggest that such mechanism can be used in other coupled chaotic systems as well.

Chapter 6

Dynamical motifs: Building blocks of complex dynamics in neural networks

6.1 Introduction

Dynamics in networks underlie functioning of many complex systems such as the brain [48], cellular regulatory machinery [32], ecosystems [49] and many others. These systems exhibit a wide repertoire of dynamics, ranging from periodic oscillations in cell cycle and brain rhythms to chaos in food webs and chemical reactions. Recently, rapid advancements had been made in our understanding of statistical properties of natural and artificial networks (for reviews, see [4, 21, 68]), and of traffic dynamics [93] and transport processes [92, 87] on them. However, still very little is understood about oscillatory dynamics in such networks. This is due to several reasons, in particular, inadequacy of the methods of nonequilibrium statistical mechanics in the domain of heterogeneous mesoscopic systems and inability of the dynamical systems theory to deal with systems having more than order-1 dimensions.

Fundamental problem which one faces while trying to understand dynamics in complex networks is the strong influence of their structure on their non-Hamiltonian dynamics. This influence induces long-term connectivity-dependent spatio-temporal correlations which present formidable problem for understanding of the dynamics. Statistical methods allow us to solve this problem in the limit of infinite-size net-

works [88], but they are not applicable to the study of realistic networks with non-uniform connectivity and a relatively small size.

It was recently found that many real networks include statistically significant subnetworks, so-called *motifs*, in their structure [66]. Here we suggest the use of *dynamical motifs* – small subnetworks with non-trivial dynamics – as a new approach to the study of oscillatory dynamics in complex networks. In this approach we combine dynamical and statistical methods to identify dynamical motifs and evaluate probability of their occurrence in the structure of networks. We show that the emergence of periodic and chaotic dynamics in networks of increasing structural complexity is linked to the appearance of periodic and chaotic motifs in their connectivity. We also consider spatially distributed networks with local connectivity and show that chaotic motifs are absent in their structure. We suggest that this approach may be useful for studies of oscillatory dynamics in networks of arbitrary structure and size.

6.2 Description of the model

In many complex systems the dynamics of individual elements and the rules of their interaction are relatively simple and the resulting complex behavior is an *emergent* consequence of these interactions. Hence, in order to study the influence of the structure on the dynamics of networks let us focus on models with simplest interactions and dynamics at each node. Let $x_i(t) \in [0; 1]$, $i = 1, \dots, N$ be a set of variables describing properly scaled states of N elements connected in a network. Consider the time evolution of network's state vector $\mathbf{X}(t) = \{x_1(t), x_2(t), \dots, x_N(t)\}$ described by the following set of first order differential equations

$$\frac{d\mathbf{X}(t)}{dt} = -\mathbf{X}(t) + \mathbf{F}(\mathbf{X}(t)), \quad (6.1)$$

where $\mathbf{F}(\mathbf{X}) = \{f_1(\mathbf{X}), f_2(\mathbf{X}), \dots, f_N(\mathbf{X})\}$ is a set of sigmoid nonlinearities with $[0; 1]$ value ranges. This general class of models includes continuous version of random Boolean (genetic) networks (cRBN) [65, 31], in which $f_i(\mathbf{X})$ are randomly chosen

Boolean functions of their arguments, and continuous-time artificial neural networks (cANN) [41], in which $f_i(\mathbf{X}) = f((\hat{W} \cdot \mathbf{X})_i + \sigma_i)$, where \hat{W} is the coupling matrix and σ_i are thresholds. Both of these models were shown to exhibit complex periodic and chaotic dynamics in the biologically relevant cases of intermediate probabilities of gene expression in cRBN [31] and non-symmetric interactions in cANN [88]. Corresponding discrete-time, two-state models also exhibit disordered dynamics (see, *e.g.*, [5] for RBN and [6] for ANN models).

To illustrate the use of dynamical motifs we employ a simple cANN model

$$\frac{dx_i(t)}{dt} = -x_i(t) + f((\hat{W} \cdot \mathbf{X}(t))_i + \sigma_i), \quad (6.2)$$

with $f(x) = (1 + \exp(-20x))^{-1}$, uniform external excitation $\sigma_i = \sigma = 0.5$ and inhibitory interactions of the same strength: $\hat{W} = -\hat{G}w$, where $w = 5$ and \hat{G} is the adjacency matrix of the directed graph on which the network is defined. In this setting the model is similar to the simplified version of a balanced network model [98] with excitatory connections replaced by a uniform excitatory field and can be viewed as a simple model of a cortical microcircuit. It is also an extension of the concept of winnerless competitive networks [77] to the case of random connectivity. However, methods presented in this Letter can be used for other models of the dynamics, such as Lotka-Volterra competition, etc.

6.3 Results

6.3.1 Dynamics in Erdős-Rényi networks

We have performed Monte Carlo simulations of the described above cANN model defined on an ensemble of random networks with $N = 200$ nodes and uniform probability p of node-to-node connections, *i.e.*, an Erdős-Rényi (ER) ensemble. A sample of $2 \cdot 10^4 p$ random networks was generated for each considered p and cANN dynamics was simulated 100 times on each of the networks, each time starting with different initial condition taken at random from the hypercube $R_{(0,1)}^{200}$. Sets of initial condi-

tions were considered in order to eliminate the influence of the basins of attraction in multistable networks which in itself is a very complicated issue.

Simulations of cANN dynamics in networks with different realizations of connectivity \hat{G} revealed different dynamical behaviors of these networks, such as fixed point dynamics (examples are presented in Figs. 6.1 and 6.2), periodic dynamics (Figs. 6.3 and 6.4) and chaotic dynamics (Figs. 6.5 and 6.6). In some cases, such as the one depicted in Fig. 6.2, long chaotic transients were observed before the settling of the dynamics on fixed point or periodic attractor. It is well known that transients may be very long in high-dimensional chaotic dynamical systems such as the one under study. While observing chaos in such systems, there is no way to tell the difference between long chaotic transients and genuinely chaotic dynamics. Hence, to maximally diminish the influence of chaotic transients on the results of this study, each simulation was run for 2000 time units. This time was determined as being long enough by observing that most transients die out after several hundred time units of simulations.

Some of the networks exhibited the same type of dynamics regardless of initial conditions, while others demonstrated multistability, with different initial conditions leading to different types of dynamics. Usually only two types of dynamics out of three were observed in multistable networks. In order to perform automatic classification of networks according to their dynamical behavior largest Lyapunov exponent λ was calculated in each simulation. Networks with at least one initial condition leading to $\lambda \in (-0.005; 0.005)$, typically $\lambda \sim 10^{-4}$ were classified as having limit cycle dynamics and with $\lambda > 0.005$, typically $\lambda \sim 10^{-1}$ as having chaotic dynamics. The relative frequency with which each type of dynamics was observed in the ensemble of networks was dependent on the density of connections p . In Fig. 6.7 we plot the fraction of networks in the ensemble with given type of dynamics as a function of p . Mostly periodic dynamics was observed in networks with $p < 0.02$. As the density of connection increased above 0.02, networks with chaotic dynamics began to dominate.

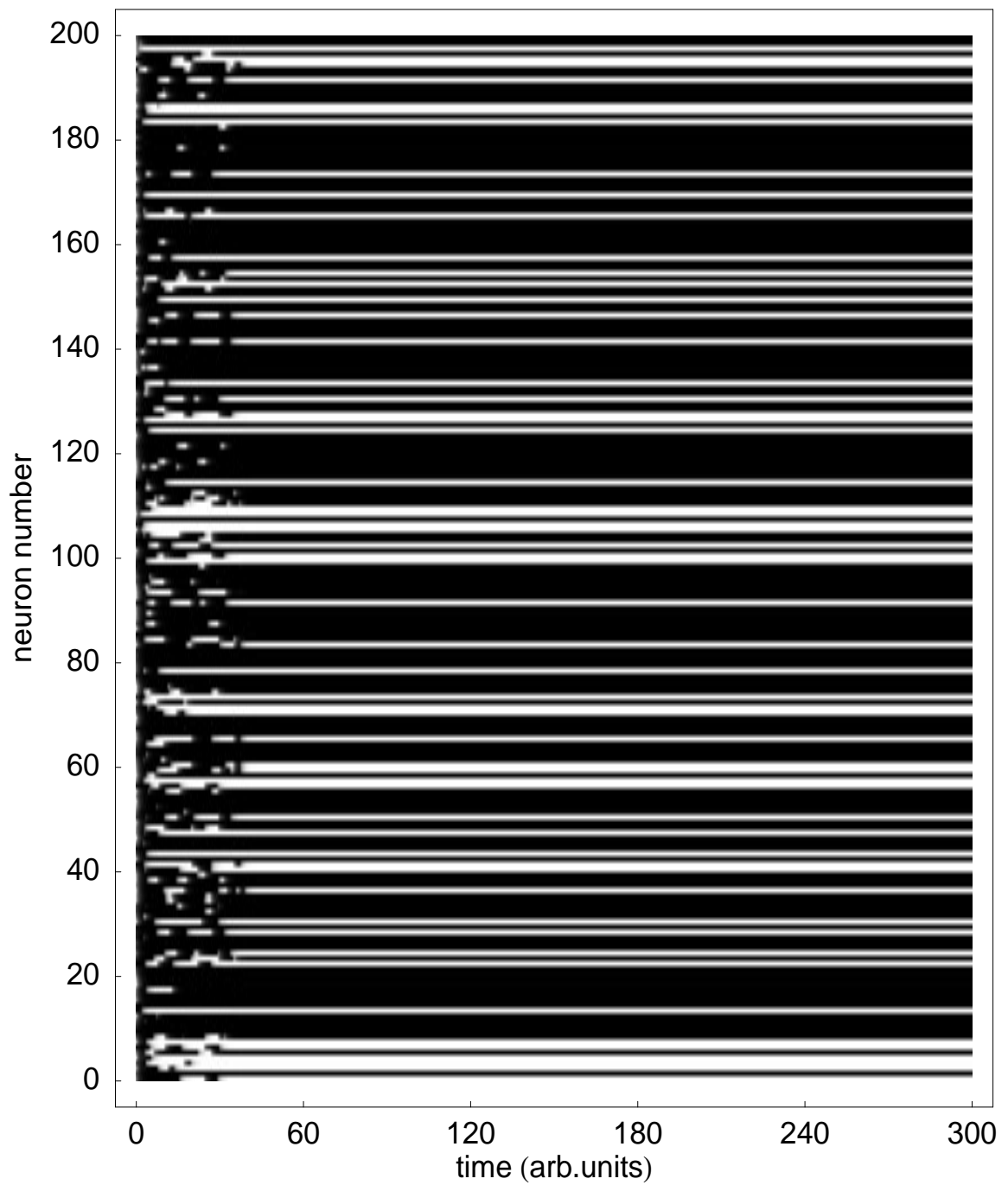


Figure 6.1: Time series of fixed point dynamics in a network. Time goes along the horizontal axis while identity of the neuron - along the vertical. Each horizontal line represents activity of one neuron. Level of neuronal activity is coded by grayscale with black corresponding to the quiet state ($x_i(t) = 0$) and white - to the maximally active state ($x_i(t) = 1$).

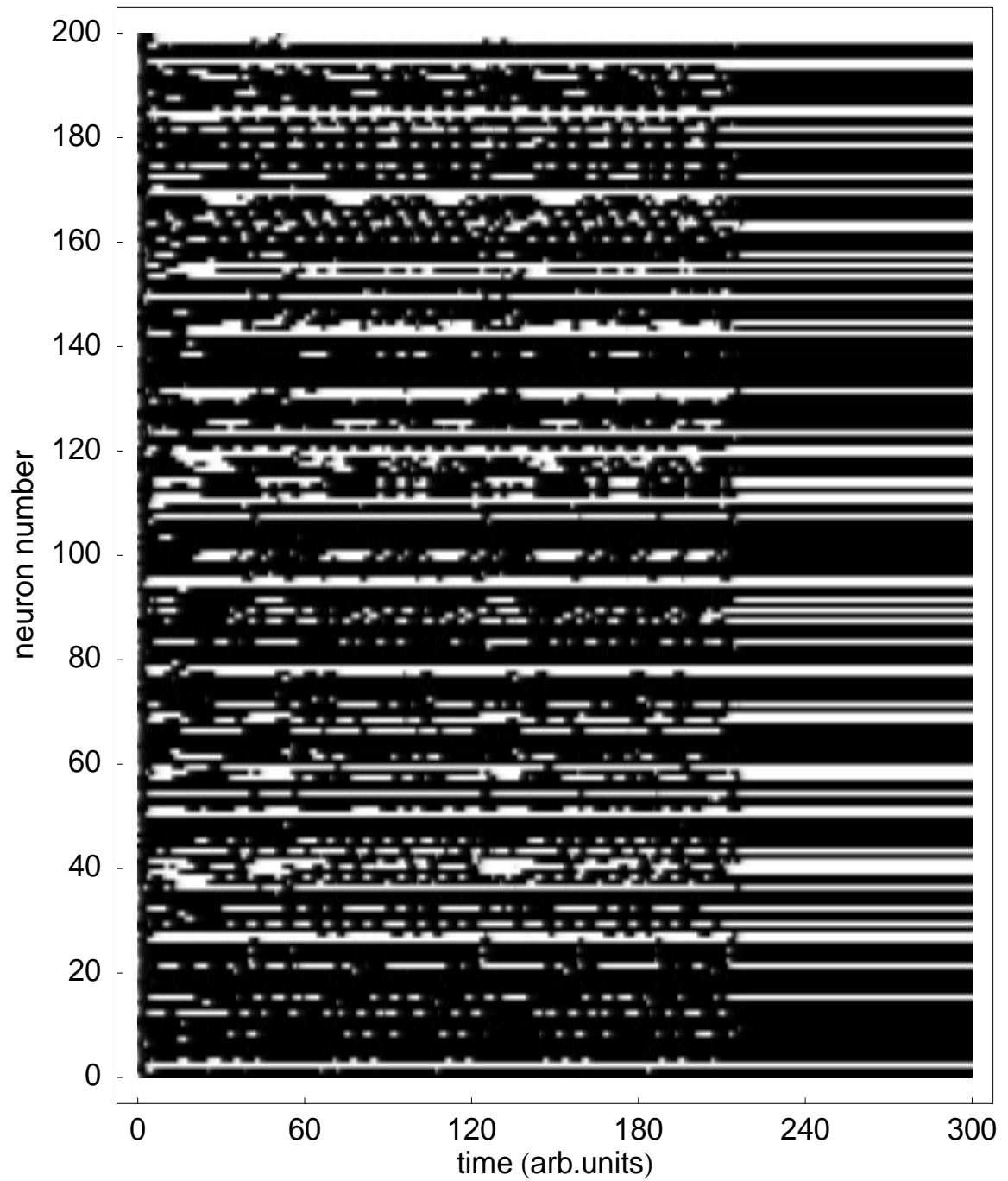


Figure 6.2: Another example of a network with fixed point dynamics. In this case the period of transient chaotic dynamics was rather long. Time series are represented in the same way as in Fig. 6.1.

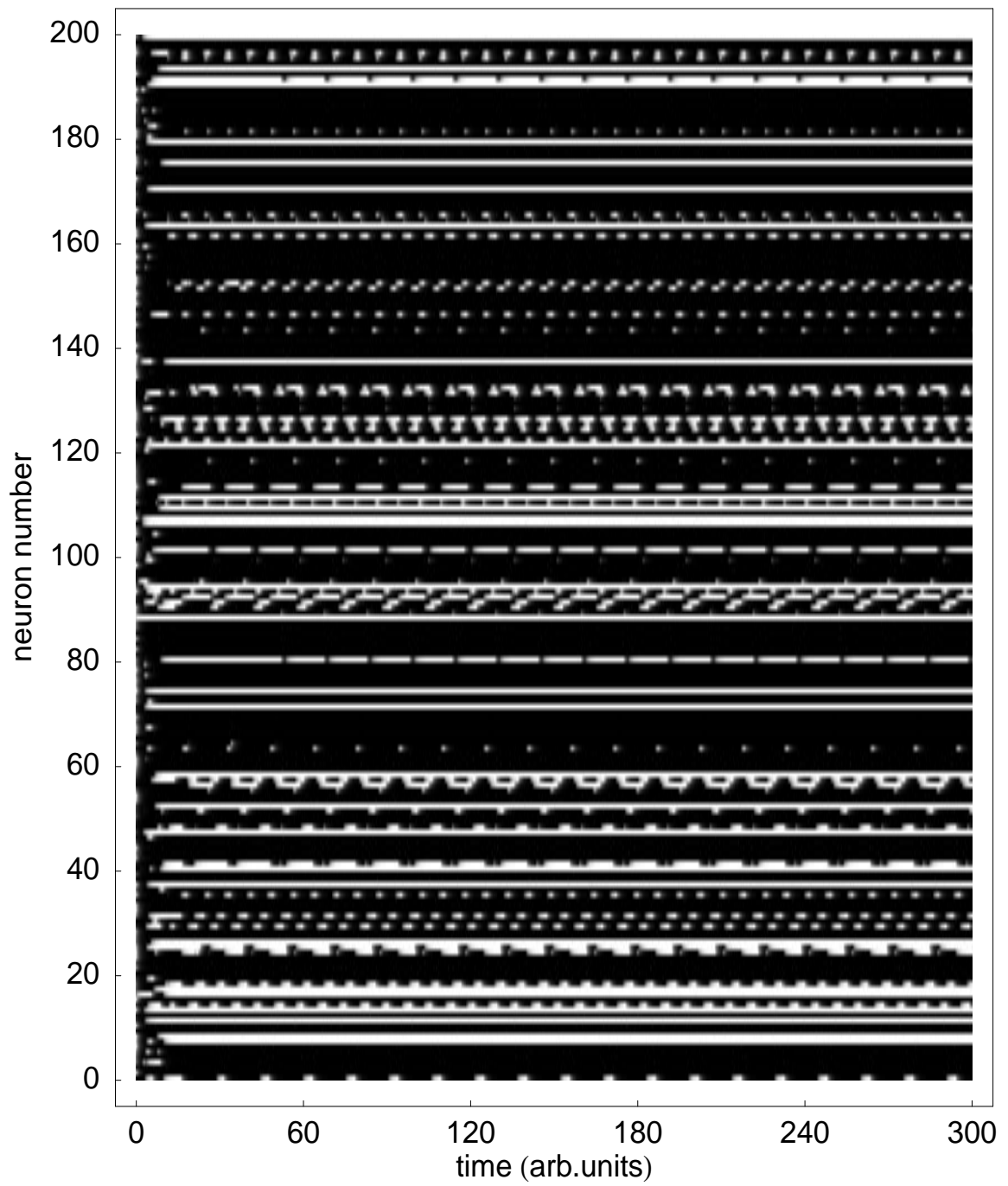


Figure 6.3: Example of a network with periodic dynamics. Time series are represented is the same way as in Fig. 6.1.

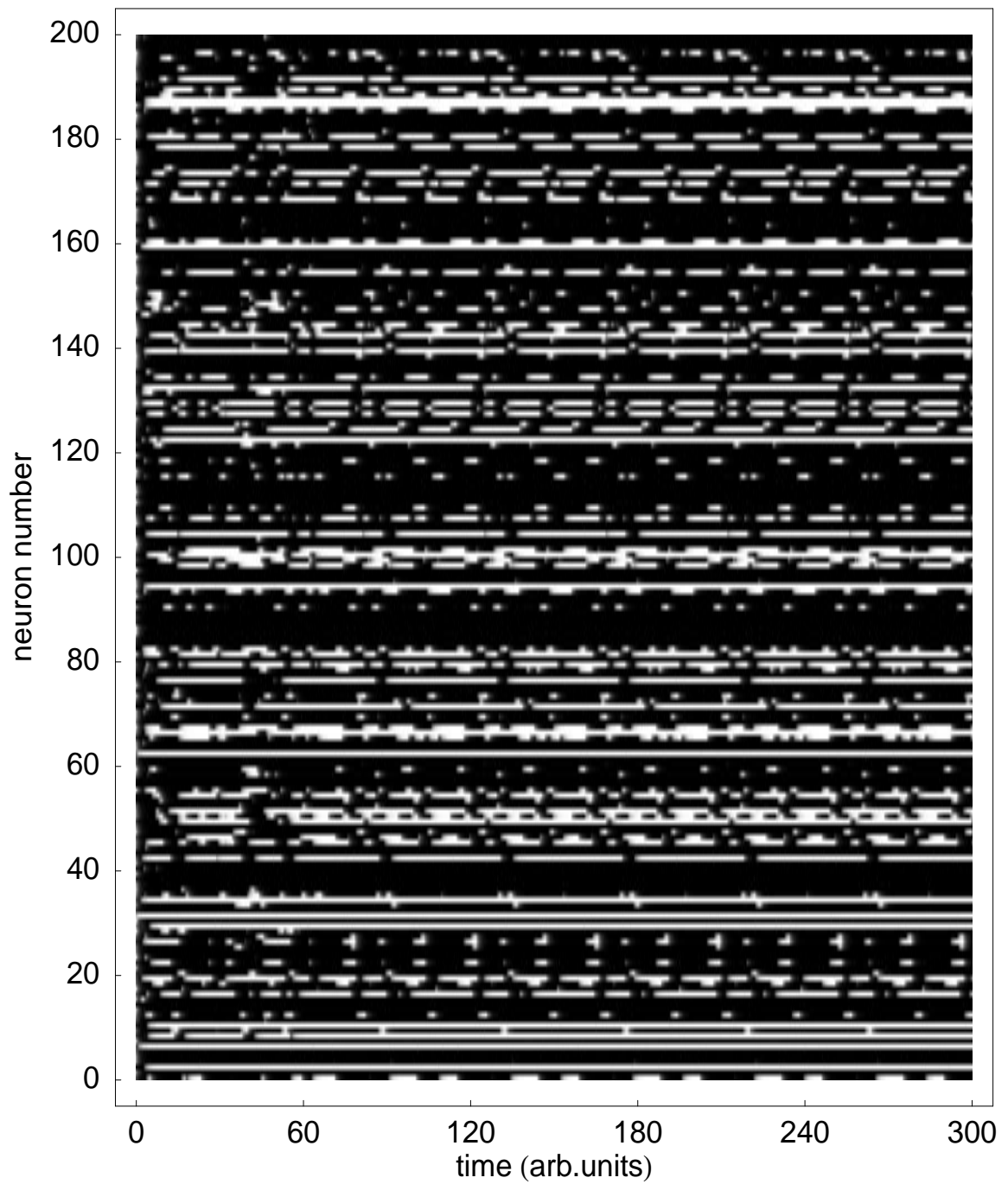


Figure 6.4: Another example of a network with periodic dynamics. In this case periodic dynamics was more complicated and had longer period. Time series are represented is the same way as in Fig. 6.1.

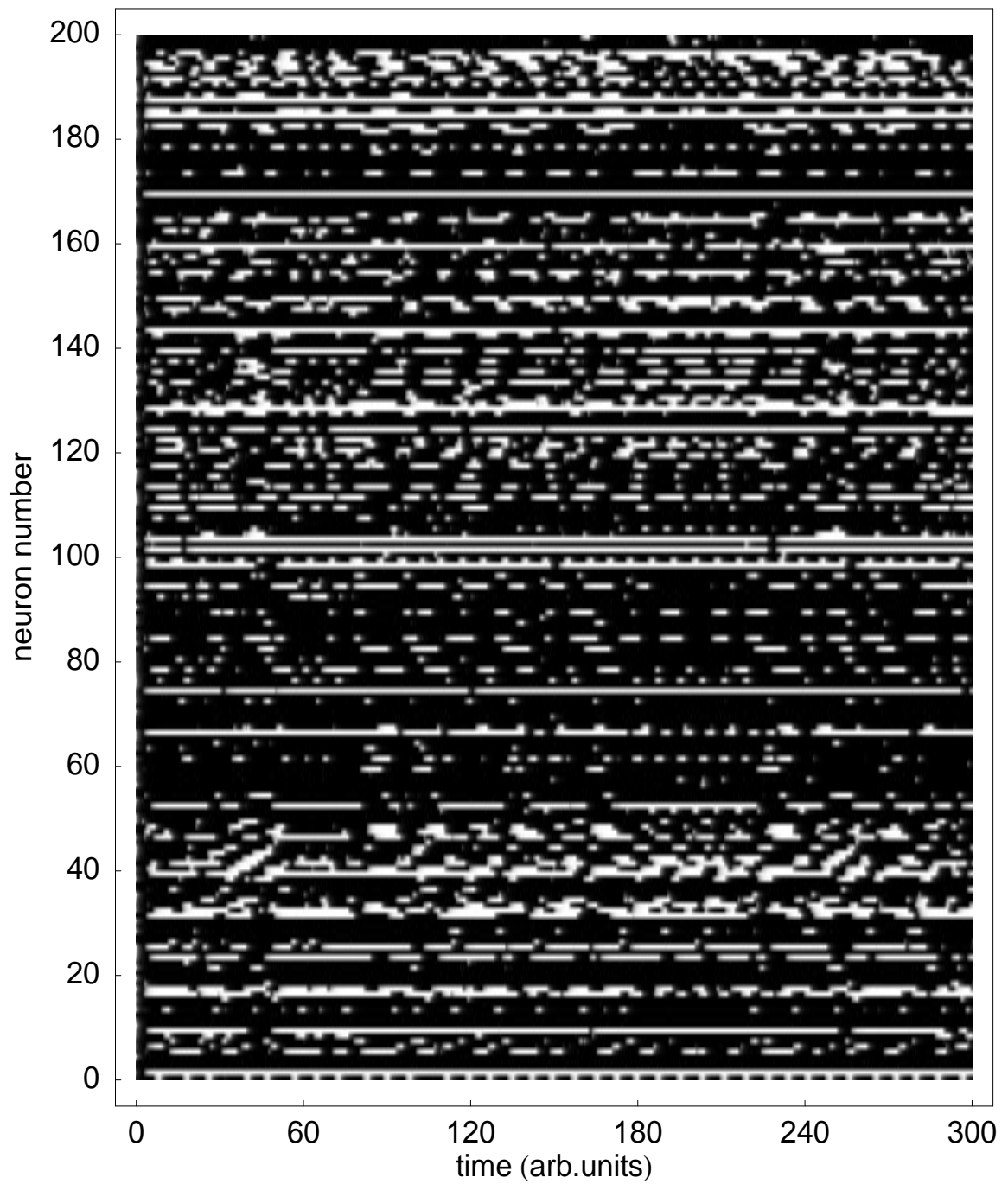


Figure 6.5: Example of a network with chaotic dynamics. Time series are represented is the same way as in Fig. 6.1.

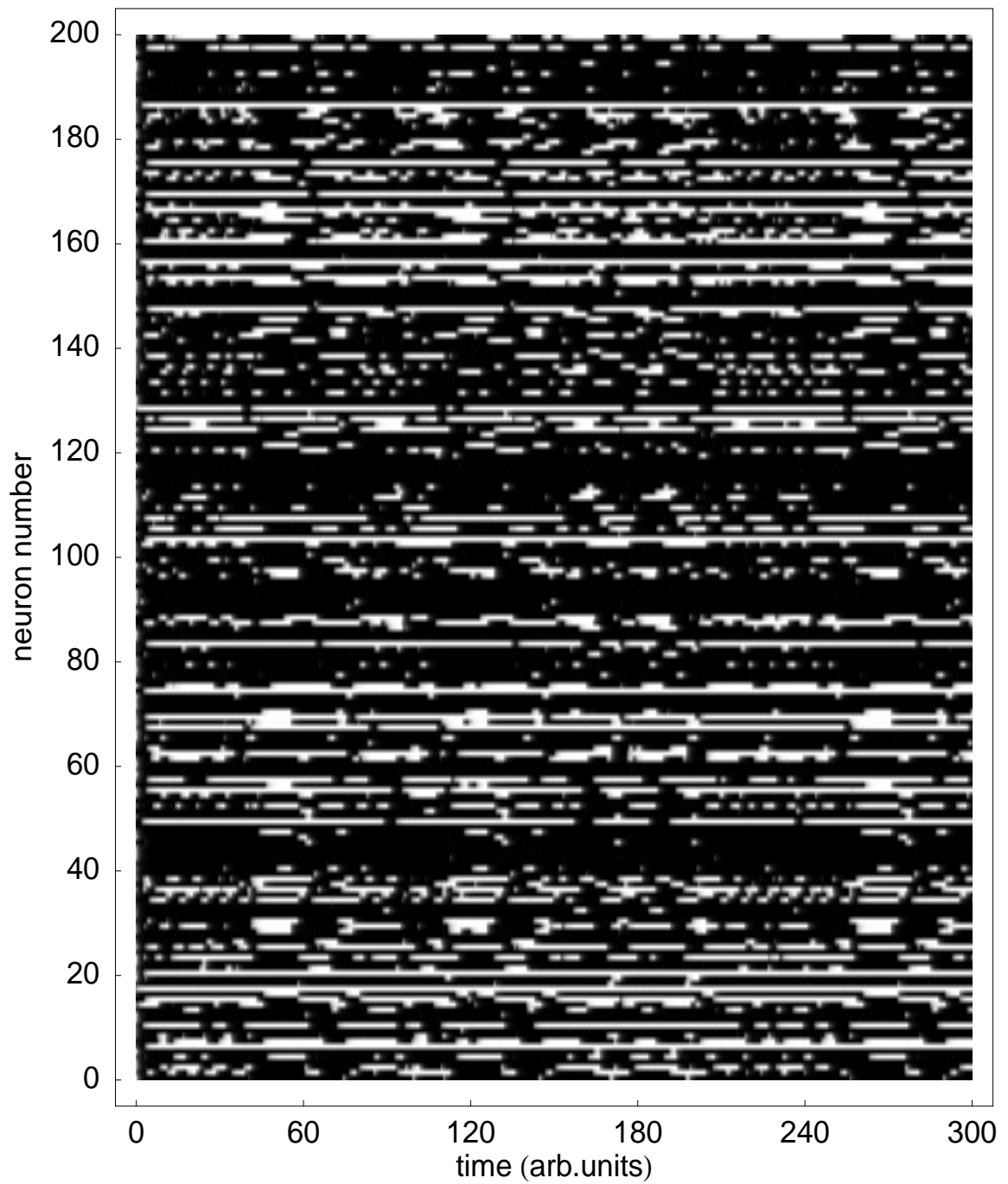


Figure 6.6: Another example of a network with chaotic dynamics. Time series are represented in the same way as in Fig. 6.1.

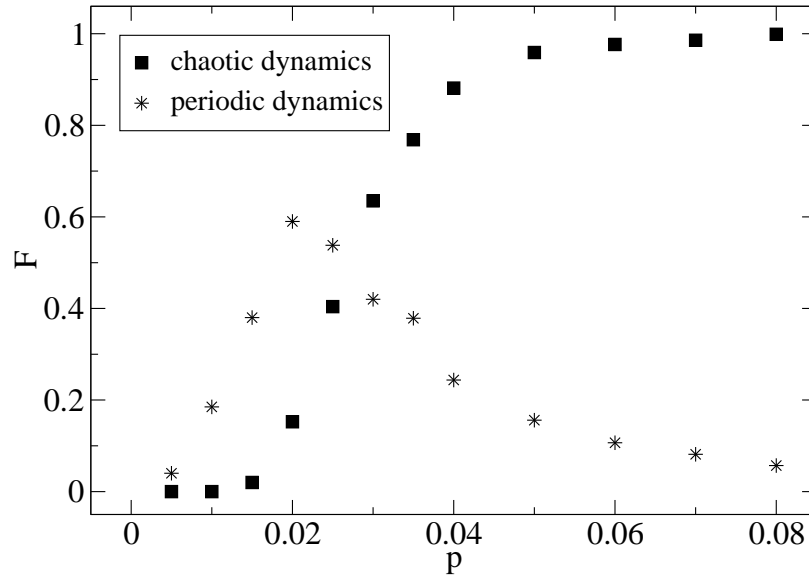


Figure 6.7: Fraction of networks F with periodic (stars) or chaotic (squares) dynamics in simulations of 200-node cANN networks with node-to-node connection probability p .

6.3.2 Dynamical motifs

Let us now apply the concept of dynamical motifs in order to explain these observations and make further predictions about oscillatory dynamics in networks. The main idea behind this approach is that the transition to periodic or chaotic overall dynamics in a given network occurs due to appearance in its structure of small, not necessary isolated, dynamical motifs which have the same type of dynamics. Of course many of them may be present in a given dynamical network, but at least one is needed in order for the network to exhibit a given type of dynamics. The dynamical phase transitions that are observed in models of complex networks are then identified with proliferation of dynamical motifs, *i.e.*, 0-to-1 transitions in the probability of their occurrence.

Let us consider an ER network with the probability of node-to-node connection p . The probability p_n that some n nodes of this network form a given motif with l links and no self-loops is given by

$$p_n = p^l (1 - p)^{n(n-1)-l}. \quad (6.3)$$

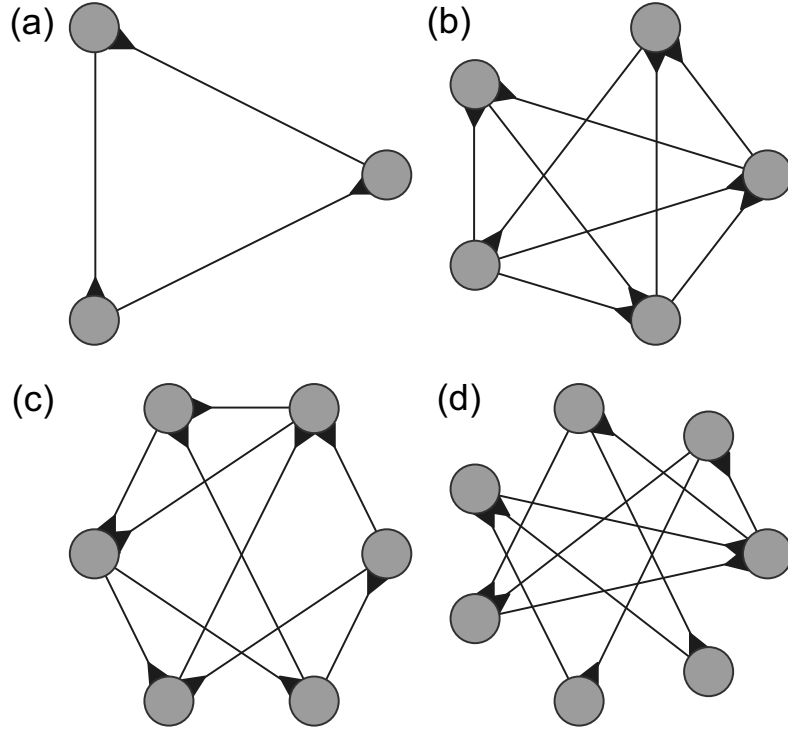


Figure 6.8: Smallest dynamical motifs with periodic (a) and chaotic (b-d) dynamics. Triangles indicate direction of the inhibitory connections.

It is possible that dynamics of some of the nodes in the motif could be permanently suppressed by inhibitory connections from the nodes outside of a motif that are frozen in the ‘+1’ state. The fraction p_f of such frozen nodes in the network can be approximated in the following way. Assume that p_f is well represented by the probability $Prob(x_i = 1)$ for an arbitrary node i to be frozen in the ‘+1’ state. Then from (6.2) it follows that

$$p_f = Prob(x_i = 1) = Prob\left(\sum_{j=1}^N \hat{G}_{ij}x_j = 0\right). \quad (6.4)$$

Since the sum of these non-negative terms has to be equal to zero, each of the terms is required to be zero as well:

$$Prob\left(\sum_{j=1}^N \hat{G}_{ij}x_j = 0\right) = \prod_{j=1}^N Prob(\hat{G}_{ij}x_j = 0). \quad (6.5)$$

Now, let us assume that correlations in the dynamics of different nodes of the network are very weak. We expect this assumption to hold in the limit of sparse connectivity ($p \ll 1$). Under this assumption we can suppose that $Prob(x_j = 1) = Prob(x_i = 1)$ and that the products $\hat{G}_{ij}x_j$ are independent random variables satisfying the same statistics. Then

$$\prod_{j=1}^N Prob(\hat{G}_{ij}x_j = 0) \approx (Prob(\hat{G}_{ij}x_j = 0))^N. \quad (6.6)$$

Let us further assume that x_i can only take on two values: 0 or 1. This assumption is close to satisfaction when the sigmoid function $f(x)$ in (6.2) has a steep slope which is indeed the case here. Then, since \hat{G} is the adjacency matrix and is composed of zeros and ones, the product $\hat{G}_{ij}x_j$ is also limited in its values to 0 and 1. Hence,

$$Prob(\hat{G}_{ij}x_j = 0) \approx 1 - Prob(\hat{G}_{ij}x_j = 1) = 1 - Prob(\hat{G}_{ij} = 1)Prob(x_j = 1). \quad (6.7)$$

Remembering that any connection in the network is present with probability p , i.e., $Prob(\hat{G}_{ij} = 1) = p$ and that $Prob(x_j = 1) = Prob(x_i = 1)$, we obtain

$$1 - Prob(\hat{G}_{ij} = 1)Prob(x_j = 1) = 1 - pp_f. \quad (6.8)$$

Combining equations (6.4) through (6.8) we finally arrive at the following self-consistent equation for the fraction of frozen nodes:

$$p_f = (1 - pp_f)^N. \quad (6.9)$$

Numerical solution of this equation for $N = 200$ is plotted in Fig. 6.9 by a solid line. As one can see, the agreement with the data from our simulations of cANN dynamics (represented by squares) is good while connectivity is very sparse ($p < 0.01$). Above $p = 0.01$ the difference between our theoretical approximation and the data increases with increasing p . This occurs because our assumption about the weakness of correlations in the dynamics of nodes starts to break as density of connections p

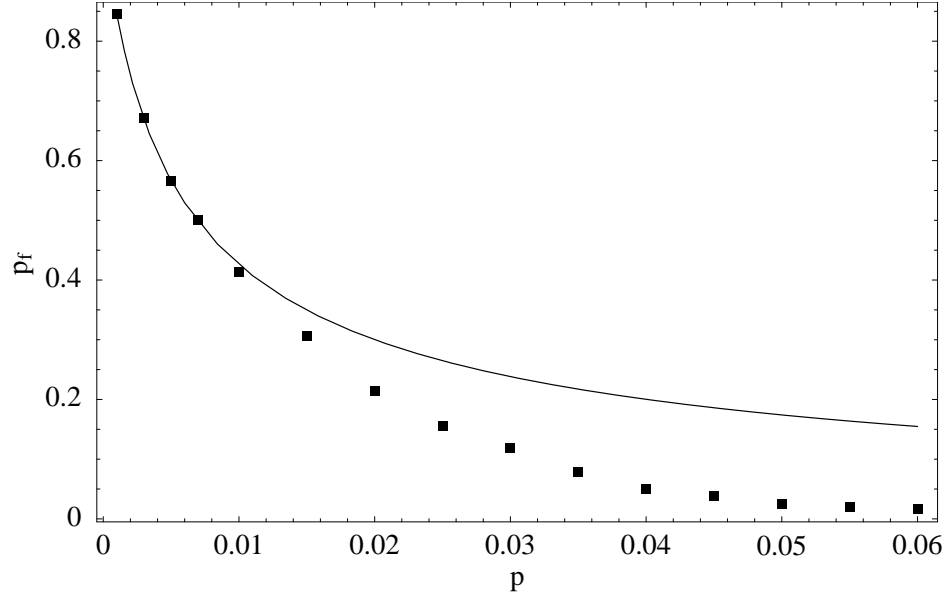


Figure 6.9: Theoretical estimation of the dependence of fraction of frozen nodes p_f in the network on the density of connections p (solid line) and its values that were calculated from simulations (squares).

increases above 0.01. In what follows we are going to use the interpolation of p_f that was calculated from its numerical estimation (Fig. 6.9, squares).

Let us now turn back to the calculation of the probability of motif occurrence in ER networks. We have found that the probability for any n nodes of the network to form a motif with l links is given by (6.3). Inputs from any of the frozen nodes (of which there are $N_f = p_f N$) would suppress dynamics in the motif and hence should be excluded. By doing so we obtain the corrected probability

$$p_{nf} = p^l (1 - p)^{n(n+N_f-1)-l}. \quad (6.10)$$

It is difficult to calculate exactly the probability to find a given number of such motifs in a network. However, an approximate calculation of the probability $P_{(n;l)}$ to encounter one or more motifs is relatively straight forward and is expected to work well in the case of sparsely connected networks ($p \ll 1$). This probability can be written as

$$P_{(n;l)} = 1 - p(N_{(n;l)} = 0), \quad (6.11)$$

where the probability $p(N_{(n;l)} = 0)$ of not finding any such motifs in a sparsely connected network can be approximated by treating each set of n nodes independently and requiring the absence of the motif in each such set of nodes. Under this approximation,

$$p(N_{(n;l)} = 0) \approx (1 - p_{nf})^{\frac{N!}{A(N-n)!}} \approx \exp\left(-\frac{p_{nf}N!}{A(N-n)!}\right), \quad (6.12)$$

where $N!/(A(N-n)!)$ is the number of ways to pick n nodes of the motif from the N -node network multiplied by $n!/A$ – number of ways to label a motif, with A being the order of motif's automorphism group. Hence, combining (6.11) and (6.12) we obtain

$$P_{(n;l)} \approx 1 - \exp\left(-\frac{p_{nf}N!}{A(N-n)!}\right). \quad (6.13)$$

This formula predicts proliferation of motifs with n nodes and l links at some intermediate value of p which depends on n and l . We are interested in the values of n and l for which proliferation occurs at the smallest $p = p_c$. Let us define it by the point where $P_{(n;l)} = 1/2$. Then

$$\frac{N!}{(N-n)!A} p_c^l (1 - p_c)^{n(n+f-1)-l} = \log 2. \quad (6.14)$$

Assuming $N \gg n$ and $p_c \ll 1$ we get

$$N^n p_c^l \approx A \log 2, \quad (6.15)$$

and, hence,

$$p_c \sim A^{1/l} N^{-n/l}. \quad (6.16)$$

This result indicates that in order to minimize p_c , n/l should be maximized and hence subnetworks with most nodes and least links will appear first as p is increased from 0.

Subnetworks with limit cycle dynamics include 3-loop (Fig. 6.8(a)), 4-loop and other, more complicated, structures. Since for the n -loop $l = n$ and $A = n$, 3-loop

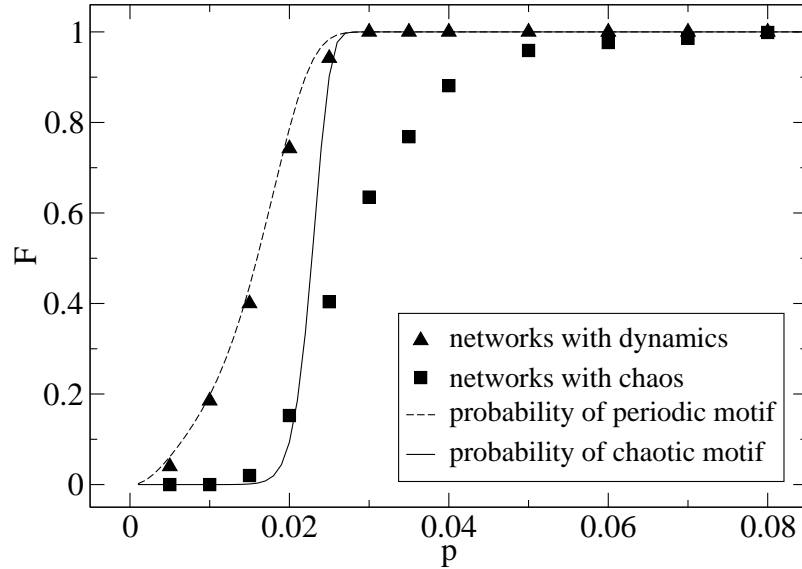


Figure 6.10: Fraction of networks F with either periodic or chaotic (triangles) and only chaotic (squares) dynamics in simulations of 200-node cANN networks with node-to-node connection probability p . Lines represent predictions based on the probability of occurrence of periodic (dashed line, Eq. (6.17)) and chaotic (solid line, Eq. (6.18)) motifs.

has smallest p_c . According to (6.13), its probability of occurrence is given by

$$P_{(3;3)} \approx 1 - \exp\left(-\frac{N^3}{3}p^3(1-p)^{3(1+f)}\right) \quad (6.17)$$

and is plotted in Fig. 6.10 by a dashed line (with f evaluated numerically from simulations). This estimate predicts the appearance of dynamics in ER networks very accurately.

In order to find chaotic motifs we used the *nauty* package [62] to generate all possible non-isomorphic directed graphs with up to 8 nodes and 11 links. Even though the total number of n -node directed graphs growth like 2^{n^2} , which is approximately $6.8 \cdot 10^{10}$ for $n = 6$, the number of non-isomorphic directed graphs growth much slower, there are, for example, approximately $1.5 \cdot 10^6$ of them for $n = 6$. This fact made it feasible to study all non-isomorphic digraphs with up to 8 nodes. We simulated the cANN dynamics on them and calculated the largest Lyapunov exponent λ for each. Digraphs with $\lambda > 0.005$, typically $\lambda \sim 10^{-1}$ were classified as chaotic. Not

surprisingly, most of these small digraphs were found to have no dynamics, quite a few had periodic dynamics and very few exhibited chaotic dynamics. In Fig. 6.8(b-d) we show the first three chaotic motifs in the order of increasing number of nodes (5, 6 and 7 nodes) and minimal number of links (9, 10 and 10 links). Also, we found six non-isomorphic chaotic motifs with 8 nodes and 11 links, four of them with $A = 2$ and two with $A = 1$. Numerical evaluations of p_c according to (6.14) indicate that the latter motifs have smallest $p_c \approx 0.025$. Probability to find one or more of them in an ER network is given by

$$P_{(8,11)} \approx 1 - \exp(-4N^8 p^{11} (1-p)^{45+8f}) \quad (6.18)$$

and is plotted in Fig. 6.10 by a solid line (with f evaluated from simulations of chaotic networks). As can be seen from the plot, this prediction is reasonably good. The discrepancy may be caused by the approximate nature of the estimate (6.13), severe undersampling of the network space in simulations and disregard of the fact that not only frozen, but also periodically oscillating external nodes suppress chaos in these motifs.

While the origin of periodic dynamics in n -loops is obvious as they merely are negative feedback loops, the nature of chaos in chaotic motifs is not self-evident. As one can see from Figs. 6.8(b-d), these chaotic motifs consist of multiple interconnected feedback loops of different lengths – configuration that frequently leads to chaotic dynamics. We have traced the route to chaos in the first chaotic motif by lowering w to 0.5 and then gradually increasing it. In Fig. 6.11 the bifurcation diagram of the local maxima of $x_1(t)$ oscillations is plotted. This diagram reveals two period doubling cascades, one starting around $w = 0.7$ and another one around $w = 2.5$. In order to confirm presence of these cascades in Fig. 6.12 we plot projections of the phase space on the $(x_2(t), x_3(t))$ plane which were calculated for $w = \{2.4, 2.6, 2.7, 2.8\}$. These projections illustrate that at $w = 2.4$ dynamics consisted of a simple limit cycle. Its period doubled before $w = 2.6$ and quadrupled before $w = 2.7$. Fully developed chaotic dynamics was already seen at $w = 2.8$. Similar period doubling cascades were

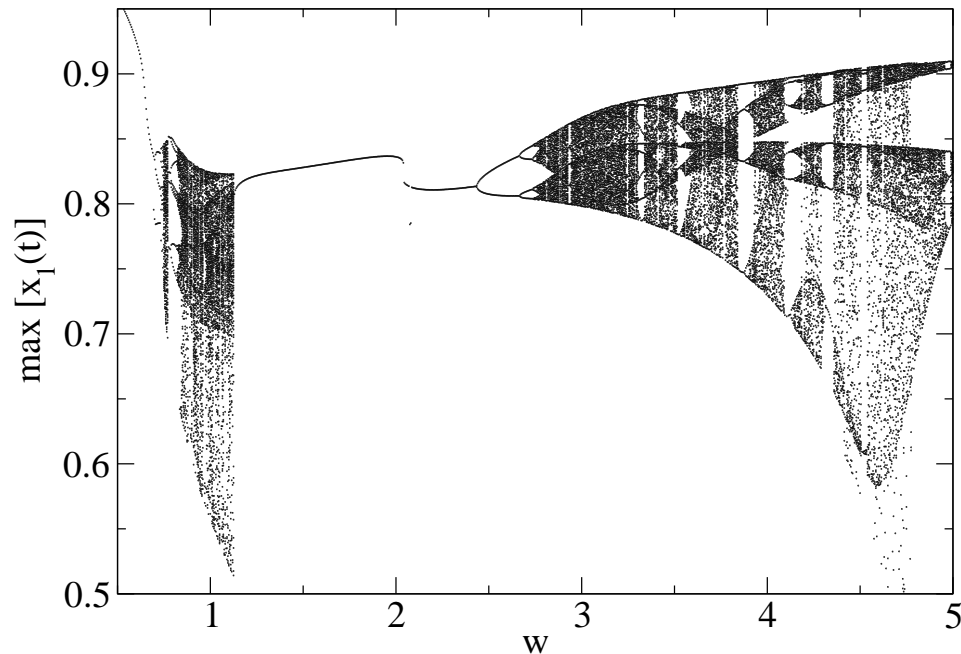


Figure 6.11: Bifurcation diagram depicting local maxima of $x_1(t)$ oscillations for a range of strengths w of the inhibitory connections in the first chaotic motif (Fig. 6.10(b)). Period doubling cascades start around $w = 0.7$ and $w = 2.5$.

observed when strength of each of the links was varied separately while the rest were kept fixed.

6.3.3 Dynamics in spatial networks

However, there are no conclusive experimental observations of chaotic dynamics in either genetic or neuronal networks. Recently performed careful analyzes of the methods used in works that have claimed to observe chaos in EEG data concluded that these methods are not reliable enough to support such claims [14, 51]. Also, presence of chaotic dynamics would be inconsistent with the requirements of robustness and reproducibility of the response imposed on the living organisms by the environment. On the other hand, periodic dynamics in these networks are very common. Hence, some of the assumptions that were used in these simplified models must be wrong. As we show below, one of them is the assumption of ER connectivity. Recent experimental data suggest that metabolic networks possess scale-free structure [43] while neuronal

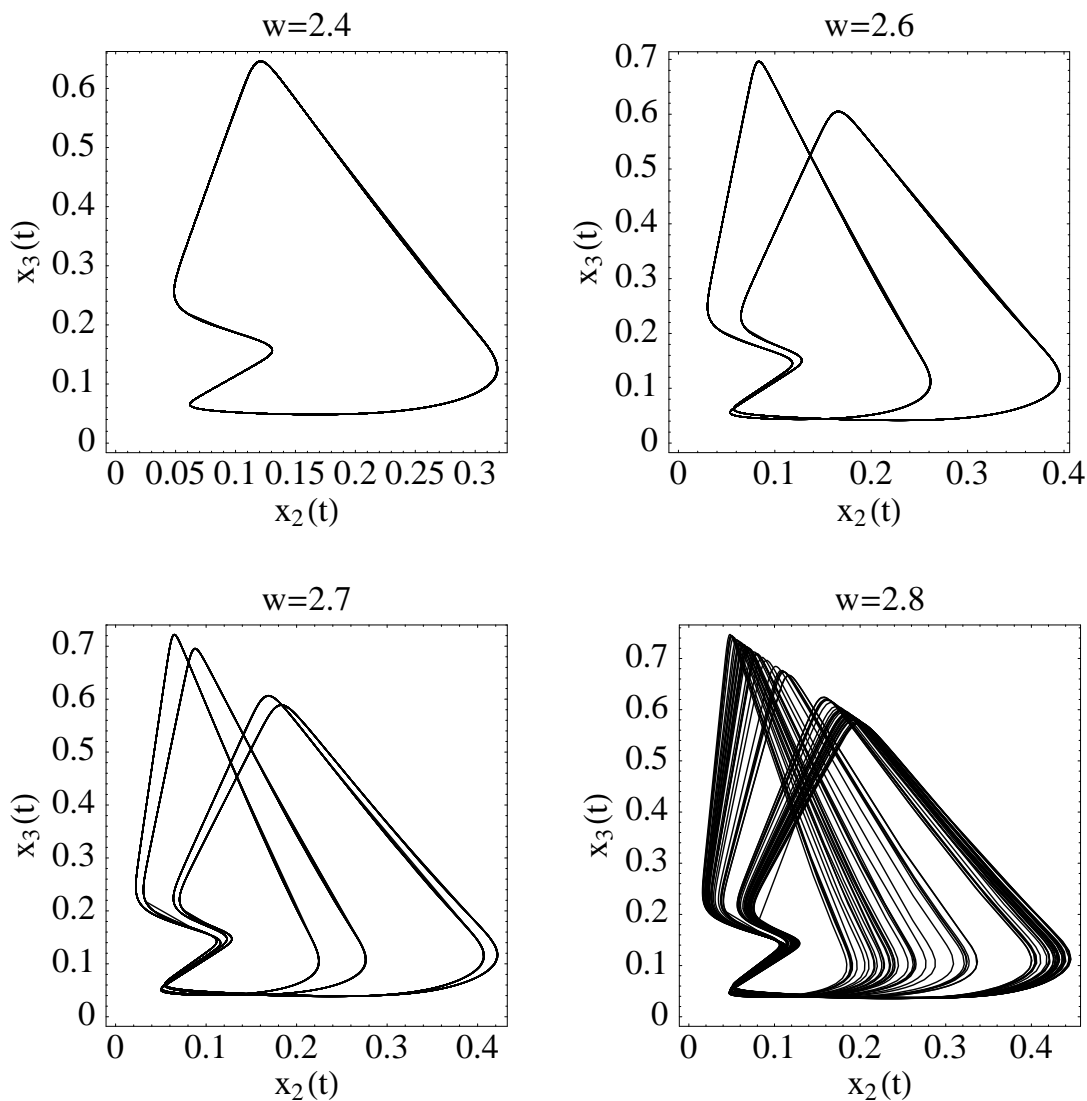


Figure 6.12: Projections of the five-dimensional phase space onto two-dimensional plane calculated for different strengths w of the inhibitory connections in the first chaotic motif (Fig. 6.10(b)). Period doubling bifurcations of the limit cycle are clearly seen.

networks are highly clustered on both small [85] and large [38] spatial scales. Moreover, neurons in the brain frequently form ordered spatial structures with distance-dependent probabilities of connections, so-called cortical microcircuits [86, 56].

To illustrate the influence of spatial structure on the dynamical properties of networks we simulated the cANN model on the 12-by-12 two-dimensional square

lattice with neuron-to-neuron connection probabilities obeying Gaussian distribution and forbidden self-connections:

$$p(d_{ij}) = KN(1 - \delta_{ij})e^{-\left(\frac{d_{ij}}{\gamma}\right)^2} / \sum_{m,n=1}^N (1 - \delta_{mn})e^{-\left(\frac{d_{mn}}{\gamma}\right)^2}, \quad (6.19)$$

where d_{ij} is a metric distance between neurons i and j , γ is the length scale of the distribution, K is the average number of connections per neuron and δ_{ij} is the Kronecker delta. In effect, γ controls clustering of the connectivity, with values close to 1 corresponding to networks with mostly local connectivity and large values effectively diminishing the role of spatial structure and corresponding to ER-like connectivity.

We generated a random sample of 1000 such networks with $\gamma = 2$ and $K = 14$. As in the case of an ER sample, cANN dynamics was simulated in each of the networks for 100 different random initial conditions and the largest Lyapunov exponent was calculated in each simulation. An average connectivity $K = 14$ corresponds to $p \approx 0.1$ which has led to approximately 99% of chaotic networks in a sample of ER ensemble (Fig. 6.10). On the contrary, around 99% of the networks with $\gamma = 2$ exhibited periodic dynamics and only about 1% were chaotic. This result indicates that clustering plays an important role in defining dynamical properties of neural networks and supports an observation that many real neuronal networks are locally clustered.

We now show how the idea of dynamical motifs may be used to understand these observations. Let us enumerate grid nodes by $1, \dots, N$ and consider a motif with n nodes and l links placed on the grid. We label its nodes by i_1, i_2, \dots, i_n and its links by $i_{a_1}i_{b_1}, i_{a_2}i_{b_2}, \dots, i_{a_l}i_{b_l}$ with $a_j b_j, j = 1 \dots l$ denoting ordered pairs of nodes that are connected. Probability $P_{i_a i_b}$ for the grid nodes i_a and i_b to be connected is distance-dependent and is given by (6.19). Then the average probability that n nodes of a network form this motif is obtained by averaging over all possible placements of its nodes on a grid:

$$p_n \approx \frac{1}{N^n} \sum_{i_1, \dots, i_n=1}^N \left(\prod_{j=1}^l P_{i_{a_j} i_{b_j}} \prod_{k=1}^s (1 - P_{i_{u_k} i_{v_k}}) \right), \quad (6.20)$$

where $s = n(n-1) - l$ and $u_k v_k$ are all the pairs of unconnected nodes. For example, an average probability for a 3-loop (Fig. 6.8(a)) is $p_3 = \frac{1}{N^3} \sum_{i_1, i_2, i_3=1}^N P_{i_1 i_2} P_{i_2 i_3} P_{i_3 i_1} (1 - P_{i_2 i_1})(1 - P_{i_3 i_2})(1 - P_{i_1 i_3})$. As expected, in the limit of distance-independent probabilities expression (6.20) becomes equivalent to the ER case. Probability of occurrence of one or more motifs in a network can again be approximated by (6.13). It is approximately 1 for 3- and 4-loops and $P_m \approx 0$ for the (5; 9) motif in networks with $\gamma = 2$. Other chaotic motifs would be even less probable because connection probability falls off quickly with distance in these networks. Also, $P_m \approx 1$ for the (5; 9) motif in networks with $\gamma = 12$. Hence, periodic motifs are present and chaotic motifs are absent in spatial networks with local connectivity ($\gamma = 2$), but chaotic motifs are present in non-local networks with $\gamma = 12$. These calculations may also explain recent observations of periodic and chaotic dynamics in models of cortical neural microcircuits with local and non-local spatial organization of connectivity [56]. Eq. (6.20) may also be applied in the study of networks with other distributions of connectivity, such as, e.g., networks with scale-free degree distributions. Our analysis of oscillatory dynamics on such networks will be presented elsewhere.

6.4 Discussion

In conclusion, a method to study dynamical behavior of networks by examining minimal building blocks of the dynamics was suggested. Calculations of abundance of dynamical motifs in networks with different structure allow to study and control dynamics in these networks by choosing connectivity that maximizes the probability of motifs with desirable dynamics and minimizes probability of motifs with unacceptable dynamics. Using this method we predict that connectivity of cortical networks might be such that it minimizes the occurrence of chaotic motifs in their structure.

In some real networks average node degree is high compared to $K \sim 10$ considered here. However, many of the connections are weak and were excluded from the model as they play minor role in the dynamics. Hence, only the number of strong connections should be compared. In the brain, for example, although a given neuron may be

receiving on the order of 10^3 inputs, typically only about 10 of them are strong.

It was shown in [66] that many real networks have 3-loops in their structure. In most cases there are very few of such loops and it was argued that their presence is not statistically significant. However, we suggest that such dynamical motifs are important because presence of even one or two of them may profoundly influence dynamical behavior of the whole network by slaving dynamics of many adjacent nodes.

Bibliography

- [1] H. D. I. Abarbanel, R. Huerta, and M. I. Rabinovich. Dynamical model of long-term synaptic plasticity. *Proc. Natl. Acad. Sci. USA*, 99(15):10132–10137, 2002.
- [2] H. D. I. Abarbanel, R. Huerta, M. I. Rabinovich, N. F. Rulkov, P. F. Rowat, and A. I. Selverston. Synchronized action of synaptically coupled chaotic model neurons. *Neural Comput.*, 8:1567–1602, 1996.
- [3] M. Abeles. *Corticonics: Neural circuits of the cerebral cortex*. Cambridge University Press, Cambridge, 1991.
- [4] R. Albert and A. L. Barabasi. Statistical mechanics of complex networks. *Rev. Mod. Phys.*, 74:47–97, 2002.
- [5] M. Aldana, S. Coppersmith, and L. P. Kadanoff. Boolean dynamics with random couplings. <http://arxiv.org/nlin.AO/0204062>.
- [6] U. Bastolla and G. Parisi. Relaxation, closing probabilities and transition from oscillatory to chaotic attractors in asymmetric neural networks. *J. Phys. A*, 31:4583–4602, 1998.
- [7] M. F. Bear and D. J. Linden. *Synapses*, page 455. J. Hopkins Univ. Press, 2000.
- [8] C. C. Bell, V. Z. Han, Y. Sugawara, and K. Grant. Synaptic plasticity in a cerebellum-like structure depends on temporal order. *Nature*, 387(6630):278–281, 1997.

- [9] C. C. Bell, V. Z. Han, Y. Sugawara, and K. Grant. Synaptic plasticity in the mormyrid electrosensory lobe. *J. Exp. Biol.*, 202:1339–1347, 1999.
- [10] M. J. Berry, D. K. Warland, and M. Meister. The structure and precision of retinal spike trains. *Proc. Natl. Acad. Sci. USA*, 94(10):5411–5416, 1997.
- [11] G.-Q. Bi and M.-M. Poo. Synaptic modifications in cultured hippocampal neurons: Dependence on spike timing, synaptic strength, and postsynaptic cell type. *J. Neurosci.*, 18(24):10464–10472, 1998.
- [12] G.-Q. Bi and M.-M. Poo. Synaptic modification by correlated activity: Hebb’s postulate revisited. *Annu. Rev. Neurosci.*, 24(1):139–166, 2001.
- [13] G.-Q. Bi and H. X. Wang. Temporal asymmetry in spike timing-dependent synaptic plasticity. *Physiol. Behav.*, 77(4-5):551–555, 2002.
- [14] B. Biswal and C. Dasgupta. Neural network model for apparent deterministic chaos in spontaneously bursting hippocampal slices. *Phys. Rev. Lett.*, 88:088102, 2002.
- [15] A. Borst and F. E. Theunissen. Information theory and neural coding. *Nat. Neurosci.*, 2(11):947–957, 1999.
- [16] A. Bose, Y. Manor, and F. Nadim. Bistable oscillations arising from synaptic depression. *SIAM J. Appl. Math.*, 62(2):706–727, 2001.
- [17] D. L. Buhl, K. D. Harris, S. G. Hormuzdi, H. Monyer, and G. Buzsaki. Selective impairment of hippocampal gamma oscillations in connexin-36 knock-out mouse in vivo. *J. Neurosci.*, 23(3):1013–1018, 2003.
- [18] B. Cazelles, M. Courbage, and M. Rabinovich. Anti-phase regularization of coupled chaotic maps modelling bursting neurons. *Europhys. Lett.*, 56:504–509, 2001.
- [19] S. Coombes and P. C. Bressloff. Mode-locking and Arnold tongues in integrate-and-fire neural oscillators. *Phys. Rev. E*, 60:2086–2096, 1999.

- [20] J. P. Crutchfield and K. Young. Inferring statistical complexity. *Phys. Rev. Lett.*, 63:105–108, 1989.
- [21] S. N. Dorogovtsev and J. F. F. Mendes. Evolution of networks. *Adv. Phys.*, 51:1079–1187, 2002.
- [22] K. Doya and S. Yoshizawa. Adaptive neural oscillator using continuous-time back-propagation learning. *Neural Networks*, 2:375–385, 2001.
- [23] M. Elhilali, J. B. Fritz, D. J. Klein, J. Z. Simon, and S. A. Shamma. Dynamics of precise spike timing in primary auditory cortex. *J. Neurosci.*, 24(5):1159–1172, 2004.
- [24] R. C. Elson, A. I. Selverston, R. Huerta, N. F. Rulkov, M. I. Rabinovich, and H. D. I. Abarbanel. Synchronous behavior of two coupled biological neurons. *Phys. Rev. Lett.*, 81:5692–5695, 1998.
- [25] A. K. Engel, P. Fries, and W. Singer. Dynamic predictions: Oscillations and synchrony in top-down processing. *Nature Rev. Neurosci.*, 2(10):704–716, 2001.
- [26] G. B. Ermentrout and N. Kopell. Learning of phase lags in coupled neural oscillators. *Neural Comput.*, 6:225–241, 1994.
- [27] D. E. Feldman. Timing-based LTP and LTD at vertical inputs to layer II/III pyramidal cells in rat barrel cortex. *Neuron*, 27(1):45–56, 2000.
- [28] J. Fell, P. Klaver, K. Lehnertz, T. Grunwald, C. Schaller, C. E. Elger, and G. Fernandez. Human memory formation is accompanied by rhinal-hippocampal coupling and decoupling. *Nature Neurosci.*, 4(12):1259–1264, 2001.
- [29] R. C. Froemke and Y. Dan. Spike-timing-dependent synaptic modification induced by natural spike trains. *Nature*, 416(6879):433–438, 2002.
- [30] L. Glass. Synchronization and rhythmic processes in physiology. *Nature*, 410(6825):277–284, 2001.

- [31] L. Glass and C. Hill. Ordered and disordered dynamics in random networks. *Europhys. Lett.*, 41:599–604, 1998.
- [32] A. Goldbeter. Computational approaches to cellular rhythms. *Nature*, 420(6912):238–245, 2002.
- [33] E. Greenfeld and H. Lécarr. Mutual information in a dilute, asymmetric neural network model. *Phys. Rev. E*, 63:041905, 2001.
- [34] H. Hayashi and S. Ishizuka. Chaotic nature of bursting discharges in the onchidium pacemaker neuron. *J. Theor. Biol.*, 156:269–291, 1992.
- [35] D. H. He, G. Hu, M. Zhan, and H. P. Lu. Periodic states with functional phase relation in weakly coupled chaotic Hindmarsh-Rose neurons. *Physica D*, 156:314–324, 2001.
- [36] D. O. Hebb. *The Organization of Behavior*. Wiley, New York, 1949.
- [37] J. Heller, J. A. Hertz, T. W. Kjaer, and B. J. Richmond. Information flow and temporal coding in primate pattern vision. *J. Comput. Neurosci.*, 2(3):175–193, 1995.
- [38] C. C. Hilgetag, G. A. Burns, M. A. O’Neill, J. W. Scannell, and M. P. Young. Anatomical connectivity defines the organization of clusters of cortical areas in the macaque monkey and the cat. *Philos. Trans. R. Soc. London, Ser. B*, 355(1393):91–110, 2000.
- [39] J. L. Hindmarsh and R. M. Rose. A model of neuronal bursting using 3 coupled first-order differential equations. *Proc. R. Soc. Lond. Ser. B*, 221:87–102, 1984.
- [40] A. L. Hodgkin and A. F. Huxley. A quantitative description of membrane current and its application to conduction and excitation in nerve. *J. Physiol. (London)*, 117(4):500–544, 1952.

- [41] J. J. Hopfield. Neurons with graded response have collective computational properties like those of 2-state neurons. *Proc. Natl. Acad. Sci. USA*, 81:3088–3092, 1984.
- [42] S. G. Hormuzdi, I. Pais, F. E. LeBeau, S. K. Towers, A. Rozov, E. H. Buhl, M. A. Whittington, and H. Monyer. Impaired electrical signaling disrupts gamma frequency oscillations in connexin 36-deficient mice. *Neuron*, 31(3):487–495, 2001.
- [43] H. Jeong, B. Tombor, R. Albert, Z. N. Oltval, and A. L. Barabasi. The large-scale organization of metabolic networks. *Nature*, 407(6804):651–654, 2000.
- [44] E. R. Kandel. *Cellular Basis of Behavior*. Freeman, San Francisco, 1976.
- [45] J. Karbowski and G. B. Ermentrout. Synchrony arising from a balanced synaptic plasticity in a network of heterogeneous neural oscillators. *Phys. Rev. E*, 65:031902, 2002.
- [46] U. R. Karmarkar and D. V. Buonomano. A model of spike-timing dependent plasticity: One or two coincidence detectors? *J. Neurophysiol.*, 88(1):507–513, 2002.
- [47] R. Kempter, W. Gerstner, and J. L. van Hemmen. Intrinsic stabilization of output rates by spike-based Hebbian learning. *Neural Comput.*, 13(12):2709–2741, 2001.
- [48] C. Koch and G. Laurent. Complexity and the nervous system. *Science*, 284(5411):96–98, 1999.
- [49] M. Kondoh. Foraging adaptation and the relationship between food-web complexity and stability. *Science*, 299(5611):1388–1391, 2003.
- [50] M. La Rosa, M. I. Rabinovich, R. Huerta, H. D. I. Abarbanel, and L. Fortuna. Slow regularization through chaotic oscillation transfer in an unidirectional chain of Hindmarsh-Rose models. *Phys. Lett. A*, 266:88–93, 2000.

- [51] Y. C. Lai, M. A. F. Harrison, M. G. Frei, and I. Osorio. Inability of Lyapunov exponents to predict epileptic seizures. *Phys. Rev. Lett.*, 91:068102, 2003.
- [52] G. Laurent. A systems perspective on early olfactory coding. *Science*, 286(5440):723–728, 1999.
- [53] G. Laurent and H. Davidowitz. Encoding of olfactory information with oscillating neural assemblies. *Science*, 265:1872–1875, 1994.
- [54] A. Loebel and M. Tsodyks. Computation by ensemble synchronization in recurrent networks with synaptic depression. *J. Comput. Neurosci.*, 13(2):111–124, 2002.
- [55] T. Lu and X. Wang. Information content of auditory cortical responses to time-varying acoustic stimuli. *J. Neurophysiol.*, 91(1):301–313, 2004.
- [56] W. Maass, T. Natschlager, and H. Markram. Real-time computing without stable states: A new framework for neural computation based on perturbations. *Neural Comp.*, 14(11):2531–2560, 2002.
- [57] Z. F. Mainen and T. J. Sejnowski. Reliability of spike timing in neocortical neurons. *Science*, 268(5216):1503–1506, 1995.
- [58] G. Major, R. Baker, E. Aksay, B. Mensh, H. S. Seung, and D. W. Tank. Plasticity and tuning by visual feedback of the stability of a neural integrator. *Proc. Natl. Acad. Sci. USA*, 101(20):7739–7744, 2004.
- [59] V. Makarenko and R. Llinas. Experimentally determined chaotic phase synchronization in a neuronal system. *Proc. Natl. Acad. Sci. USA*, 95(26):15747–15752, 1998.
- [60] Y. Manor and F. Nadim. Synaptic depression mediates bistability in neural networks with recurrent inhibitory connectivity. *J. Neurosci.*, 21(23):9460–9470, 2001.

- [61] H. Markram, J. Lubke, M. Frotscher, and B. Sakmann. Regulation of synaptic efficacy by coincidence of postsynaptic APs and EPSPs. *Science*, 275(5297):213–215, 1997.
- [62] B. D. McKay. Isomorph-free exhaustive generation. *J. Algorithms*, 26:306–324, 1998.
- [63] M. R. Mehta, A. K. Lee, and M. A. Wilson. Role of experience and oscillations in transforming a rate code into a temporal code. *Nature*, 417(6890):741–746, 2002.
- [64] P. Melby, J. Kaidel, N. Weber, and A. Hübner. Adaptation to the edge of chaos in the self-adjusting logistic map. *Phys. Rev. Lett.*, 84:5991–5993, 2000.
- [65] T. Mestl, R. J. Bagley, and L. Glass. Common chaos in arbitrarily complex feedback networks. *Phys. Rev. Lett.*, 79:653–656, 1997.
- [66] R. Milo, S. Shen-Orr, S. Itzkovitz, N. Kashtan, D. Chklovskii, and U. Alon. Network motifs: Simple building blocks of complex networks. *Science*, 298:824–827, 2002.
- [67] W. H. R. Miltner, C. Braun, M. Arnold, H. Witte, and E. Traub. Coherence of gamma-band EEG activity as a basis for associative learning. *Nature*, 397(6718):434–436, 1999.
- [68] M. E. J. Newman. The structure and function of complex networks. *SIAM Rev.*, 45:167–256, 2003.
- [69] T. Nowotny, V. P. Zhigulin, A. I. Selverston, H. D. I. Abarbanel, and M. I. Rabinovich. Enhancement of synchronization in a hybrid neural circuit by spike timing dependent plasticity. *J. Neurosci.*, 23(30):9776–9785, 2003.
- [70] E. Ott, C. Grebogi, and J. A. Yorke. Controlling chaos. *Phys. Rev. Lett.*, 64:1196–1199, 1990.

- [71] Y. Perez, F. Morin, and J.-C. Lacaille. A Hebbian form of long-term potentiation dependent on mGluR1a in hippocampal inhibitory interneurons. *Proc. Natl. Acad. Sci. USA*, 98(16):9401–9406, 2001.
- [72] R. D. Pinto, R. C. Elson, A. Szücs, M. I. Rabinovich, A. I. Selverston, and H. D. I. Abarbanel. Extended dynamic clamp: Controlling up to four neurons using a single desktop computer and interface. *J. Neurosci. Methods*, 108:39–48, 2001.
- [73] K. Pyragas. Continuous control of chaos by self-controlling feedback. *Phys. Lett. A*, 170:421–428, 1992.
- [74] M. I. Rabinovich and H. D. I. Abarbanel. The role of chaos in neural systems. *Neuroscience*, 87:5–14, 1998.
- [75] M. I. Rabinovich, H. D. I. Abarbanel, R. Huerta, R. Elson, and A. I. Selverston. Self-regularization of chaos in neural systems: Experimental and theoretical results. *IEEE Trans. Circuits Syst. I*, 44:997–1005, 1997.
- [76] M. I. Rabinovich, P. Varona, J. J. Torres, R. Huerta, and H. D. I. Abarbanel. Slow dynamics and regularization phenomena in ensembles of chaotic neurons. *Physica A*, 263:405–414, 1999.
- [77] M. I. Rabinovich, A. Volkovskii, P. Lecanda, R. Huerta, H. D. I. Abarbanel, and G. Laurent. Dynamical encoding by networks of competing neuron groups: Winnerless competition. *Phys. Rev. Lett.*, 87:068102, 2001.
- [78] R. P. Rao and T. J. Sejnowski. Spike-timing-dependent Hebbian plasticity as temporal difference learning. *Neural Comput.*, 13(10):2221–2237, 2001.
- [79] A. Riehle, S. Grun, M. Diesmann, and A. Aertsen. Spike synchronization and rate modulation differentially involved in motor cortical function. *Science*, 278(5345):1950–1953, 1997.

- [80] J. Rubin, D. D. Lee, and H. Sompolinsky. Equilibrium properties of temporally asymmetric Hebbian plasticity. *Phys. Rev. Lett.*, 86:364–367, 2001.
- [81] J. E. Rubin. Steady states in an iterative model for multiplicative spike-timing-dependent plasticity. *Network*, 12(2):131–140, 2001.
- [82] N. F. Rulkov. Regularization of synchronized chaotic bursts. *Phys. Rev. Lett.*, 86:183–186, 2001.
- [83] A. A. Sharp, M. B. O’Neil, L. F. Abbott, and E. Marder. The dynamic clamp: artificial conductances in biological neurons. *Trends Neurosci.*, 16:389–94, 1993.
- [84] A. A. Sharp, M. B. O’Neil, L. F. Abbott, and E. Marder. Dynamic clamp: computer-generated conductances in real neurons. *J. Neurophysiol.*, 69(3):992–995, 1993.
- [85] O. Shefi, I. Golding, R. Segev, E. Ben-Jacob, and A. Ayali. Morphological characterization of in vitro neuronal networks. *Phys. Rev. E*, 66:021905, 2002.
- [86] G. Silberberg, A. Gupta, and H. Markram. Stereotypy in neocortical microcircuits. *Trends Neurosci.*, 25(5):227–230, 2002.
- [87] I. Simonsen, K. A. Eriksen, S. Maslov, and K. Sneppen. Diffusion on complex networks : A way to probe their large-scale topological structures. <http://arxiv.org/cond-mat/0312476>.
- [88] H. Sompolinsky, A. Crisanti, and H. J. Sommers. Chaos in random neural networks. *Phys. Rev. Lett.*, 61:259–262, 1988.
- [89] S. Song and L. F. Abbott. Cortical development and remapping through spike timing-dependent plasticity. *Neuron*, 32(2):339–350, 2001.
- [90] S. Song, K. D. Miller, and L. F. Abbott. Competitive Hebbian learning through spike-timing-dependent synaptic plasticity. *Nature Neurosci.*, 3(9):919–926, 2000.

- [91] R. E. Suri and T. J. Sejnowski. Spike propagation synchronized by temporally asymmetric Hebbian learning. *Biol. Cybern.*, 87(5-6):440–445, 2002.
- [92] B. Tadic and S. Thurner. Information super-diffusion on structured networks. *Physica A*, 332:566–584, 2004.
- [93] B. Tadic, S. Thurner, and G. J. Rodgers. Traffic on complex networks: Towards understanding global statistical properties from microscopic density fluctuations. <http://arxiv.org/cond-mat/0401094>.
- [94] R. D. Traub and R. Miles. *Neuronal Networks of the Hippocampus*, chapter 4. Cambridge Univ. Press, 1991.
- [95] R. D. Traub, I. Pais, A. Bibbig, F. E. LeBeau, E. H. Buhl, S. G. Hormuzdi, H. Monyer, and M. A. Whittington. Contrasting roles of axonal (pyramidal cell) and dendritic (interneuron) electrical coupling in the generation of neuronal network oscillations. *Proc. Natl. Acad. Sci. USA*, 100(3):1370–1374, 2003.
- [96] M. Tsodyks, A. Uziel, and H. Markram. Synchrony generation in recurrent networks with frequency-dependent synapses. *J. Neurosci.*, 20(1):RC50, 2000.
- [97] M. C. van Rossum, G.-Q. Bi, and G. G. Turrigiano. Stable Hebbian learning from spike timing-dependent plasticity. *J. Neurosci.*, 20(23):8812–8821, 2000.
- [98] C. vanVreeswijk and H. Sompolinsky. Chaos in neuronal networks with balanced excitatory and inhibitory activity. *Science*, 274:1724–1726, 1996.
- [99] F. Varela, J.-P. Lachaux, E. Rodriguez, and J. Martinerie. The brainweb: Phase synchronization and large-scale integration. *Nature Rev. Neurosci.*, 2(4):229–239, 2001.
- [100] J. D. Victor. How the brain uses time to represent and process visual information. *Brain Res.*, 886(1-2):33–46, 2000.
- [101] A. D. Wagner. Synchronicity: when you’re gone I’m lost without a trace? *Nature Neurosci.*, 4(12):1159–1160, 2001.

- [102] M. Wehr and G. Laurent. Odour encoding by temporal sequences of firing in oscillating neural assemblies. *Nature*, 384(6605):162–166, 1996.
- [103] A. Whitehead, M. I. Rabinovich, R. Huerta, V. P. Zhigulin, and H. D. I. Abarbanel. Dynamical synaptic plasticity: A model and connection to some experiments. *Biol. Cybern.*, 88:229–235, 2003.
- [104] A. T. Winfree. *The Geometry of Biological Time*. Springer-Verlag, New York, 1980.
- [105] M. Zhan, G. Hu, Y. Zhang, and D. H. He. Generalized splay state in coupled chaotic oscillators induced by weak mutual resonant interactions. *Phys. Rev. Lett.*, 86:1510–1513, 2001.
- [106] L. I. Zhang, H. W. Tao, C. E. Holt, W. A. Harris, and M.-M. Poo. A critical window for cooperation and competition among developing retinotectal synapses. *Nature*, 395(6697):37–44, 1998.
- [107] V. P. Zhigulin. Dynamical motifs: Building blocks of complex dynamics in sparsely connected random networks. *Phys. Rev. Lett.*, in press.
- [108] V. P. Zhigulin and M. I. Rabinovich. An important role of spike timing dependent synaptic plasticity in the formation of synchronized neural ensembles. *Neurocomputing*, 58-60:373–378, 2004.
- [109] V. P. Zhigulin and M. I. Rabinovich. Self-control of chaos in neural circuits with plastic electrical synapses. *Radiofizika (Russia)*, in press.
- [110] V. P. Zhigulin, M. I. Rabinovich, R. Huerta, and H. D. I. Abarbanel. Robustness and enhancement of neural synchronization by activity-dependent coupling. *Phys. Rev. E*, 67:021901, 2003.